Design of an RF Ion Thruster

by

Johannes Rudolf Botha

Thesis presented in fulfilment of the requirements for the degree of Master of Engineering (Research) in the Faculty of Electrical and Electronic Engineering at Stellenbosch University

Supervisor: Prof. Thomas Jones
Co-supervisor: Prof. Johann de Swardt

April 2014

Declaration

By submitting this thesis electronically, I declare that the entirety of the work contained therein is my own, original work, that I am the sole author thereof (save to the extent explicitly otherwise stated), that reproduction and publication thereof by Stellenbosch University will not infringe any third party rights and that I have not previously in its entirety or in part submitted it for obtaining any qualification.

April 2014

Abstract

Recent years have seen a decline in the rate of space exploration due to the inefficiency of chemical rockets. Therefore alternative fuel efficient propulsion methods are being sought to enable cost effective deep space exploration. The high fuel efficiency of electric thrusters enable a spacecraft to travel further, faster and cheaper than any other propulsion technology available. Thus electric propulsion has become the propulsion of choice for scientists and engineers. A typically electric thruster contains some sort of electrode to ionise the propellant. Although this is feasible for short space missions, it becomes impractical for more ambitious space missions as electrodes erode over time. The alternative is to ionise the propellant using electromagnetic fields, which eliminates lifespan issues associated with electrode based thrusters.

In order to examine methods of improving the lifespan and performance of electric thrusters, this thesis aimed to study the method of microwave discharge ionisation for an electric thruster. This includes the design of an RF Ion Thruster with extraction and acceleration grids to generate thrust. A 600 W 2.45 GHz magnetron (obtained from a conventional microwave oven), coupled to circular TM_{010} resonant cavity, was used to ionise neutral argon gas. The process of electron cyclotron resonance (ECR) was used to ensure the efficient ionisation of a high density plasma. The thrust was achieved with a three-grid system biased at high voltages to accelerate positively charged argon ions to high exhaust velocities.

Results yielded the success of the designed electromagnetic based thruster, measuring approximatively 1.78 mN of thrust with a specific impulse of $I_{sp} = 3786$ $seconds$. The ECR process produced a high plasma density with a plasma absorption rate of approximately 77% of the total input microwave power. The final results obtained were found to match the predicted results extremely well and resembled results found in literature. This demonstrates the efficiency of the RF ion thruster that was designed in this project and the future use in space exploration activities. However, future research needs to be undertaken on a controlled feedback system that will ensure optimal operating conditions for maximum performance. In addition, the method of grid-less acceleration needs to be studied to achieve maximum thrust and specific impulse.

Uitreksel

In onlangse jare het 'n afname in die tempo van die verkenning van die ruimte dit te danke aan die ondoeltreffendheid van chemiese vuurpyle. Derhalwe moet alternatiewe brandstof aandrywing metodes ondersoek word, om koste-effektiewe diep ruimte-eksplorasie moontlik te maak. Die hoë brandstof-doeltreffendheid van elektriese ontbranders stel 'n ruimtetuig in staat om verder, vinniger en goedkoper te reis as enige ander aandrywing tegnologie wat tans beskikbaar is. Dus het elektriese aandrywing metodes die aandrywings keuse vir wetenskaplikes en ingenieurs geword. 'n Tipies elektriese vuurpyl/aandrywer bevat 'n vorm van elektrode om die brandstof (argon gas) te ioniseer. Alhoewel hierdie elektrode proses van ionisasie effektief is vir kort ruimte missies, word dit onprakties vir meer ambisieuse ruimte missies as gevolg van verweering van elektrodes met verloop van tyd. 'n Alternatief is om die dryfmiddel/brandstof te ioniseer deur gebruik te maak van elektromagnetiese velde. Die elekromagnetiese velde sal die lewensduur van die vuurpyl vermeerder deur die verweering van elektrodes, wat geassosieer word met tipiese elektrieses vuurpyle, te elimineer.

Hierdie tesis se doelwit is om die metode van mikrogolf ontslag ionisasie vir 'n elektriese vuurpyl/aandrywer te bestudeer om ten einde die lewensduur en doeltreffendheid van elektriese vuurpyl/aandrywer te ondersoek. Dit sluit in die ontwerp van 'n radio frekewensie ioon vuurpyl/aandrywer met 'n ontginning en versnelling matriks/rooster om stukrag te genereer. 'n 2,45 GHz magnetron (verkry vanaf 'n konvensionele mikrogolfoond), gekoppel aan 'n TM_{010} resonante holte, was gebruik om neutrale argon gas te ioniseer. Die proses van elektron siklotron resonansie (ESR) was gebruik om die doeltreffende ionisasie van 'n hoë digtheid plasma te verseker. Die aandrywing/stukrag was behaal met 'n drie-matriks-stelsel, bevoordeel deur hoë spannings om die positief-gelaaide argon ione te versnel.

Resultate opgelewer, het die sukses van die ontwerp van 'n elektromagnetiese gebaseerde vuurpyl/aandrywer met 'n benaderde meting van ongeveer 1.78 mN van stukrag/aandrywing met 'n spesifieke impuls van $I_{sp} = 3786$ *sekondes* bewys. Die ECR proses het 'n hoë plasma digtheid geproduseer met 'n plasma opname persentasie van ongeveer 77% van die totale inset mikrogolf energie. Die finale uitslae wat verkry was, het bevind dat die voorspelde resultate baie goed inpas met resultate in beskikbare literatuur. Dit dui op die

doeltreffendheid van die RF ioon vuurpyl/aandrywer wat ontwerp is in hierdie projek vir die toekomstige gebruik in ruimte eksplorasie-aktiwiteite. Toekomstige navorsing moet op 'n beheerde terugvoer sisteem onderneem word, wat optimale werktoestande verseker vir maksimum prestasie. Daarbenewens moet die metode van matriks-lose versnelling bestudeer word, om maksimum versnelling/stukrag en spesifieke impuls te verseker.

Acknowledgements

It would have been impossible to complete this project without the support and assistance of a number of people who deserve my humblest thanks:

- To my supervisors, Prof. Thomas Jones and Prof. Johann de Swardt, for their support, advice and guidance.
- To the Electrical Engineering staff, Mr. WJ Croukamp, Mr. Lincoln Saunders, Mr. Niklaas van Graan and Mr. Petrus Pieterse for their practical advice and willingness to lend their energy and time.
- To my ESL colleagues for their company. A special thanks to my office colleagues, Paul Moller and Shaun Irwin for the many laughs we shared during this project.
- To Dr. Rainer W. Thomae from iThemba LABS, for his advice on the thruster design and experimental work.
- To my friends and family, for their support, prayers and love.
- To Helouise van Rooyen, you kept me going.
- To my Lord God, your mercy knows no bounds.

Contents

List of Figures

List of Tables

Nomenclature

Constants

AMU	Atomic Mass Unit	$[1.6602176487 \times 10^{-27}\ kg]$
c	Velocity of Light	$[2.9979 \times 10^{8}\ m/s^2]$
η	Impedance of Free Space	$[377\ \Omega]$
ϵ_0	Permittivity of Free Space	$[8.8542 \times 10^{-12}\ F/m]$
eV	Energy Associated with 1 Electron Volt	$[1.602176487 \times 10^{-19}\ J]$
g_0	Gravitational Acceleration	$[9.80665\ m/s^2]$
μ_0	Permeability of Free Space	$[4\pi \times 10^{-7}\ H/m]$
m_e	Electron Mass	$[9.1093822 \times 10^{-31}\ kg]$
M	Ion Mass	$[6.68993 \times 10^{-26}\ kg]$
q	Electron Or Ion Charge	$[1.6020176487 \times 10^{-19}\ C]$

Acronyms and Abbreviations

accel grid	Acceleration Grid
AMU	Atomic Mass Unit
AWG	American Wire Gauge
CST	Computer Simulation Software
DC	Direct Current
decel grid	Deceleration Grid
ECR	Electron Cyclotron Resonance
eV	Electron Volt

FDA	Food and Drug Administration
MET	Microwave Electrothermal Thruster
MPD	Magnetoplasmadynamic Thruster
NASA	National Aeronautics and Space Administration
NEXT	NASA'S Evolutionary Xenon Thruster
RF	Radio Frequency
sccm	Standard cubic centimetres per minute
SMART	Small Mission for Advanced Research in Technology
SmCo	Samarium Cobalt
TE	Transelectric
TM	Transmagnetic
VASMIR	Variable Specific Impulse Magnetoplasma Rocket
VNA	Vector Network Analyser
XIPS	Xenon Ion Propulsion System

Defined Terms

F_t	Thrust Correction Due To Beam Divergence
I_{sp}	Specific Impulse
M_{fuel}	Fuel mass
M_{total}	Spacecraft mass
Q-value	Quality Factor
T_e	Electron Temperature

Variables

a	Internal Radius of cavity, Waveguide Width
A_g	Total Area of Grid

A_{open}	Grid Area Containing Apertures
b	Waveguide Height
B	Magnetic Field
d	Gap Distance
d_a	Acceleration Grid Aperture Diameter
d_s	Screen Grid Aperture Diameter
d_d	Deceleration Grid Aperture Diameter
E	Electric field
$E_{k,ion}$	Ion Kinetic Energy
F	Force
h	Cavity Height
I	Current
I_b	Beam Current
I^+	Singly Charged Ion Current
I^{++}	Doubly Charged Ion Current
J	Current Density
J_i	Ion Current Density
J_{max}	Maximum Child-Langmuir Current Density
k	Wave Number $= 2\pi/\lambda$
K	Proportional Constant
l	Length
l_e	Sheath Thickness Length
l_g	Grid Gap Length (sreen and accel grid)
l_d	Grid Gap Length (accel and decel grid)
m	Mass, Electron Mass
m_i	Propellant Mass Due to Ions

m_p	Propellant Mass
$\dot{m}_i$	Ion Mass Flow Rate
$\dot{m}_p$	Total Propellant Mass Flow Rate
M	Ion Mass, Total Spacecraft mass
N	Number of Turns
n	Particle Density
n_e	Electron Density
n_i	Ion Density
p	Value of Integer Half Wavelengths
P_{in}	Power Into The Plasma Discharge
P_{jet}	Jet Power (Kinetic Power)
P_{max}	Maximum Perveance
P_T	Total Electric Power Into Thruster
q	Charge
Q	Propellant Flow Rate
R	Resistance
R_s	Surface Resistance
S_{11}	Return loss
S_{21}	Insertion Loss
t_a	Acceleration grid thickness
t_s	Screen grid thickness
t_d	Deceleration grid thickness
T	Thrust, Temperature
T_e	Electron Temperature
T_m	Sum of Thrust for Multiple Species
v	Velocity

v_B	Bohm Velocity
v_{ex}	Exhaust Velocity
v_i	Ion Velocity
v_e	Electron Velocity
v_{col}	Collision Frequency
V_a	Acceleration Grid Voltage
V_s	Screen Grid Voltage
V_d	Deceleration Grid Voltage
V_b	Net Beam Voltage
X_{mn}	Bessel Function Values for Mode of Operation

Symbols

α	Thrust Correction Factor for Double Charged Ions
γ	Total Thrust correction Factor = αF_t
Δv	Change In Velocity
η_e	Electrical Efficiency
η_m	Mass Utilisation Efficiency
η_T	Total Thruster Efficiency
λ	Wavelength
ω	Cyclic Frequency ($2\pi f$)
ω_p	Electron Plasma Frequency
ω_c	Electron Cyclotron Frequency
σ	Conductivity
ϵ	Permittivity
ϵ_r'	Dielectic Constant
ϵ_r''	Dielectic Loss

Chapter 1

Introduction

1.1 Background and Motivation

Space exploration was shown to be possible when Tsiolkovsky published a paper in 1903 that derived the rocket equation and explained the idea of rocket propulsion for space travel in detail [1]. The contribution of Tsiolkovksy, Goddard, Oberth and many others, led to the invention of the chemical rocket. Space exploration accelerated after the chemical rocket was invented, with moon walks occurring within ten years of the first man orbiting the earth. Since then the rate of progress has decreased. This decrease is due to the fuel inefficiency of chemical rockets as well as their limitations in exhaust velocity. Therefore, this project aims to explore an alternative to chemical rockets which can overcome these limitations, namely electric thrusters.

The amount of fuel consumed by any propulsion system is dependent on the performance of the thruster and its specific impulse, I_{sp}. In order to determine the affect of specific impulse on the fuel consumption of a thruster, a relationship can be derived between the specific impulse, I_{sp}, and mass ratio, $\frac{M_{fuel}}{M_{total}}$ [2]:

$$\frac{M_{fuel}}{M_{total}} = 1 - \exp\left(-\frac{\Delta v}{g_0 I_{sp}}\right) \tag{1.1.1}$$

The ratio, $\frac{M_{fuel}}{M_{total}}$, describes the ratio of fuel mass to the mass of the entire spacecraft, which includes fuel, spacecraft structure and payload. A typical chemical thruster fuel mass ratio would be 0.58 (58%) for a mission with a $\Delta v = 3.8 km/s$. This high fuel mass ratio is due to the low specific impulse of chemical rockets which is approximatively $450 - 500$ *seconds*. Equation 1.1.1 shows that the fuel mass ratio can be decreased if the thruster's specific impulse is increased. For example, the same mission can be achieved with a fuel mass ratio of only 0.15 (15%) if electric propulsion is used. Electric thrusters have high specific impulses, which can be up to 8000 *seconds*. However, they also have low thrust outputs which are in the range of milli-Newtons to one Newton.

The high fuel consumption efficiency of electric thrusters results in the total time-integrated thrust output of the thruster to be greater than chemical rockets, given that the time of the mission is long enough. Of the many types of advanced thrusters currently being researched, electric thrusters look the most promising. Electric thrusters are an attractive choice for orbital station-keeping and deep space exploration due to their high specific impulse and relative simple design. However, there are a few limitations and disadvantages for electric thrusters of which the need for high power units to produce thrust is one of the most fundamental limitations.

1.2 Electric Thruster Overview

Electric Thrusters

There are different types of electric thrusters that, rely on different ways for generating thrust. However, the concept stays the same. Ions are produced from a neutral propellant (typically xenon or argon) by means of electrical energy. A large voltage difference and/or magnetic field accelerates the ions to very high velocities in order to generate thrust. This form of propulsion provides very low thrust (typically between $1\mu N - 1N$), but a high exhaust velocity. The exhaust velocity can be in excess of $50,000\ m/s$ and the specific impulse as high as 8000 *seconds* [1]. Electrodes are mostly used for electric thrusters to ionise the propellant. This is feasible for short space missions, but it is impractical for more ambitious space missions as electrodes erode over time. The alternative is to generate the plasma using electromagnetic fields, which eliminates life span issues associated with electrode-based electric thrusters.

Electromagnetic Thrusters

The concept of microwave discharge plasma is fairly comprehensive and well studied. Microwave discharge plasma has been used in various electromagnetic thrusters (MET and VASMIR [3]) and is commonly used in metal industries for cutting metal. Essentially, microwave energy is used to excite a specific electromagnetic field pattern in a microwave resonant cavity or waveguide. These field patterns result in translational and rotational electron excitation. If the rate of atomic ionisation is greater than the rate of recombination per oscillation [1], plasma is produced. A representation of the thruster designed is shown in Figure 1.1, with an example of the ion beam produced in Figure 1.2.

[1] The acceleration energy received by an electron during the first-half cycle of the electromagnetic field needs to be used (collision of particles). Otherwise, the energy will be taken back by the deceleration of the electron on the next half-cycle of the electromagnetic field.

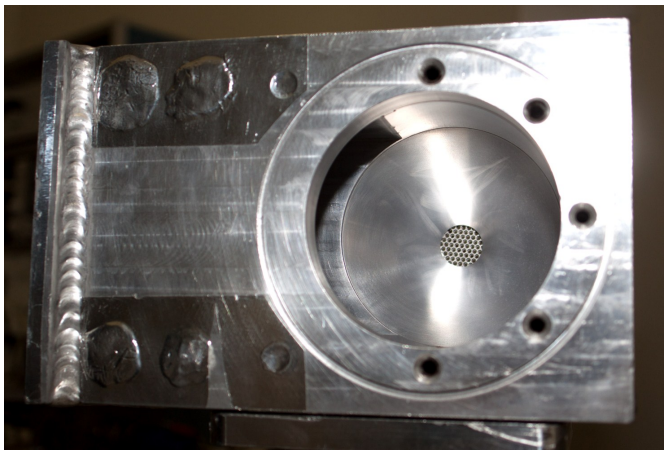

(a) Top View

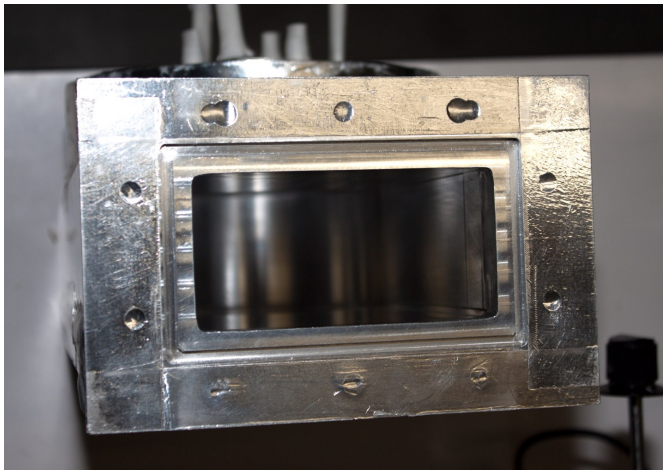

(b) Front View

Figure 1.1: Designed cylindrical resonant cavity for ionisation and acceleration of propellant.

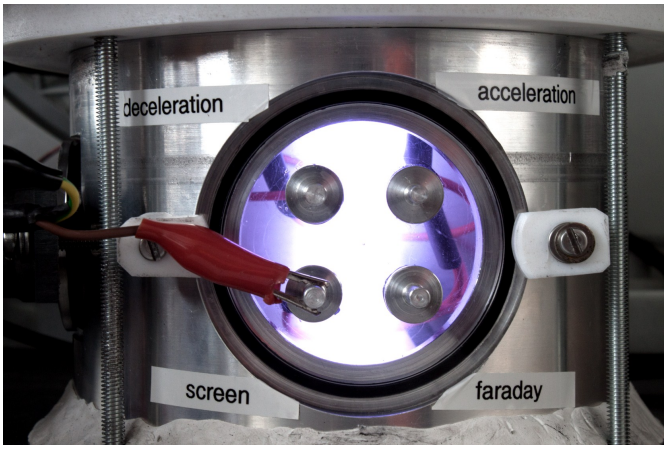

Figure 1.2: Plasma beam produced by designed ion thruster.

1.3 Objectives

In order to examine methods of improving the lifespan and performance of electric thrusters, an electrode-based method of ionisation will be replaced with electromagnetic waves. Therefore, the primary goal of this thesis is to study the method of microwave discharge ionisation for an electric thruster. This project includes designing a radio frequency (RF) Ion Thruster with extraction and acceleration grids. The experimentation includes performing detailed simulations, prototyping and experimentation.

1.4 Outline of Chapters

This thesis presents the study, design and build of an RF Ion Thruster at Stellenbosch University. The structure of this thesis is illustrated by the following flow diagram:

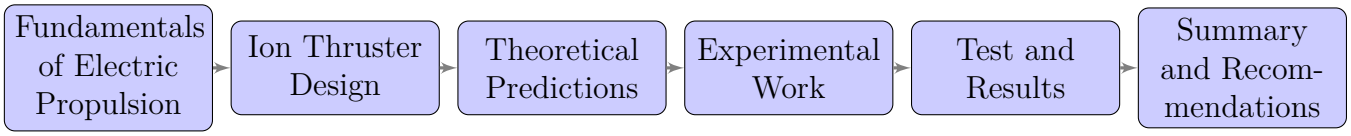

Figure 1.3: Outline of chapters.

Chapter 2 details the theoretical fundamentals needed for the design of the RF Thruster. The thruster design is presented in Chapter 3. Thereafter, the theoretical predictions regarding the performance of the ion thruster are calculated in Chapter 4. The experimental set-up and work conducted is presented in Chapter 5. Subsequently, Chapter 6 verifies the operation of the thruster. The study is concluded with results and recommendations in Chapter 7.

Chapter 2

Fundamentals of Electric Propulsion

This chapter provides the outline of an ion thruster's operation, design and performance to determine the feasibility of electromagnetic thrusters for propulsion. A brief introduction to electric thrusters is given to explain the basic principles of electric propulsion. Following the basic principles, the process of ionising the propellant is discussed to determine the feasibility of electromagnetic ionisation. Thereafter, the different methods of accelerating the ions are studied in order to determine the optimal method for maximum thrust output. Finally, the importance of neutralising the extracted/accelerated ion beam is explained.

2.1 An Introduction to Electric Thrusters

The concept of electric propulsion was originally theorised by Robert Goddard in 1906 and Konstantin Tsiolkovsky in 1911. However, it was only successfully employed in the early 1990's with NASA's Deep Space 1, that completed a comet rendezvous, and SMART 1 which went to the Moon [4]. Since then satellite attitude control and deep space missions have been assigned to hundreds of electric thrusters. For a more detailed history of electric propulsion, please refer to Choueiri's research [5] which contains further references on this subject.

2.1.1 Electric Thruster Types

Electric thrusters are generally described by the method of acceleration. A thruster can be categorized into three main types: Electro-thermal, Electrostatic and Electromagnetic. Firstly, electro-thermal thrusters are devices which use electrical power to heat the propellant. The propellant then expands and flows through a downstream nozzle to produce thrust. An example of an electro-thermal thruster is an Arcjet, which heats the propellant by passing it through a high current arc, as well as a Resistojet, which uses resistively heated elements to heat the propellant.

Secondly, electrostatic thrusters obtain thier thrust by accelerating positively charged ions through a large DC electrical field. This includes, but is not limited to, Gridded Ion Thrusters and Hall Thrusters. An illustration of a Gridded Ion Thruster is shown by Figure 2.1. Figure 2.1 also shows the three main sections namely, ionisation (step 1), acceleration (step 2) and neutralisation (step 3), that will be discussed throughout this chapter.

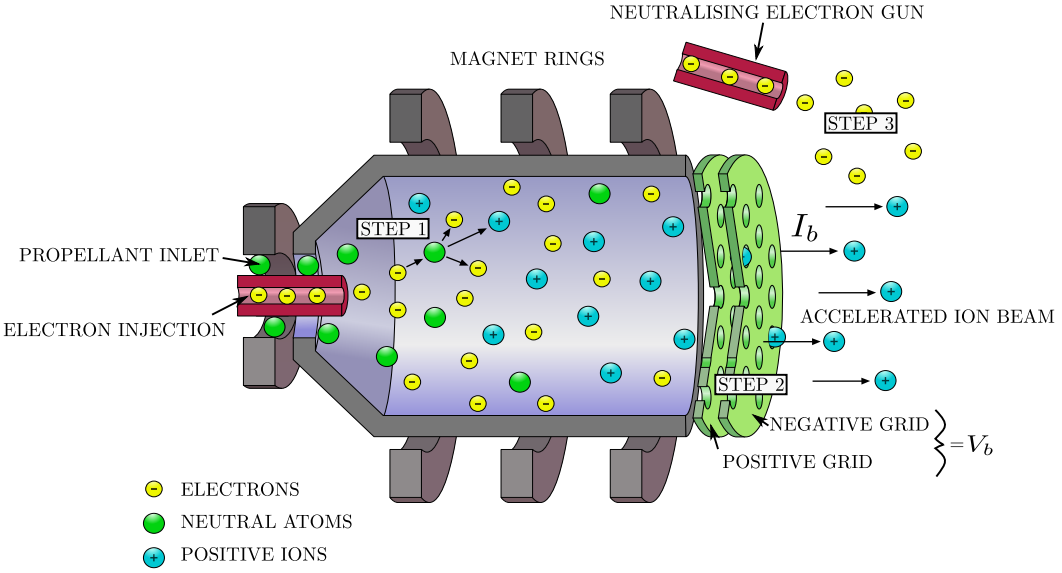

Figure 2.1: Basic gridded ion thruster (adapted from [6]).

Lastly, electromagnetic thrusters produce their thrust by applying electromagnetic forces (Lorentz $F \times B$ forces) in the plasma discharge chamber to accelerate the charged propellant. Magnetoplasmadynamic (MPD) thrusters and the Variable Specific Impulse Magneto-plasma Rocket (VASMIR) are examples of electromagnetic thrusters. Table 2.1 provides a list of the performance levels for these different methods of propulsion. Note, the chemical thruster's efficiency refers to the chemical propellant's energy transferred to thrust. The electrical thruster's efficiency refers to the total amount of electrical energy transferred to thrust.

Table 2.1: Typical performance of various propulsion methods [7].

Type	Thrust (mN)	Specific Impulse (sec)	Efficiency (%)	Duration
Chemical	100-120,000	300-450	87-97	Hours-minutes
Resistojet	200-300	200-350	65-90	Months
Arcjet	200-1000	500-600	25-45	Months
Ion Thruster	0.01-200	2500-3600	40-80	Monts
Hall Thruster	0.01-2000	1500-2000	35-60	Years
MPD	0.001-2500	2000-5000	30-50	Years

2.1.2 Thruster principles

Electric thrusters work on the same basic principles as chemical rockets do, in order to generate thrust, by accelerating a mass and ejecting it from the spacecraft. However, electromagnetic forces are used for gas acceleration in electric thrusters, as opposed to gas combustion, which is used in chemical rockets. In addition, a chemical rocket's thrust is directly proportional to the amount of energy stored in the propellant. Thus no more energy can be put into the rocket than what is contained in the propellant. The solution to this limitation is to separate the energy input to the engine from the propellant flow by applying external energy to the propellant. Then the propellant can receive more energy than what is available from its chemical properties. Electric thrusters are based on this principle by using electrical power to ionise the propellant and eject the energetically charged particles. The result is much higher exhaust velocities (up to $\Delta v = 10^3\ km/s$) than chemical rockets ($\Delta v = 3 - 4\ km/s$), which can either improve the spacecraft's velocity or the payload for a specific Δv.

The thrust of electric thrusters is given by the time rate of change of the momentum[1], which can be written as [7]:

$$T = \frac{d}{dt}\left(m_p v_{ex}\right) \approx \dot{m}_i v_i, \tag{2.1.1}$$

where $\dot{m}_i$ is the ion mass flow rate and v_i is the ion exhaust velocity. The mass flow rate of ions is related to the ion beam current, I_b, by

$$\dot{m}_i = \frac{I_b M}{q}, \tag{2.1.2}$$

where M is the ion mass and q the charge of an ion. The ion exhaust velocity is given by

$$v_i = \sqrt{\frac{2qV_b}{M}}, \tag{2.1.3}$$

where V_b is the net voltage across the grids, as shown in Figure 2.1, through which the ions are accelerated.

In substituting Equation 2.1.3 and Equation 2.1.2 into Equation 2.1.1, the thrust for a single charge propellant can be described as

$$T = \sqrt{\frac{2M}{q}} I_b \sqrt{V_b}\ Newtons\ [7]. \tag{2.1.4}$$

[1]This change is due to the fact that the spacecraft's mass changed over time as the propellant decreased.

Equation 2.1.4 shows that the thrust is proportional to the ion beam current multiplied by the square root of the acceleration voltage, both of which are discussed in section 2.3.

2.2 Ionisation of Propellant

The first process within electric thrusters is the ionisation of the gas which is illustrated by step 1 of Figure 2.1. A typical ion thruster operates by injecting an inert gas into a discharge chamber where it is ionised in order to create plasma.

2.2.1 Plasma

Plasma is typically referred to the 4^{th} state of matter and is composed of freely and randomly moving electrically charged particles, such as ions and electrons, and is almost electrically neutral. The most striking difference between plasma and a gas is the susceptibility of plasma to be affected by electric and magnetic fields. This characteristic of plasma results in plasma to be used as the propellant for all types of electric thrusters. The charged ions and electrons can be accelerated via the electric and magnetic fields, in order to provide thrust. Elsewhere, comprehensive introductions to plasma physics exist [8; 9], as well as details entailing the process of ionisation [10]. Specifically, the scope of the thesis is limited to discussing the physics necessary to understand the operation of ion thrusters.

There are a number of methods for creating plasma. However, the two most conventional methods in electric propulsion are electron bombardment and a process that uses the concept of Electron Cyclotron Resonance (ECR). Electron bombardment describes the process where a propellant atom collides with a high-energy particle [2], which results in an extra electron being removed from the atom. This results in one positively charged ion and two electrons, as illustrated by step 1 of Figure 2.1. The ECR method entails the use of electromagnetic fields acting directly on the electrons of the propellant. This is achieved by coupling high frequency radiation, usually microwaves, with large magnetic fields to heat the propellant to very high temperatures. This causes the electrons to break free from the propellant atoms, thus creating plasma. The major advantage of the ECR method is the increase in expected thruster lifetime that stems from the absence of a hollow cathode or any other electron bombardment device used to ionise the propellant. A more detailed description of ECR is provided in section 2.2.3.

[2]The high-energy particle can be an electron, ion or an atom.

The operating frequencies for RF Thrusters vary. However, the two most widely used frequencies are 13.56 MHz [3] and 2.45 GHz. The electromagnetic fields can be generated in various ways. For instance, RF currents can be circulated in antennas or coils, or an RF voltage can be applied across two parallel plates. The antenna can either be immersed inside the plasma or separated using a dielectric window. However, if the antenna is directly exposed to the plasma, erosion may occur over time, which affects the lifetime of the thruster. Thus, as common practice, the RF antenna is often separated from the plasma with an insulating material. The successful microwave MUSEC-C ECR Ion Thruster built in 2003 [12], that used 4.2 GHz microwave energy and produced 8.1 mN of thrust [7], is a noteworthy example of this insulating material arrangement. This project used a 2.45 GHz magnetron, obtained form a domestic microwave oven, to achieve ionisation. These magnetrons are easy accessible, have low manufacturing costs and are extremely robust. Therefore, the remainder of this section will focus on the use of electromagnetic waves to ionise the propellant.

2.2.2 RF Ionisation

An alternative to producing the plasma with electron discharge, is to generate the plasma using electromagnetic waves at microwave frequencies. The plasma will however only absorb the electromagnetic waves under certain conditions. If the plasma density is too low, or the microwave frequency too high, the electromagnetic fields will not propagate into the plasma. If the electromagnetic waves do however propagate into the plasma, it will result in the resonant heating of the electrons in a magnetic field. The resonant heating will ensure the collision of particles which will result in the ionisation of the neutral propellant.

The propagation of electromagnetic fields in a plasma can be better understood by examining the behaviour of electromagnetic waves in a plasma. The electromagnetic wave behaviour can be described by Maxwell's Equations:

$$\nabla \times \boldsymbol{E} = -\frac{\partial \boldsymbol{B}}{\partial t}, \tag{2.2.1}$$

$$\nabla \times \boldsymbol{B} = \mu_0 \left(\boldsymbol{J} + \epsilon_0 \frac{\partial \boldsymbol{E}}{\partial t} \right), \tag{2.2.2}$$

where $\boldsymbol{J}$ represents the current density in the plasma. In addition, ϵ_0 and μ_0 represents the permittivity and permeability, in that respective order, of free space.

[3] The VASMIR rocket developed by NASA uses a helicon antenna at 13.56 MHz to heat up the plasma to very high temperatures[11].

The electromagnetic behaviour can be analysed by linearising the two equations, Equation 2.2.1 and Equation 2.2.2, using

$$\boldsymbol{E} = \boldsymbol{E}_0 + \boldsymbol{E}_1, \tag{2.2.3}$$

$$\boldsymbol{B} = \boldsymbol{B}_0 + \boldsymbol{B}_1, \tag{2.2.4}$$

$$\boldsymbol{J} = \boldsymbol{j}_0 + \boldsymbol{j}_1, \tag{2.2.5}$$

with $\boldsymbol{E}_0$, $\boldsymbol{B}_0$ and $\boldsymbol{j}_0$ as the equilibrium values of the electric and magnetic fields and currents. The perturbed values are represented by $\boldsymbol{E}_1$, $\boldsymbol{B}_1$ and $\boldsymbol{j}_1$. Linearising the two Maxwell Equations, Equation 2.2.1 and Equation 2.2.2, and knowing that in vacuum, $\epsilon_0\mu_0 = \frac{1}{c^2}$, the two Maxwell's Equations become

$$\nabla \times \boldsymbol{E}_1 = -\frac{\partial \boldsymbol{B}_1}{\partial t}, \tag{2.2.6}$$

$$c^2 \nabla \times \boldsymbol{B}_1 = \frac{\boldsymbol{j}_1}{\epsilon_0} + \frac{\partial \boldsymbol{E}_1}{\partial t}. \tag{2.2.7}$$

Taking the curl of Equation 2.2.6 and time derivative of Equation 2.2.7 and combining them results in

$$\nabla(\nabla \cdot \boldsymbol{E}_1) - \nabla^2 \boldsymbol{E}_1 = -\frac{1}{\epsilon_0 c^2}\frac{\partial \boldsymbol{j}_1}{\partial t} - \frac{1}{c^2}\frac{\partial^2 \boldsymbol{E}_1}{\partial t^2}. \tag{2.2.8}$$

Assuming that the electromagnetic waves are plane waves, the electric field and current density can be presented as

$$\boldsymbol{E} = E e^{i(kx-\omega t)}, \tag{2.2.9}$$

$$\boldsymbol{j} = j e^{i(kx-\omega t)}, \tag{2.2.10}$$

with ω being the cyclic frequency $2\pi f$ and $k = \frac{2\pi}{\lambda}$ the propagation constant. Then Equation 2.2.8 can be written as

$$-k(k \cdot \boldsymbol{E}_1) + k^2 \boldsymbol{E}_1 = \frac{i\omega}{\epsilon_0 c^2}\boldsymbol{j}_1 + \frac{\omega^2}{c^2}\boldsymbol{E}_1. \tag{2.2.11}$$

Note that the electromagnetic waves are transverse waves so that $k \cdot \boldsymbol{E}_1 = 0$. Thus Equation 2.2.11 becomes

$$(\omega^2 - c^2k^2)\boldsymbol{E}_1 = \frac{-i\omega}{\epsilon_0}\boldsymbol{j}_1. \tag{2.2.12}$$

In a plasma the ions are always larger and heavier than the electrons [9]. As a result, the ions of the plasma are too big to move on the fast time scale, represented by Equation 2.2.12, when operating in the microwave frequency range. Thus the current $\boldsymbol{j}_1$ can only come from the electron motion [7]. The perturbed electron current density in a plasma is given by

$$\boldsymbol{j}_1 = -n_e e\boldsymbol{v}_{e1}, \tag{2.2.13}$$

where n_e and $\boldsymbol{v}_{e1}$ represents the plasma density and perturbed electron velocity, respectively. If the assumption is made that the applied magnetic field is zero or that the perturbed electrical field is parallel to the magnetic field, then the the motion for the perturbed electron can be represented as

$$m\frac{\partial \boldsymbol{v}_{e1}}{\partial t} = -e\boldsymbol{E}_1. \tag{2.2.14}$$

Solving the perturbed electron velocity, $\boldsymbol{v}_{e1}$, in Equation 2.2.14 and inserting this into Equation 2.2.13, the perturbed electron current becomes

$$\boldsymbol{j}_1 = -n_e e\frac{\epsilon_0 \boldsymbol{E}_1}{i\omega m}. \tag{2.2.15}$$

Thereafter, when substituting the perturbed current, Equation 2.2.15, into Equation 2.2.12, and solving for the frequency, the dispersion relation [4] for electromagnetic waves in a plasma is given by

$$\omega^2 = \frac{n_e e^2}{\epsilon_0 m} + c^2k^2 = \omega_p^2 + c^2k^2 \text{ [7]}, \tag{2.2.16}$$

with $\omega_p = n_e e^2/\epsilon_0 m$ representing the electron plasma frequency (oscillation).

Now, by substituting $k = \frac{2\pi}{\lambda}$ into Equation 2.2.16, the wavelength for microwaves in a plasma can be presented as

$$\lambda = \frac{2\pi c}{\sqrt{\omega_p^2 - \omega^2}} = \frac{c}{\sqrt{f_p^2 - f^2}}, \tag{2.2.17}$$

[4]Dispersion relation describes the relationship between the angular frequency ω of a wave and its wavenumber $k = \frac{2\pi}{\lambda}$.

where $f_p = \frac{\omega_p}{2\pi}$ represents the plasma frequency and $f = \frac{\omega}{2\pi}$ the microwave frequency. Equation 2.2.17 shows that the microwaves will not propagate into the plasma when the microwave frequency exceeds the plasma electron frequency. This is due to the fact that the wavelength becomes infinitely long when the plasma frequency is exceeded, hence the waves become evanescent and are reflected. Table 2.2 obtained from Goebel *et al.* [7] shows the cut-off frequency, as a frequency that determines the maximum plasma density for a microwave source, for various plasma densities. The corresponding ion current density for a xenon plasma at an electron temperature of 3 electron volt [5], is also demonstrated.

Table 2.2: Cut-off frequency for several plasma densities and the corresponding ion current density for a xenon plasma at $T_e = 3eV$ [7].

Plasma Density (cm^{-3})	Cutoff Frequency (GHz)	J (mA/cm^2)
10^9	0.285	0.0118
10^{10}	0.900	0.118
10^{11}	2.846	1.184
10^{12}	9.000	11.84
10^{13}	28.460	118.4

2.2.3 Electron Cyclotron Resonance (ECR)

In order to aid the microwaves from not being reflected at high plasma densities, the process of ECR can be used. This process allows the cyclic frequency of the electrons of the propellant to correspond to the applied microwave frequency, in the presence of a magnetic field. The alternating electrical field of the microwaves are then synchronised with the gyration period of the free electrons, resulting in an increase in the perpendicular kinetic energy of the electrons (i.e. an acceleration of the electrons). This increase in kinetic energy ensures the collision of electrons with atoms or molecules which results in the ionisation of the neutral gas. This process ensures a greater ionisation efficiency of the propellant and is thus used in the RF ion thruster designed in Chapter 3.

The equation for ECR is derived from Lorentz force equation, which describes the motion for a charge particle with a velocity $\boldsymbol{v}$ in the presence of a magnetic field $\boldsymbol{B}$

$$F = m\frac{d\boldsymbol{v}}{dt} = q(\boldsymbol{E} + \boldsymbol{v} \times \boldsymbol{B}). \tag{2.2.18}$$

[5]Electron volt is the amount of energy obtained when an electron moves across an electrical potential difference of one volt. Although it is usually in units of Joule, in plasma physics it is presented as a unit of temperature in kelvin with 11 604.505 K/eV.

In Equation 2.2.18, the motion of a particle in the ẑ direction in the presence of a magnetic field and negligible electric field can be found:

$$m\frac{\partial v_x}{\partial t} = qBv_y, \tag{2.2.19}$$

$$m\frac{\partial v_y}{\partial t} = qBv_x, \tag{2.2.20}$$

$$m\frac{\partial v_z}{\partial t} = 0. \tag{2.2.21}$$

Taking the time derivative of Equation 2.2.19 and Equation 2.2.20 and solving the velocity in each direction gives

$$\frac{\partial^2 v_x}{\partial t^2} = \frac{qB}{m}\frac{\partial v_y}{\partial t} = -\left(\frac{qB}{m}\right)^2 v_x, \tag{2.2.22}$$

$$\frac{\partial^2 v_y}{\partial t^2} = \frac{qB}{m}\frac{\partial v_x}{\partial t} = -\left(\frac{qB}{m}\right)^2 v_y. \tag{2.2.23}$$

From this, the electron cyclotron frequency can be represented as

$$\omega_c = \frac{|q|\mathbf{B}}{m}, \tag{2.2.24}$$

with q and m representing the charge and mass of an electron, respectively.

The ionisation of the propellant can only be achieved if the kinetic energy of the electrons are larger than the atom or molecule's ionisation energy. The ionisation energy describes the amount of energy required to remove an electron from an atom, or molecule, in its gaseous state. The ionisation energy is typically specified in electron volts (eV) or kJ/mol with 96.485 $kJ/mol = 1\ eV/particle$. The first three ionisation energies are defined as:

$$1^{st}level : X \rightarrow X^+ + e^-,$$

$$2^{nd}level : X^+ \rightarrow X^{2+} + e^-,$$

$$3^{rd}level : X^{2+} \rightarrow X^{3+} + e^-.$$

The amount of energy needed to ionise certain elements to three different levels are illustrated below in Table 2.3.

Table 2.3: Ionisation energy of different elements for three ionisation levels in kJ/mol.

Element	$1^{st}level$	$2^{nd}level$	$3^{rd}level$
Hydrogen	1312.0	-	-
Xenon	1170.4	2046.4	3099.4
Argon	1520.6	2665.8	3931.0

Although the method of RF ionisation enables direct heating of the propellant's electrons, the microwaves can only add energy to the electrons if collisions occur. Without collision, the energy an electron receives during its acceleration on each half-cycle of its cyclotron motion is cancelled out by the deceleration it encounters in the field on the next half-cycle. Therefore a minimum pressure is needed, at which sufficient collisions can occur, to start the ionisation of the propellant. After the ionisation is started, coulomb collisions will help transfer the motion of the electrons in the microwave field into heating, thus reducing the pressure required for operation. Lubey [13] found that the nominal pressure for operation is approximately $10^{-3}\ Torr$ in order to achieve sufficient collisions to sustain the discharge.

2.2.4 Combustion Chamber

In microwave ion thrusters, the 'combustion' chamber is in fact a microwave cavity designed to produce standing electromagnetic waves that accelerate the electrons and result in the ionisation of the propellant. The cavity is typically given a circular geometry with certain dimensions. The dimensions determine the resonant field distributions (modes) that can exist inside the cavity, and hence, where the greatest electrical field intensities are. Selecting a proper resonant mode for the cavity will determine where the maximum field intensity is and thus, where the maximum plasma density is. The next few subsections will discuss the basic theory for the design of a microwave cavity with the correct resonant modes for the ionisation of a neutral gas.

2.2.4.1 Dielectric Materials Properties

The current density $\boldsymbol{J}$ can be represented as [14],

$$\boldsymbol{J} = (\sigma + j\omega\epsilon)\boldsymbol{E}, \tag{2.2.25}$$

with σ and ϵ representing the conductivity and permittivity of the material, respectively. The conductivity σ represents the part of the electric current responsible for any movement

of free charges in the material. Equation 2.2.25 shows that the imposing of an electric field into a material will result in electrical currents. The permittivity is composed of real and imaginary components and is represented in complex format as:

$$\epsilon = \epsilon' - j\epsilon''. \tag{2.2.26}$$

The permittivity can be normalised with free space to become

$$\epsilon = \epsilon_0\epsilon_r' - j\epsilon_0\epsilon_r'', \tag{2.2.27}$$

where ϵ_r' is called the relative permittivity or dielectric constant. In contrast, ϵ_r'' is called the loss factor or dissipation factor. The dielectric constant represents the related stored energy within the medium, whereas the loss factor represents the dissipation of energy within the medium.

Inserting Equation 2.2.27 into Equation 2.2.25 yields:

$$\boldsymbol{J} = (\sigma + \epsilon_0\epsilon_r''\omega)\boldsymbol{E} + j\epsilon_0\epsilon_r'\omega\boldsymbol{E}. \tag{2.2.28}$$

Effect of Dielectric Loss of Material

Materials, like ceramics and glass, are frequently used in high frequency applications where a window is needed to allow fields into the applicator. The low dielectric losses (ϵ_r'') of glass, like quartz, ensures that very little microwave energy is absorbed by the glass itself.

Effect of Conductivity of Material

The conductivity of materials can have a very strong impact on shaping the electric fields inside a cavity. For example, a solid sheet of aluminium will reflect all the microwaves, yet a very thin sheet will serve as an excellent absorber of microwaves. The charge that plasma has, as explained in 2.2.1, causes plasma to have dielectric losses of a conductive body in a microwave cavity. The conductivity of most industrial plasma is based on Lorentzian plasmas, and is given by

$$\sigma = \frac{e^2 n_e}{m_e v_{col}} \text{ [15]}, \tag{2.2.29}$$

where $e = 1.602 \times 10^{-19}$ represents the charge of the electron. The electron density in m^3 is represented by n_e. The mass of the electron is represented by $m_e = 9.109 \times 10^{-31} kg$, and v_{col} represents the electron collision frequency per second. The conductivity

of plasma ranges from 200 to 10,000 S/m. The properties of the plasma is different prior to 'ignition' and during the sustainment of the plasma. This is due to the non-linear nature of plasma and is a consideration that needs to be kept in mind when designing the ionisation chamber.

2.2.4.2 Selection of a Resonant Cavity Mode

Resonance is used to increase the intensity of field interaction with the application load. The properties of the material being heated play an important role in determining the necessity of using resonance. If the material has a high dielectric loss, resonance may not be needed because low levels of electrical fields will be able to heat the material. As a result of gas [6] having very weak interactions with electromagnetic fields, the process of resonance is necessary. The two transverse modes that are used in circular resonators are the trans-electric (TE) mode and the trans-magnetic (TM) mode. In each of these modes, the axial fields are defined as either magnetic fields (TE mode) or electric fields (TM mode).

Electromagnetic field distributions can be calculated by solving Maxwell's Equations. The derivations of these equations can be tedious and as such only the results are shown below. The reader is referred to reference [16] for a complete derivation. The resonant frequency that exists in a TM or TE mode cavity is given as:

$$\omega_{mnp} = \frac{1}{\sqrt{\mu\epsilon}}\sqrt{\left(\frac{X_{mn}}{a}\right)^2 + \left(\frac{p\pi}{h}\right)^2}, \tag{2.2.30}$$

where a and h are the internal radius and height of the cylindrical cavity, respectively. The constant p refers to the number of integer half-wavelengths that may exist inside the resonant cavity. The order of Bessel function for the TM and TE type modes are represented by X_{mn}. Table 2.4 lists some of the values of the different modes.

Table 2.4: Some values of X_{mn} for Bessel function [16].

n	X_{0n}	X_{1n}	p_{2n}
0	2.4049	3.8318	5.1357
1	5.5201	7.0156	8.4173
2	8.6537	10.1735	11.6199

A commercial microwave magnetron, with an operating frequency of 2.45 GHz, was used for the purpose of ionising the gas in this thesis. From Equation 2.2.30, it can be noted that various combinations of diameters and heights will result in a resonant frequency of 2.45 GHz. Figure 2.2 shows the various TM and TE resonant modes for a cylindrical

[6] The propellant is in a gaseous state prior to ionisation.

cavity with various dimensions. The dimensions of the cavity must be as compact as possible in order to conserve weight and confine microwave energy to a smaller region. A smaller region will increase the energy density inside the cavity and will facilitate the process of ionisation. As a result, the only two modes that are of interest are the TE_{111} mode and the TM_{010} mode. A TM_{010} mode cavity has the advantage of producing uniform electrical fields in the axial direction, with a maximum intensity in the centre of the cavity. Thus, the highest plasma density will be found in the centre of the cavity along the axial direction, which will aid the extraction and acceleration process discussed in section 2.3. Therefore, this thesis will focus on a TM_{010} cavity in order to ionise the propellant.

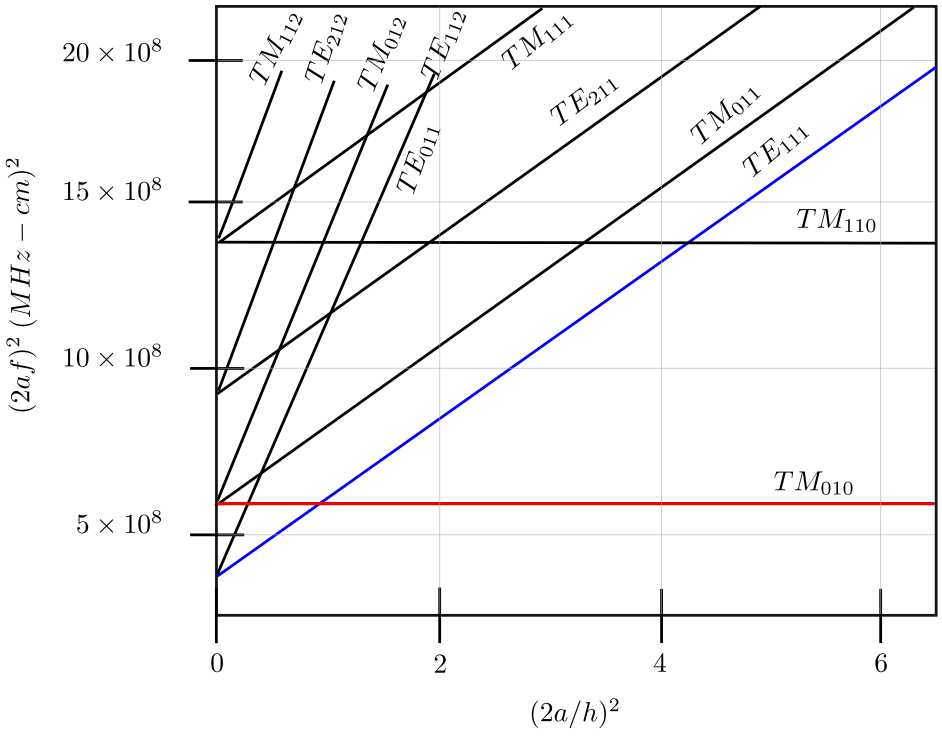

Figure 2.2: Resonant mode chart for a cylindrical resonant cavity [17].

2.2.4.3 TM_{010} Mode Cylindrical Cavity

The circular TM_{010} mode cavity produces uniform electrical fields and more intense fields in the area of interest for a fixed power input. In addition, they are also very efficient heaters with a large quality factor (Q-value). Therefore, it is possible to create very high electrical fields at modest power levels, prior to ionisation of the neutral gas [14]. This advantage makes the single-mode cavity a favourable option for ionising the propellant.

Solving Maxwell's equations again, with the proper boundary conditions for a cylindrical cavity, the field distribution of the resonant cavity can be obtained. The complex field

distributions can be expressed in cylindrical coordinates with the following set of equations [16]:

$$\boldsymbol{E}_r = -j\frac{1}{\omega\mu\epsilon}\frac{\partial^2\psi}{\partial r\partial z},$$

$$\boldsymbol{E}_\theta = -j\frac{1}{\omega\mu\epsilon}\frac{1}{r}\frac{\partial^2\psi_z}{\partial\theta\partial z},$$

$$\boldsymbol{E}_z = -j\frac{1}{\omega\mu\epsilon}\left(\frac{\partial^2}{\partial z^2} + \epsilon\mu\omega^2\right)\psi, \tag{2.2.31}$$

$$\boldsymbol{H}_r = \frac{1}{\mu r}\frac{\partial\psi}{\partial\theta},$$

$$\boldsymbol{H}_\theta = \frac{1}{\mu}\frac{\partial\psi}{\partial r},$$

$$\boldsymbol{H}_z = 0.$$

The Helmholtz wave equation can be used to express the equation for ψ in a TM_{010} cylindrical cavity as [16],

$$\psi(r,\theta,z) = J_m\left(\frac{X_{mn}p}{a}\right)cos(m\theta)cos\left(\frac{p\pi z}{h}\right) = J_0\left(\frac{X_{01}r}{a}\right). \tag{2.2.32}$$

Equation 2.2.32 can be substituted into each component of Equation 2.2.31 and normalised with $-j\omega$. Following the substitution, the electric and magnetic field component for a TM_{010} cavity, with radius a and radial distance r, can be expressed as [18]:

$$\boldsymbol{E}_z = J_0\left(\frac{X_{01}r}{a}\right), \tag{2.2.33}$$

$$\boldsymbol{H}_\phi = j\left(\frac{X_{01}}{\eta}\right)J_1\left(\frac{X_{01}r}{a}\right), \tag{2.2.34}$$

where $\eta = 377\ \Omega$ is the impedance of free space. J_0 and J_1 represents the Bessel functions of the first zero and first order respectively. Whereas, $j = \sqrt{-1}$ shows that the E and H fields are out of phase. Thus the TM_{010} resonant mode is seen to have a azimuthal magnetic field distribution, as well as an axial electrical field distribution, as illustrated by Figure 2.3.

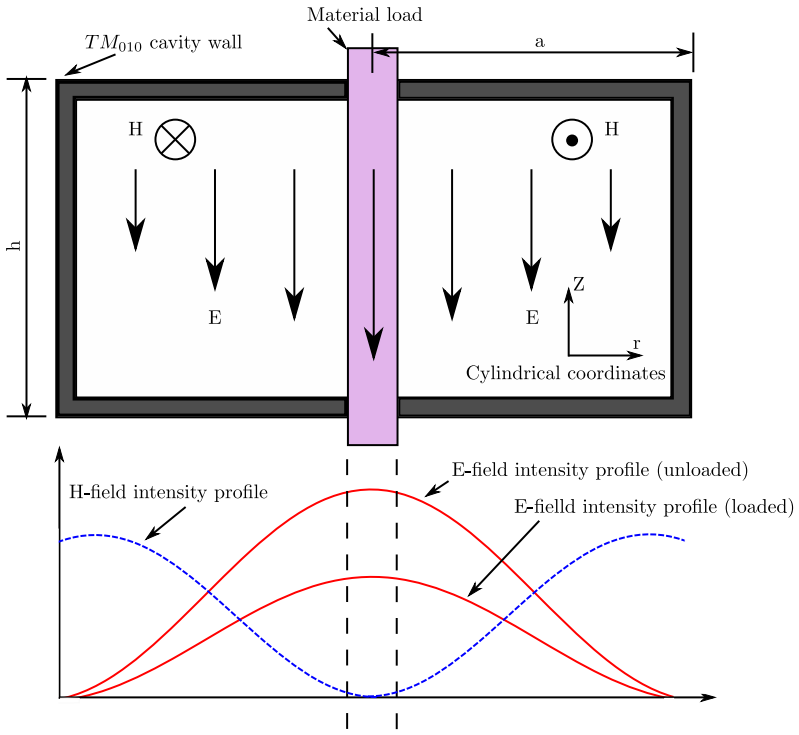

Figure 2.3: Field configuration intensity for a TM_{010} cylindrical cavity (adapted from [14]).

The electrical field distribution is a function of the radial distance with a maximum intensity at the centre axis of the cavity. The maximum electrical field intensity will contribute to the ionisation process of the thruster. The magnetic field distribution is also a function of the radial distance from the centre of the axis. However, the field distribution is coupled with the first order of the Bessel function J_1, instead of the zero order Bessel function J_0, as with the electric field. As a result, the greatest magnetic field intensity is approximately 76% from the centre axis. Figure 2.4 provides an illustration of the maximum field distributions.

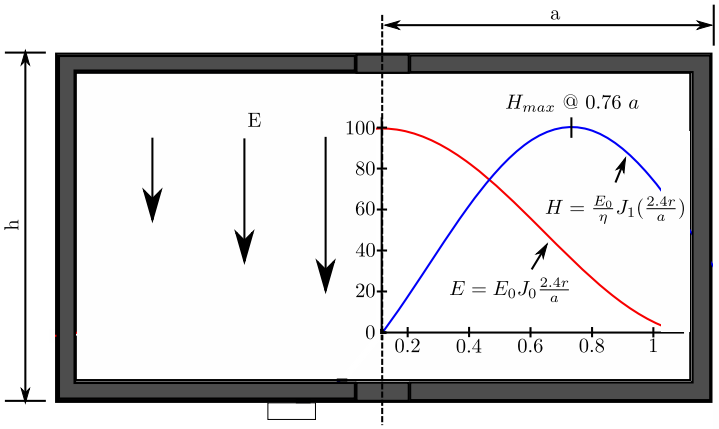

Figure 2.4: Maximum electric and magnetic field distribution in an empty TM_{010} cylindrical cavity (adapted from [14]).

The resonant frequency (in Hz) of an empty TM_{010} cavity, with internal radius a and height h (in meters), can be expressed by applying Equation 2.2.35, as [18]

$$f_0 = \frac{X_{01}}{2\pi a\sqrt{\mu_0\epsilon_0}}, \tag{2.2.35}$$

where μ_0 and ϵ_0 are the permeability and permittivity of free space, respectively. The Bessel functions first root of first type and order zero is represented by $X_{01} = 2.4049$. In a TM_{010} cavity, it is important to note that the resonant frequency is independent of the cavity height. However, the resonant frequency is affected by the dielectric properties of the load introduced into the cavity. The load will result in a decrease of the resonant frequency and as such, the diameter of the cavity should be reduced to maintain the same resonant frequency. For the purpose of this project, the argon gas used does not look like a 'load' prior ionisation. This is due to the low dielectric constants of gas which provides very weak interactions with electromagnetic fields. After ionisation the resonant frequency will be affected, however, this is not a concern, provided the plasma is sustained.

2.2.4.4 Quality Factor

The Quality Factor (Q-value) is an indication of the power dissipation in resonant circuits and is defined as

$$Q = \frac{W_m + W_e}{P_l}, \tag{2.2.36}$$

with W_m and W_e representing the energy stored in the magnetic and electric field, respectively, whereas P_l is the power lost per second in Watts.

A high Q-value indicates high accuracy and narrow bandwidth for a cavity resonator. The unloaded Q-value (Q_0) for an empty TM_{010} cavity is represented as [14]

$$Q_0 = \frac{\eta}{R_s}\frac{p_{01}}{2\,(a/h+1)}, \tag{2.2.37}$$

where $R_s = \sqrt{\pi f\mu_0/\sigma}$ is the surface resistance of the cavity's metal. The impedance of free space is represented by $\eta = 377\ \Omega$. Similar to the electrical field intensity decreasing with a load, the Q factor is also reduced when a load is introduced. The extent of the Q factor reduction is dependent on the size and dielectric properties of the load. In practice, the cavity has to be coupled with an external circuit which has its own Q-value (Q_e). The coupling, which is discussed in the following section 2.2.4.5, will reduce the Q-factor of the entire system.

2.2.4.5 Coupling Method

The method used to introduce the microwave energy into the cavity is a crucial part in the process of exciting the specific resonant mode. Regardless of which cavity or transmission line type is being used, two methods can be considered, namely: electric field antenna coupling and magnetic flux linkage.

Electric Field Antenna Coupling

The magnetron can be coupled to the ionisation chamber in order to excite a TM_{010} mode by using the electric field antenna coupling method. The magnetron's stub antenna is placed parallel to the electric fields of the cavity, as shown by Figure 2.5. Although this is the simplest method of coupling the magnetron to the cavity, there are drawbacks to consider. The amount of energy that is reflected by the cavity can get coupled to the antenna of the magnetron, which can lead to heating and magnetron failure. Additionally, in this method, there is no simple way of determining the transmitted and reflected power of the cavity. The amount of power being absorbed by the neutral gas and plasma can only be calculated if this important parameter is known, which ultimately impacts the efficiency of the thruster.

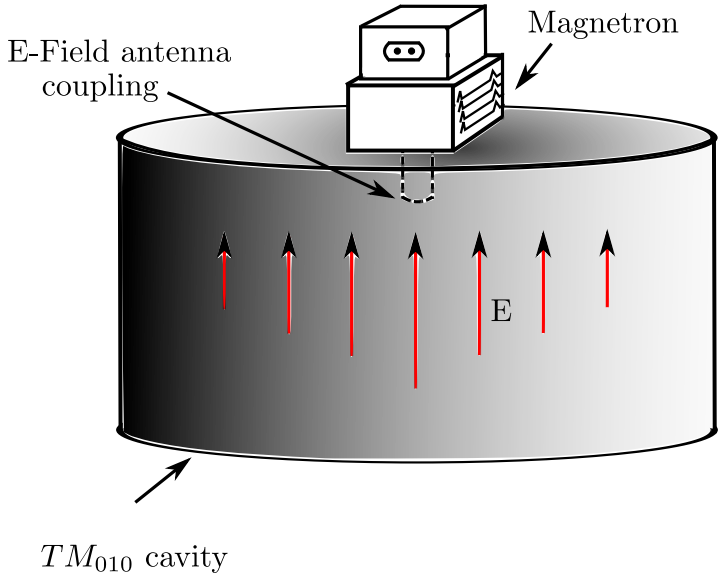

Figure 2.5: Electric field antenna coupling with magnetron for a TM_{010} mode cavity.

Magnetic Flux Linkage Coupling

The magnetron can also be coupled to the ionisation chamber to excite a TM_{010} mode using a magnetic flux linkage via a waveguide, as shown by Figure 2.6. In this method, a circulator can be introduced to the system to avoid the magnetron from overheating. In addition, the transmitted and reflected power can be determined by introducing a bi-directional microwave coupler to the system. Nevertheless, the drawbacks of this coupling method includes big waveguides and precise tuning devices that are needed to calculate the reflected power, and match the impedance of the magnetron and waveguide to the cavity.

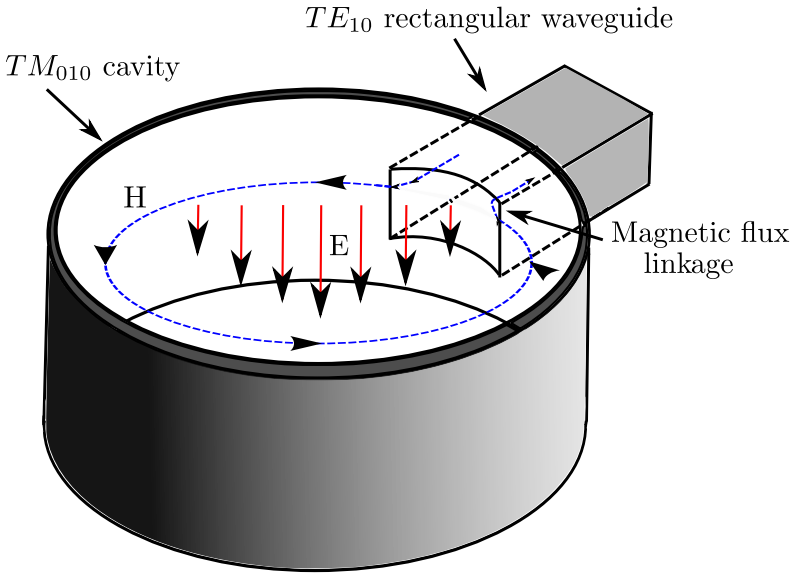

Figure 2.6: Magnetic flux linkage coupling with a TE_{10} waveguide for a TM_{010} cylindrical cavity (adapted from [14]).

In comparing these two methods for coupling, the latter was found to be more suitable for this project. The effect of parameters, such as plasma density, vacuum pressure and microwave power, can be studied with the available transmitted and reflected power information. The cavity can also be precisely tuned to create and sustain a high power plasma discharge which will increase the efficiency of the thruster.

The dimension and cut-off frequency of the rectangular waveguide, necessary for the magnetic flux linkage, are calculated from [16]

$$(f_c)_{min} = \frac{1}{2\pi\sqrt{\mu_0\epsilon_0}} = \sqrt{(\frac{m\pi}{a})^2 + (\frac{n\pi}{b})^2}, \tag{2.2.38}$$

where a is the waveguide width, b the waveguide height and mn the 'mode' of operation. The cut-off frequency must always be lower than the resonant frequency to ensure correct operation of the designed resonant cavity.

The waveguide used for magnetic flux linkage is normally coupled with an iris. The function of the iris is to ensure impedance matching between the cavity and the waveguide. In a situation where a 'heavy' microwave load is introduced, critical coupling will occur with a wider iris. However, as the load changes, the dimension of the iris needs to change to maintain critical coupling, or else some or all of the microwave energy will be reflected. The effect of coupling can be explained by examining the equivalent circuit for a cylindrical TM_{010} cavity.

2.2.4.6 Equivalent Circuit for a Cylindrical TM_{010} Cavity

Figure 2.7 represents the equivalent circuit for cylindrical resonant cavity [19]. Port 1 represents the feeding port, which consists of source V_s and internal impedance R_c. The length between port 1 and port 2 represents the transmission line and the impedance $R_s + jX_s$ between port 2 and port 3 illustrates the coupling structure. Port 3 represents the location of the resonator/cavity. The resistance R represents the dissipation inside the cavity caused by dielectric and conductor losses of the cavity.

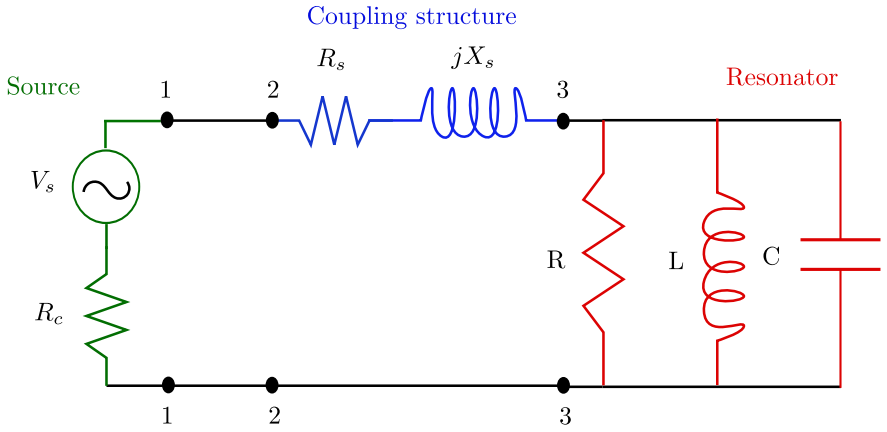

Figure 2.7: The equivalent circuit for a TM_{010} cylindrical cavity [19].

Effect of Coupling

Norton's equivalent (see Figure 2.8) of Figure 2.7 can be used to explain the effect of coupling. The impedance $R_c + R_s + jX_s$ can be transformed into $R_{ex} + jB_{ex}$. The Norton equivalent circuit shows that the external circuit influences the resonator in two ways. Firstly, jX_{ex} detunes the resonant frequency of the cavity and secondly, R_{ex} affects the quality factor of the cavity.

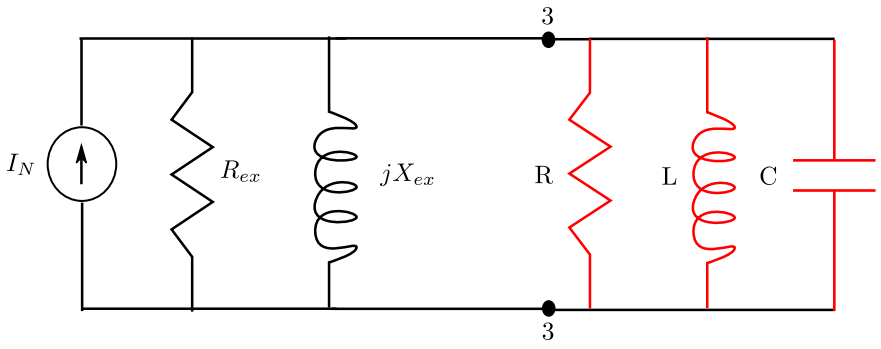

Figure 2.8: Norton's equivalent circuit for port 2 [19].

2.3 Extraction and Acceleration

The extraction and acceleration of the ionised particles to high velocities is the second, and most important part, of an electric thruster. Electrostatic acceleration (i.e. gridded thrusters) and electromagnetic acceleration (i.e. grid-less thrusters) are the two main methods of acceleration.

Electrostatic Acceleration

Gridded thrusters encompass electrically biased multi-aperture grids that are spaced only a few millimetres from each other inside a thruster. The bias potentials cause the positively charged particles, created during the ionisation process, to be extracted and accelerated through the apertures, as shown by step 2 of Figure 2.1. The essential elements needed for this method are shown below by Figure 2.9.

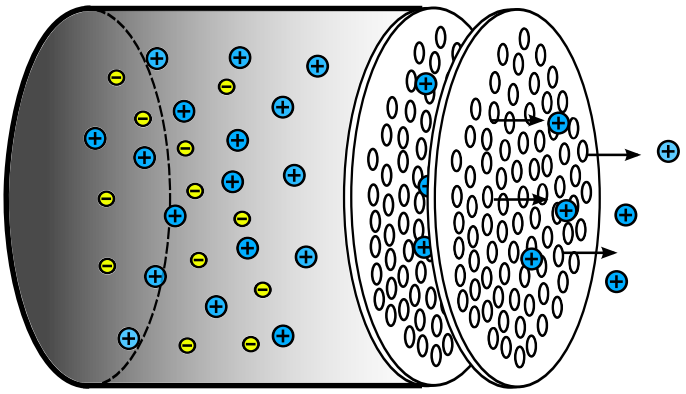

Figure 2.9: Electrostatic acceleration.

Electrostatic acceleration is the most fully developed acceleration method with a substantial body of literature available ([7; 2; 20]). Attainable thrust depends only on the mass of the ion, exhaust speed and the maximum ion beam current that can be accommodated by the grids. Electrostatic acceleration has been successfully implemented on various thrusters. Examples include the XIPS thruster that was launched in 1999 on a Hughes/Boeing 702 satellite [21], and the NEXT thruster, from NASA, which operated for more than 48,000 hours [22; 23]. However, the limited performance, due to the space charge effect, is a great disadvantage for this acceleration method. The maximum amount of ion current a gridded ion thruster can extract and focus into a beam for a given voltage is known as the space charge limit.

Electromagnetic Acceleration

In order to overcome the space charge limit, electromagnetic acceleration uses a gridless method of acceleration. To illustrate this concept in its simplest form, consider an ionised gas which is subjected to an orthogonal electric and magnetic field (see Figure 2.10) as it passes through a channel. The current density $\boldsymbol{j} = \boldsymbol{E} + \boldsymbol{u} \times \boldsymbol{B}$ that will flow through the channel, which is parallel to the electric field $\boldsymbol{E}$, will interact with the magnetic field $\boldsymbol{B}$ to generate a force $f_B = \boldsymbol{j} \times \boldsymbol{B}$ along the channel. The advantage of this form of acceleration is that both ions and electrons contribute to the thrust. Additionally, there is no fundamental space charge limitation on the plasma density like that provided by gridded thrusters. However, the process of electromagnetic acceleration is not as simple. The current produced from the charged particles generates an extra magnetic field, which causes ions and electrons to act on their own electric and magnetic fields. Extensive knowledge of thermodynamics and electromagnetic theory is required to predict the outcome.

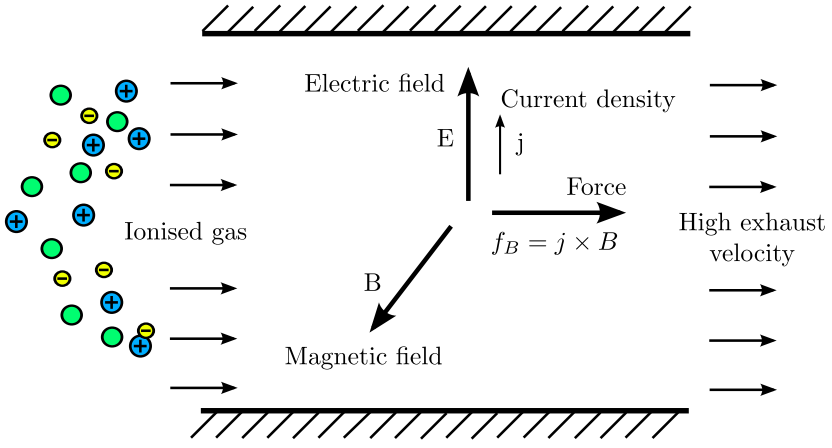

Figure 2.10: Electromagnetic acceleration.

The original idea of this project was to study and implement the method of electromagnetic acceleration to the thruster, in order to ensure a greater lifespan with an absence of erosion on grids and a maximum plasma acceleration. However, the implementation was found to be far too complex for the amount of time available. As a result, the focus of this thesis shifted and was instead placed on electrostatic acceleration. Thus, the remainder of this section will focus on the method of grid-based acceleration.

2.3.1 Grid Configuration

Various factors, such as the lifetime and performance of the spacecraft, as well as the propellant being used, impact the design of electrostatic acceleration grids. Typically, two grids are contained in the design. The first grid, called the screen grid, is kept at a high positive voltage relative to the system (around +1500 V). The second grid, called the acceleration grid, is kept at a negative voltage relative to the system (around -500 V). Due to the high voltage difference (around 2000 V), the positively charged ions are extracted. These ions are focused through the screen grid and then accelerated by means of the acceleration grid. Normally when exiting the grid system, the positively charged ion plume is neutralised. This will prevent any back-streaming of charged particles[7], which is an action that will have a negative impact on the thruster. A more detailed description of neutralisation is discussed in section 2.4.

2.3.2 Plasma Sheaths

In order to understand the design of the 'grid system', the sheaths formed at the boundaries of the plasma needs to be studied. The boundaries of the plasma represents the sections through which charged particles enter and leave the plasma and the thruster. The plasma, that is created inside the 'combustion chamber', will form density and potential variations at the boundaries, in order to satisfy particle balancing for a quasi-neutral plasma. These potential variations are due to the different mobilities and temperatures of electrons and ions, and are called sheaths.

If the potential gradient is small in comparison to the electron temperature T_e, a Debye sheath is established. If the potential is much greater than T_e, a Child-Langmuir sheath is established [10]. A Child Langmuir sheath is obtained when the potential gradient across the sheath is sufficiently large, causing electrons to be repelled from the sheath's thickness. The electron density is essentially zero at the sheath's edge. The Child-Langmuir sheaths ensure that ions are accelerated through the multi-aperture grids with reasonable direction. In addition, it also ensures that the electrons are reflected. The extraction of electrons will increase the extracted current density, which will have a negative impact on

[7]The back-streaming is a result of the negative potential acceleration grid which attracts the positively charged ions.

the performance of the thruster. This is because there is a maximum current a gridded ion thruster can extract. Therefore the current must be mostly due to the large ions that will produce a greater amount of thrust in comparison with the small electrons. The equation for Child-Langmuir can be written as [7]

$$J_i = \frac{4\epsilon_0}{9}\left(\frac{2e}{M}\right)^{1/2}\frac{V^{3/2}}{d^2}. \tag{2.3.1}$$

The equation was derived by Child [24] in 1911 and Langmuir [25] in 1913. The equation states that the current per unit area that can pass through a sheath is limited by the space charge effect, and is proportional to the voltage $V^{3/2}$ divided by the sheath thickness d^2.

Figure 2.11 illustrates the Child-Langmuir length for two single charged ion current densities. As can be seen in Figure 2.11, a 0.2-cm-diameter aperture has a maximum space charge current density for argon gas of approximately 8 mA/cm^2 at 1500 V. Thus, the total ion current per aperture is only 0.39 mA. Equation 2.1.4 indicates the total thrust for this current and voltage to be only about 18μN. Although this amount of thrust is very low, if multiple apertures are used, then the amount of thrust will greatly increase.

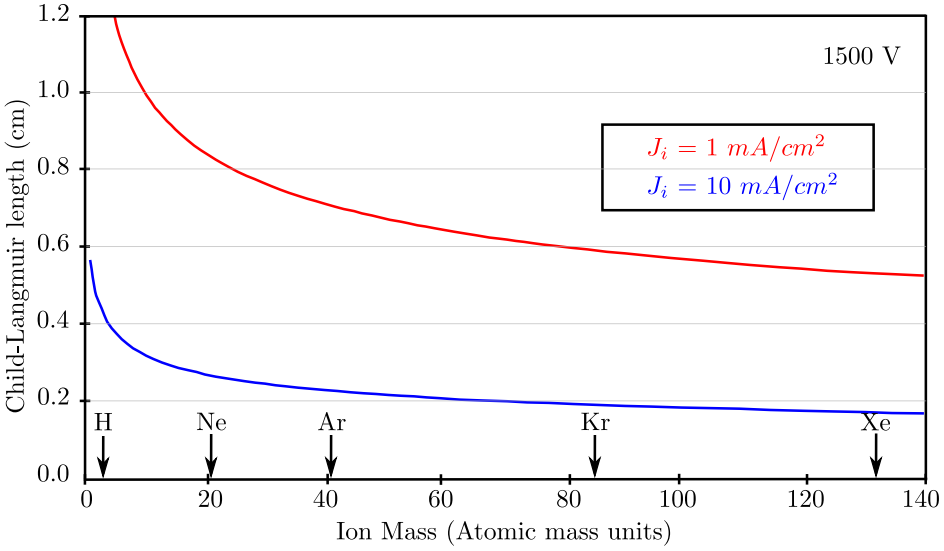

Figure 2.11: Child-Langmuir sheath length versus various propellants at 1500 V acceleration voltage for two ion current densities [7].

2.3.3 Ion Acceleration

The ideal grid design will extract and accelerate all the ions that approach the grid-system whilst blocking the electrons and neutral gas outflow. If the grid design only contains an acceleration grid, then the only ions that are accelerated through the aperture are those that arrive on axis with the apertures. The ions that are not aligned with the apertures are accelerated into the acceleration grid itself, which will cause rapid erosion. Therefore, a 'screen' grid with apertures aligned to the acceleration grid is introduced. This will help prevent unwanted collision of ions, as shown by Figure 2.12. The screen grid typically has a positive potential that will help confine some of the electrons and ensure that the ions that collide with the grids have relatively low energy.

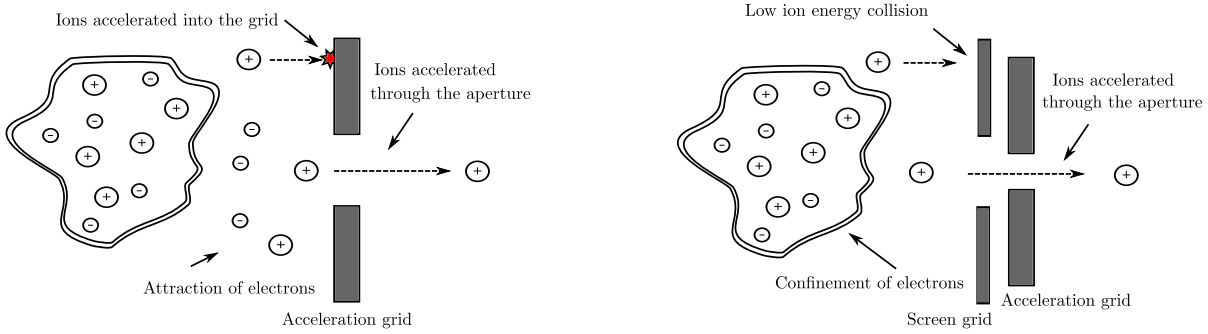

(a) Acceleration of ions in absence of screen grid.

(b) Acceleration of ions with screen grid present.

Figure 2.12: Effect of a screen grid on charged particles in a plasma.

The screen and acceleration grids, together, are known as the ion optics. Figure 2.13 shows the five degrees of freedom for the ion optics: screen grid thickness; acceleration grid thickness; screen grid aperture diameter; acceleration grid aperture diameter; and the distance between the two grids.

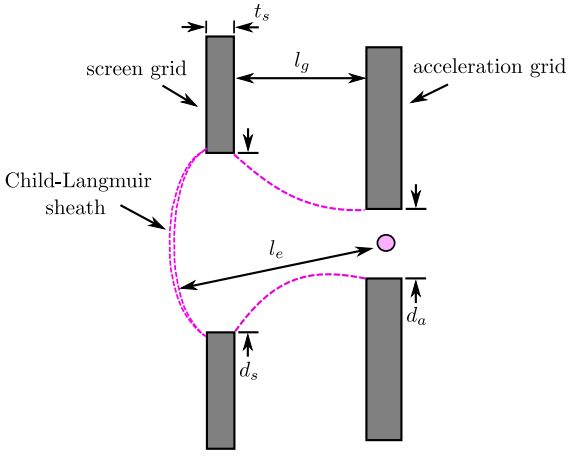

Figure 2.13: Plasma sheath layout for a two grid system.

The equation that represent this configuration is obtained from Equation 2.3.1 for a non-planar sheath as

$$J_{max} = \frac{4\epsilon_0}{9}\sqrt{\frac{2e}{M}}\frac{V_T^{3/2}}{l_e^2}, \tag{2.3.2}$$

where V_T is the total voltage between the grids and M the atomic mass of the propellant. The sheath thickness, l_e, is given by [7]

$$l_e = \sqrt{(l_g + t_s)^2 + \frac{d_s^2}{4}}. \tag{2.3.3}$$

The maximum ion current density, as expressed in Equation 2.3.2, shows that there is a maximum thrust density for an ion thruster. This maximum thrust density can be expressed from Equation 2.1.1 as [20],

$$\frac{T}{A_g} = \dot{m}_i\dot{v}_i = \frac{jM\dot{v}_i}{q} = \frac{8\epsilon_0}{9}T_g\left(\frac{V_T}{l_e}\right)^2 = \frac{8\epsilon_0}{9}\frac{A_{open}}{A_g}E^2, \tag{2.3.4}$$

where A_{open} and A_g are the grid open and total grid area, respectively. The effective electrical field in the acceleration gap is represented by $E = \frac{V_T}{l_e}$. Although the exhaust velocity depends on the charge-to-mass ratio M (see Equation 2.1.3), the thrust density is independent of the parameter.

2.4 Neutralisation of Ion beam

Neutralisation is a very important process that directly affects the performance and lifespan of an ion thruster. This process is shown in step 3 of Figure 2.1. A large amount of positively charged ions are expelled by the ion thruster and as such, an equal amount of negative charge electrons need to be expelled, in order to keep the net charge of the exhaust beam neutral. The neutralisation process prevents positive charge ions to accelerate backwards into the acceleration grid. This action, known as back-streaming, erodes the acceleration grids which reduces the lifespan and ultimately decreases thrust. The neutraliser is located on the end of the thruster and normally consists of a hollow-cathode that emits the necessary electrons.

2.5 Summary

In this chapter, the fundamental theory of electric thruster, was studied in order to determine the feasibility of electromagnetic thrusters for propulsion. The different methods of ionising the neutral propellant, with microwaves, were presented. Then the theory was examined and it was found that a circular TM_{010} cavity was the most ideal method for ionising the propellant. The two different methods of accelerating the ions, namely electromagnetic acceleration and electrostatic acceleration, were discussed. Thereafter, the necessary theory for electrostatic acceleration with grids, was reviewed. Finally, the necessity of neutralisation for electric propulsion was discussed.

Chapter 3

Ion Thruster Design

The previous section provided a broad perspective on the design of the electromagnetic ion thruster. The need for a maximum electrical field to be produced by the 'combustion chamber', in order to ionise the propellant, was demonstrated. This maximum electrical field was seen to be necessary due to the weak electromagnetic field interactions that a neutral gas has prior to ionisation. The process of electron cyclotron resonance was deemed appropriate, in the presence of a large magnetic field, to assist in the production of a large plasma density with a certain microwave frequency. The magnetic field will not only assist in the process of ECR but will also help to contain the plasma. Lastly, electrostatic acceleration was found to create thrust by extracting and accelerating the positively charged ion particles.

Ion propulsion was reviewed in detail in order to begin a discussion of the design conceptualisation of the RF ion thruster. A number of conceptual designs are examined in this chapter to determine the optimal concept for reaching the thesis goals. Thereafter, the preliminary design of an RF ion thruster is discussed. Finally, the complete RF ion thruster is presented in detail, where the design of the ion optics, in order to achieve thrust, is described.

3.1 Conceptual Design

The design of a RF based ion thruster was the primary aim of this thesis because the lifespan of the thruster can be increased in the absence of electrodes that erode over time. Several design concepts were explored to ionise the propellant within the parameters of minimal manufacturing time and costs. Due to availability and cost effectiveness of microwave ovens, the 2.45 GHz magnetron from the oven was used for ionisation purposes.

3.1.1 Tokamak Plasma Containment (*Concept 1*)

The high power usage involved in the ionisation process of the propellant is the main disadvantage of electric thrusters. Additionally, the extraction of all the positive charge particles increase the power usage. In order to address this limitation, the positively charged particles is contained instead of ejected. Neutral particles are ionised by the extraction of a small amount of charged particles which collide with the neutral particles. This concept is largely inspired from Rostoker's work [26] on toroidal acceleration of heavy ions.

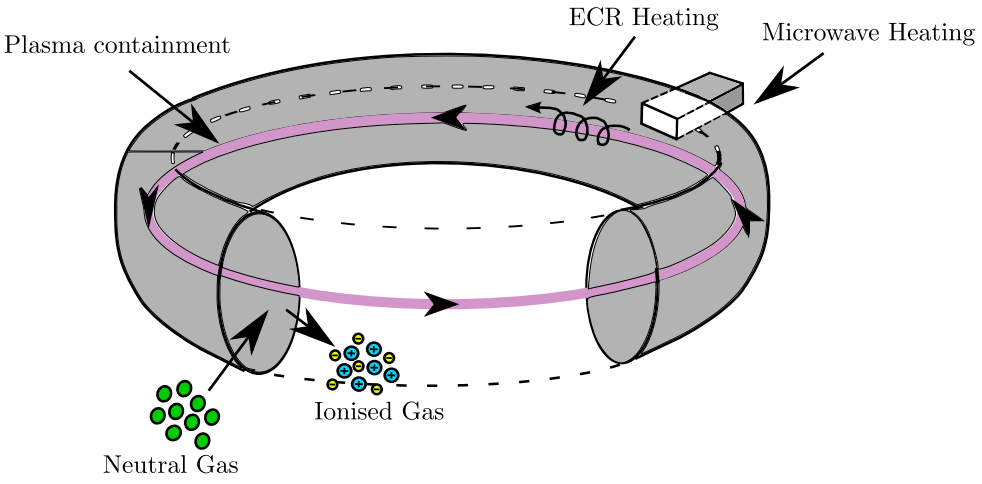

Figure 3.1: Plasma containment with tokamak concept.

Similar to the Tokamak concept (see Figure 3.1 above), a magnetic field is used to confine a plasma in the shape of a torus. However, instead of keeping all the plasma contained inside the toroid, some of the charged particles are 'extracted' to collide with neutral particles, in order to transfer their energy to the neutral particles. The neutral particles are ionised through the process of electron bombardment (discussed in 2.2).

Although the Tokamak concept has some advantages, the plasma confinement poses potential difficulties. The amount of energy that is needed to ensure that the plasma does not collide with the surface of the toroid is very high for the electromagnets. In addition, Rostoker [26] found that it would be necessary to extract the plasma beam simultaneously, at various locations, and guide the ion beams to a single target for sufficient ionisation. This adds to the complexity of the thruster design.

3.1.2 WR340 Plasma Applicator (*Concept 2*)

Gower [27] largely inspired the second concept, where a high power microwave plasma beam applicator was developed. The concept entails feeding 2.45 GHz electromagnetic fields via a WR340 waveguide into an applicator containing a quartz tube. The neutral gas is injected into the tube for ionisation. A tuning plunger, as shown in Figure 3.2 below, is used to tune the applicator.

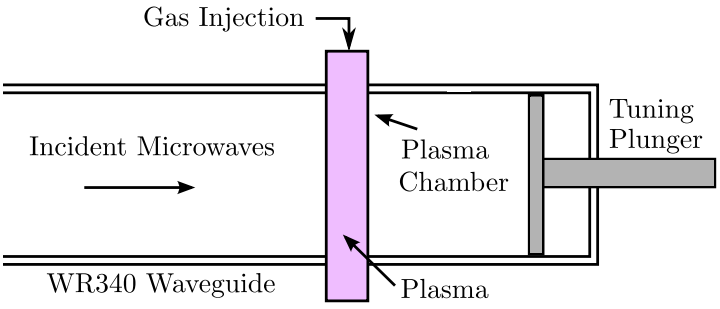

Figure 3.2: Waveguide ionisation concept.

The properties of plasma change over time, as mentioned in section 2.2.4.1, which complicates the load matching of the applicator. The concept above includes a tuning plunger to alleviate this difficulty. The tuning plunger ensures a standing wave pattern with a maximum electrical field centred in the plasma confinement chamber. Once the plasma has been initiated, the plunger can be adjusted to ensure minimum reflected power. However, Gower [27] found that plasma ignition can only be achieved with the insertion of a tungsten wire. Thereby, an electron source from the resultant spark is created which results in plasma 'ignition'.

The major drawback to this design is that the need of a plunger to 'ignite' the plasma results in a reduction in lifespan for the thruster. The plunger will erode over time decreasing the lifespan of the thruster which is commonplace for electrode base thrusters. Furthermore, the cooling of the quartz tube will be very difficult. Water is a very good receptor of microwave energy. This means that general water cooling is not a viable option because the water will absorb all/most of the ionisation energy. Thus an insufficient electrical field strength results, that will not be able to sustain the plasma.

3.1.3 Circular TM_{010} cavity (*Concept 3*)

The final concept, based on *Concept 2*, involves a cavity that generates a maximum electrical field at the plasma region. Instead of using a WR340 waveguide with a quartz tube and tuning plunger, the concept consists of a single mode TM_{010} cylindrical cavity, coupled with a WR340 waveguide, with magnetic flux linkage (see section 2.2.4.5). This is illustrated in Figure 3.3 below. The single mode TM_{010} cavity, as discussed in section (2.2.4.3), ensures a high electrical field concentration in the cavity's centre which aids plasma ionisation (see Figure 2.3). In addition, the cylindrical cavity makes the application of a high external magnetic field (i.e. electromagnet) easier which facilitates the ECR process and plasma containment.

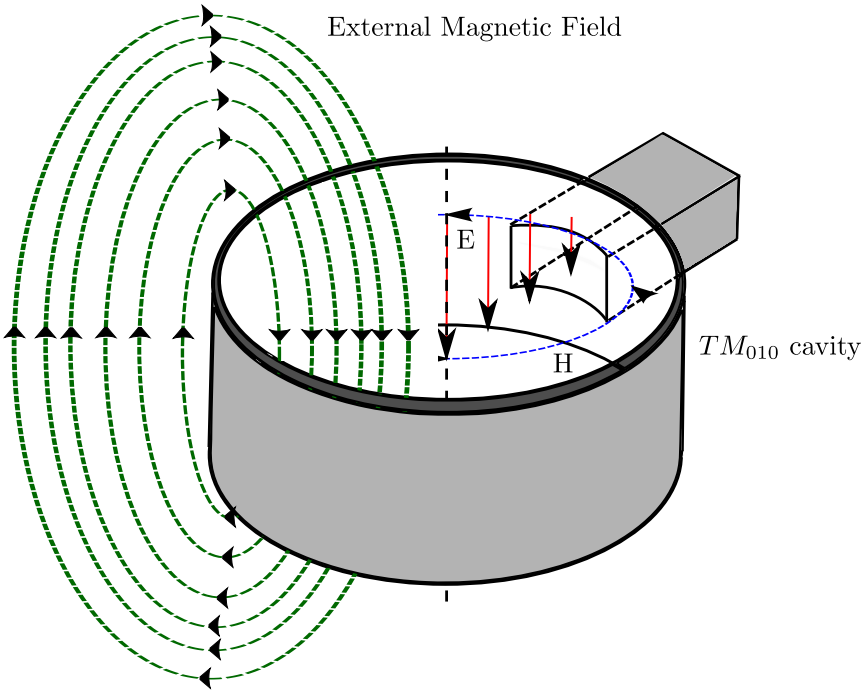

Figure 3.3: TM_{010} cavity with an external magnetic field coupled with a WR340 waveguide.

In comparison to the other two concepts, the concept has a few advantages. For example, there is no need for a quartz tube for plasma confinement, as an external magnetic field achieves the plasma confinement. In addition, there is no need for a plunger to achieve plasma ignition. The external magnetic field will facilitate the ECR process to ensure efficient ionisation of the propellant.

3.1.4 Concept Evaluation

The various strengths and weaknesses of each concept are summarised in Table 3.1 to allow a decision to be made as to which is the best ionisation concept for this thesis.

Table 3.1: Comparison of strength and weaknesses of each concept.

Conceptual design	Strengths	Weaknesses
Concept 1	Plasma containment	High power usage Complex design High manufacturing cost
Concept 2	Load matching Simple design Low Manufacturing cost	Limited lifespan Cooling required
Concept 3	Extended lifespan Efficient heating (ECR) No cooling required Simple design	Difficult load matching

By taking into account the equipment available from Stellenbosch University and Table 3.1, *Concept 3* was chosen as the concept of choice. The TM_{010} cavity has difficulty in maintaining a 'single mode' of operation as the plasma's properties change over time. However, the TM_{010} cavity can be designed from the beginning for load matching to start the ionisation process. After the start of ionisation, the 'mode' of operation for the cavity is not crucial, provided that the plasma is sustained.

3.2 Preliminary Design

The ion thruster's design was largely inspired by Ganguli *et al.* [28] and Kuninaka *et al.* [12]. The thruster operates by injecting an inert gas [1] into the centre of a cylindrical TM_{010} cavity, known as the discharge chamber. The cavity produces a maximum electrical field in the centre of the chamber which excites and ionises the neutral gas. An external magnetic field is placed around the outer edge of the cavity to contain the plasma and assist in producing a high plasma density through the ECR process. The positively charged ions move through the length of the chamber until the grid system is reached, where the ions are extracted and accelerated.

Figure 3.4 shows a representation of the thruster. The RF ion thruster can be divided into two main sections: 1) ionisation via the TM_{010} cavity, and 2) the extraction/acceleration

[1] Xenon gas is typically used in an ion thruster. However, in order to keep costs to a minimum Argon gas was chosen.

by means of the ion optics. The following sub-sections describes the design of these two sections.

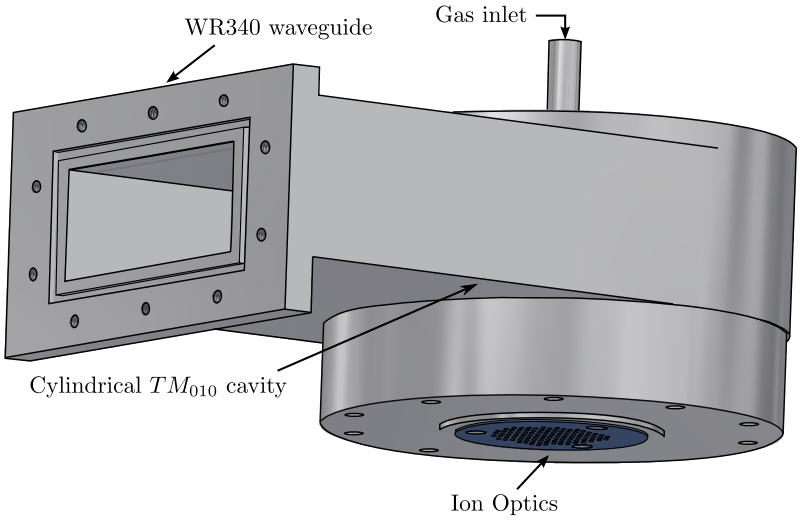

Figure 3.4: Preliminary RF ion thruster design.

3.2.1 Cavity Design

3.2.1.1 Dimensions of Cylindrical Cavity

The TM_{010} cavity was designed with a 2.45 GHz operating frequency based on the accessibility of microwave ovens. The cavity dimensions were obtained from the Bessel function and resonant frequency (Equation 2.2.35) with internal radius:

$$a = \frac{X_{01}}{f_0(2\pi)\sqrt{\mu_0\epsilon_0}} = \frac{2.4049}{2.45 \times 10^9(2\pi)\sqrt{\mu_0\epsilon_0}} = 0.4684\ [m]. \tag{3.2.1}$$

The above radius is calculated for 2.45 GHz resonance of an empty cavity. The radius must be reduced, in order to maintain the same resonant frequency when a dielectric load is added to the given cavity. However, prior to ignition, the gas injected into the system has very weak interactions with the electromagnetic fields inside the cavity. Therefore, the dimensions of the cavity were designed for an empty cavity. This ensures that the cavity resonates at 2.45 GHz, with a maximum electrical field in the centre of the cavity, to successfully ionise the neutral Argon gas.

Although the resonant frequency is independent of the cavity height, h, in a TM_{010} cavity, the mode of operation must be considered. The dominant TM_{010} mode needs to be ensured, which means the ratio of the height and radius, h/a, must be smaller than 2.03 [16]. Thus the height of the cavity was chosen as $h \approx 0.93\ [m]$.

3.2.1.2 Coupling Method for TM_{010} mode

The cylindrical TM_{010} cavity was coupled with the magnetic flux linkage method to a rectangular TE_{10} waveguide. This method can accommodate a dual directional coupler to observe the transmitted and reflected power. A circulator is used to protect the magnetron from overheating, as was discussed in section 2.2.4.5. The cut-off frequency for the TE_{10} waveguide can be calculated from Equation 2.2.38 with $a = 0.8636$ $[m]$ and $b = 0.4318$ $[m]$ obtained from literature:

$$(f_c)_{min} = \sqrt{(\frac{m\pi}{a})^2 + (\frac{n\pi}{b})^2} \approx 1.7 \ [GHz].$$

The decision was made not to use an iris with the waveguide coupling. An iris will ensure a very high Q value at the specific frequency f_0, as shown below in Figure 3.5, but with a small bandwidth. The small bandwidth would mean that impedance matching should change constantly (iris width should change) as the load's properties change. The change in load properties will affect the resonant frequency, which will result in microwave energy being reflected if the iris coupling is not matched to the impedance of the cavity. This is a challenge as the non-linear nature of plasma means that the entire process would need matching throughout the sustainment of the plasma. Without an iris, the Q-value is much lower but the bandwidth of the system is greater. Thus, less microwave energy would reflect back towards the circulator with a change in the plasma's properties.

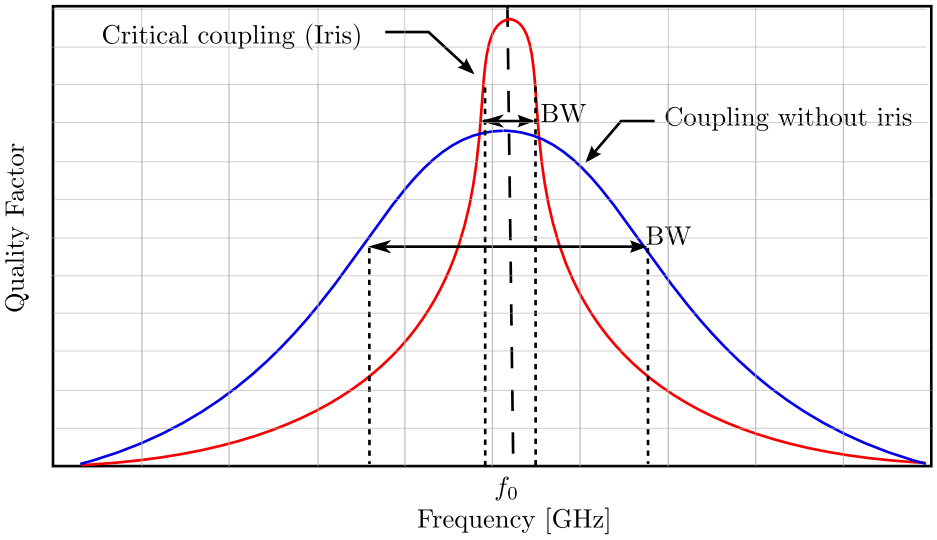

Figure 3.5: Effect of iris coupling.

3.2.1.3 CST Simulation of TM_{010} Cavity

Although the cavity is designed for a TM_{010} resonant mode, it is possible that other modes are being excited inside the cylindrical cavity. This could be the result of disfigurements on the cavity, such as manufacturing inaccuracies. The initial objective of the project was to extract and accelerate the ions with an electromagnetic acceleration process, as discussed in 2.3, and so the cavity was designed with this objective in mind. As a result, the cavity was designed with a 'cone' shape at the bottom to ensure minimum RF leakage. These cone dimensions can also affect the TM_{010} resonant mode. A simulation of the proposed cavity was performed with CST Microwave Studio software in order to analyse the effects of these components.

The simulation was used to analyse the electromagnetic fields inside the cavity. The computation time of the simulation was decreased by the simplification of the geometry used, as presented below in Figure 3.6. The simplification of the simulation was assisted by making the assumption that the gas flow and heat transfer would not affect the resonant electromagnetic fields inside the cavity. The gas, when ionised, transforms into a conductive plasma, with conductivity ranging between $\sigma = 200 - 10,000\ S/m$ (see section 2.2.4.1). This plasma 'load' will impact the electromagnetic fields inside the cavity as well as the TM_{010} resonant mode. Nevertheless, the purpose of the cavity is to resonate at 2.45 GHz in a TM_{010} mode prior to ionisation of the propellant. Once ionisation is achieved, the electromagnetic field distribution is no longer of interest. Therefore, the simulation was conducted with an empty cavity.

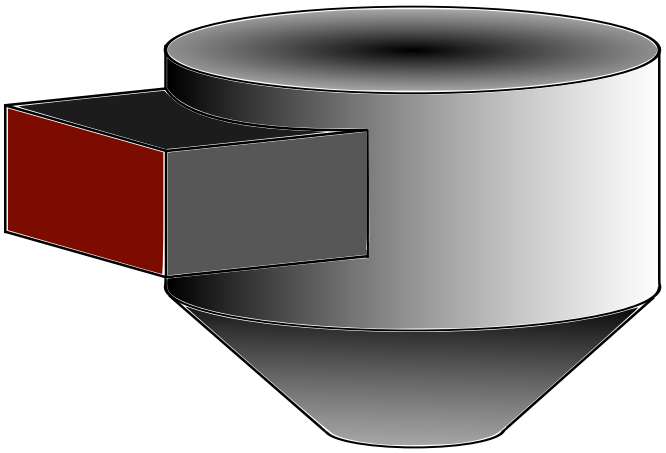

Figure 3.6: Simplified cavity for CST simulation.

The exact dimensions of the cavity were obtained by the simulation of the EM field. It was found that the internal radius of the cavity should be $a = 48\ mm$ in order to ensure a TM_{010} resonant mode. This new radius dimension in the simulation verified that the cavity's field distribution (see Figure 3.7) corresponds to that of the TM_{010} cavity, as

illustrated in Figure 2.3, with a maximum electrical field intensity in the centre of the cavity.

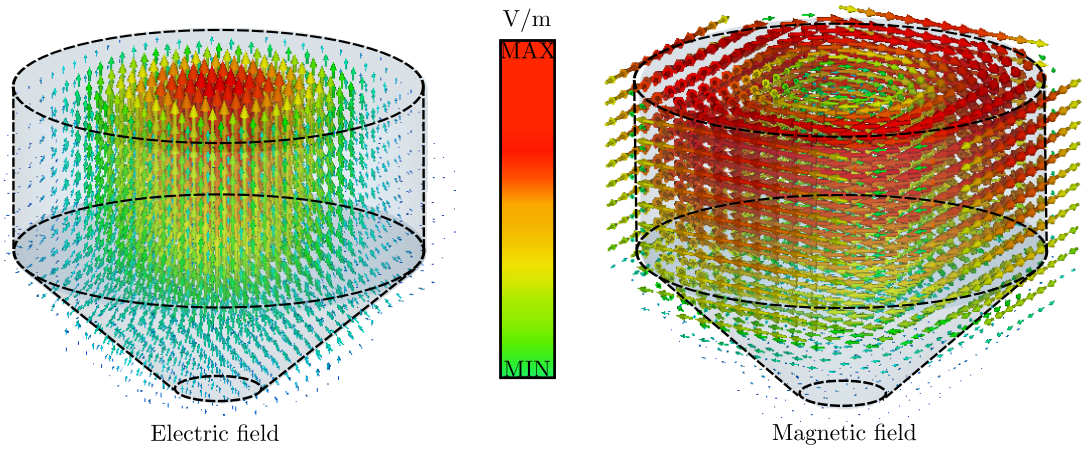

Figure 3.7: CST Simulation of the electric and magnetic field distributions for the designed TM_{010} resonant cavity.

The return loss (S_{11}) was simulated to determine if the cavity resonates at 2.45 GHz. Figure 3.8 verifies that the cavity resonates at the desired frequency with a return loss of approximatively -20 dB at 2.45 GHz. The return loss does not have a sharp peak at 2.45 GHz. This is as a result of the cavity coupling with a waveguide, without an iris, as was explained in section 3.2.1.2. Unfortunately it was not possible to simulate the effect of the plasma on the cavity. However, as mentioned earlier, this is not important for the purpose of the design of the cavity. The 'mode' and frequency of operation is not as critical post ionisation, as long as the plasma is sustained.

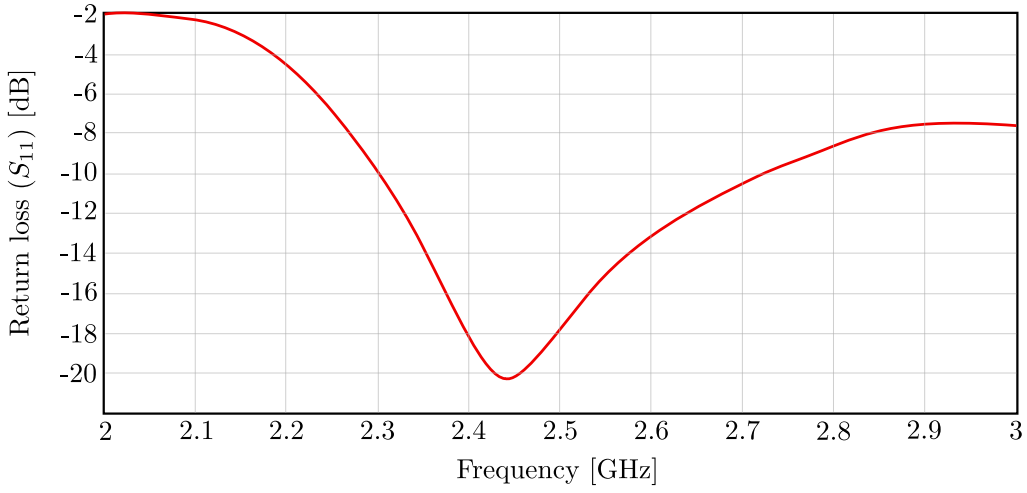

Figure 3.8: Simulated reflection coefficient of preliminary cylindrical cavity.

3.2.2 Ion Optics Design

The original objective of the project was to accelerate the charge particles by means of electromagnetic acceleration. Unfortunately, due to the time limit, this was not possible. Therefore, the thruster was adapted for the method of electrostatic-acceleration, via electrically biased multi-aperture grids. The decision to introduce a three grid system was inspired by Coletti *et al.* [29] and Miyoshi *et al.* [30]. The design consists of a three grid system where a positive potential screen grid (the first grid) is placed adjacent to the discharge plasma and is followed by a negative charge acceleration grid (the second grid). The final grid, called the "deceleration grid", is placed downstream of the acceleration grid and is kept at a ground potential. Coletti *et al.* [29] found that the deceleration grid shields the acceleration grid from ion bombardment. The charged ions that accelerated through the acceleration grid, tends to flow back into the acceleration grid. This is as a result of the negative voltage of the acceleration grid, which attracts the positively charged ions. The third grid, biased at ground potential, shields the acceleration grid from the ions flowing back into system. In addition, the biased ground voltage results in low energy collision of ions against the deceleration grid. Therefore, the thruster's lifespan is extended and less plume material is generated and deposited on the spacecraft. An illustration of the three grid system is shown in Figure 3.9.

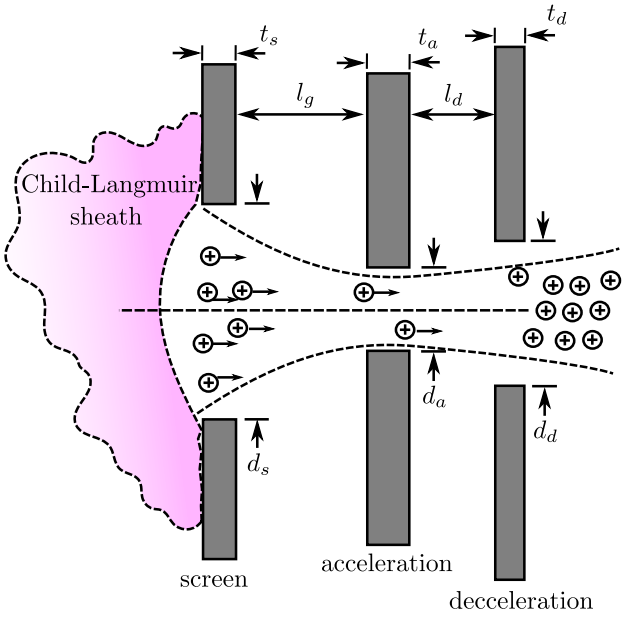

Figure 3.9: Illustration of the three grid system to extract and accelerate ions (adapted from [7]).

The aperture size of the screen grid was chosen to allow the establishment of a Child-Langmuir sheath around each screen hole for effective extraction and acceleration. The grid gap distance was chosen to ensure maximum perveance at the Child Langmuir limit.

The perveance is known as the amount of current that an ion accelerator can extract and focus into a beam for a given voltage (space charge limit). The perveance is given as Equation 3.2.2 [7]

$$P_{max} = \frac{\pi\epsilon_0}{9}\sqrt{\frac{2q}{M}}\left(\frac{D^2}{l_g^2}\right) \ [A/V^{3/2}], \tag{3.2.2}$$

where l_g is the effective grid gap and D (d_s in Figure 3.9) is the plasma beam diameter. Higher perveance can be achieved by ensuring that the grid gap, l_g, is smaller than the aperture diameter D.

Grid Dimensions

Due to the complexity of grid thrusters and the necessity of required simulation software to obtain optimal dimensions, the physical dimensions of the grid-apertures and grid-spacing were based on values identified in literature that yielded optimal performance. Taking into consideration the design of Colleti *et al.* [29] and the theory of a Child Lanmguir sheath, the screen grid was designed with apertures of $d_s = 2$ $[mm]$. The diameter of the screen grid holes are typically chosen to be larger than those of the acceleration grid. This is done, in order to retain a non-ionised propellant, and ensure a focused ion beam. The acceleration grid apertures were designed to retain a non-ionised propellant and focus the ion beam with apertures of $d_a = 1.6$ $[mm]$. The distance between the grids needs to be as small as possible to ensure a maximum perveance. In taking voltage breakdown and grid lifespan into consideration, the distance between the screen and acceleration grid was chosen to be $l_g = 0.5$ $[mm]$. The gap distance between the acceleration grid and deceleration grid was selected by using the model developed by Holmes and Thompson [31]. The overall design dimensions of the ion optics are reported in Table 3.2.

Table 3.2: Ion Optics geometry for designed three-grid system (Figure 3.9).

Grid Type	Aperture diameter [mm]	Grid thickness [mm]	Gap distance
Screen	$d_s = 2$	$t_s = 0.5$	
Acceleration	$d_a = 1.6$	$t_a = 1.6$	$l_g = 0.5$
Deceleration	$d_d = 1.6$	$t_d = 1$	$l_d = 0.8$

Grid Potentials

The voltage potential between the grids plays a vital role in the success of the ion optics. After plasma ignition, stable plasma sheaths are formed around each aperture of the screen grid. Ions will reach a sheath with Bohm velocity [32], before being accelerated through the ion optics to form a focused ion beam. The desired Child Langmuir sheath (shown in Figure 3.9) will move further into the screen grid apertures (shown in Figure 3.10) when the voltage potential is too high. The desired concave shape sheath will be transformed. As a result, ions will impinge on the acceleration grid, which will seriously compromise the thruster performances and lifespan [33].

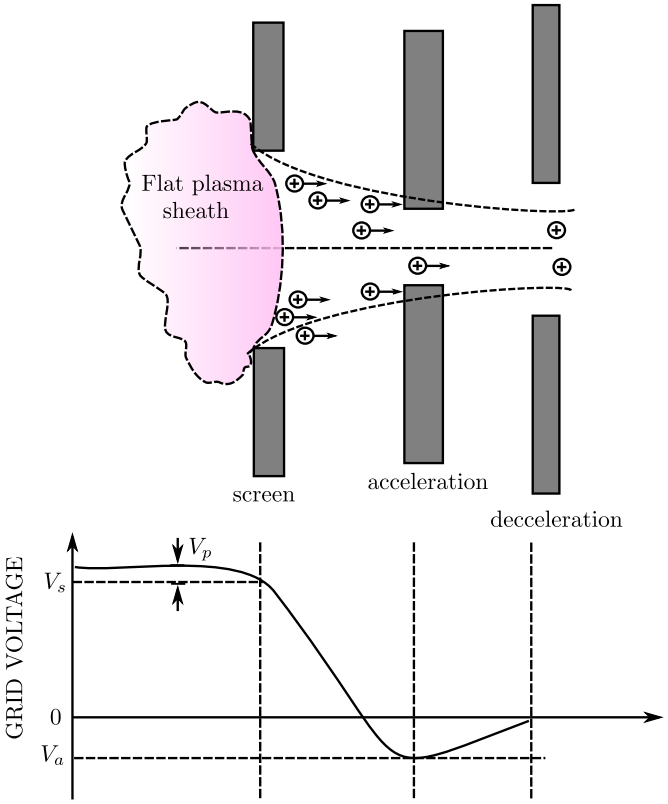

Figure 3.10: Affect of flat sheath on ion optics performance.

Previous literature [30; 29] found that voltages between 1000 V and 1500 V were typically used for the screen grid, and that the acceleration grid was normally biased with a voltage of -250 V. The performance of the thruster is affected by a greater negative voltage which attracts the positive charge ions backwards, against the plasma flow, as they pass through the acceleration apertures. Therefore, the initial voltage chosen for the ion optics was $V_s = 1200$ V for the screen grid and $V_a = -250$ V for the acceleration grid. The deceleration grid is kept at ground potential in order to minimise the effect of ions back-flowing into the acceleration grid.

3.3 Final Design

3.3.1 Cavity

The cavity was divided into three sections to facilitate manufacturing as shown in Figure 3.11. The 'top' and 'middle' section was designed to be welded together. The 'bottom' section was fastened with M6 countersunk bolts. The gas lid and the 'bottom' section was sealed with Viton® O-rings[2] to achieve a vacuum inside the cavity. Viton® O-rings were chosen due to their high temperature resistance, which will accommodate the rising temperature of the cavity during operation. A complete detailed design of the drawings can be found in Appendix B. The final cavity consists of aluminium and is shown by Figure 3.12.

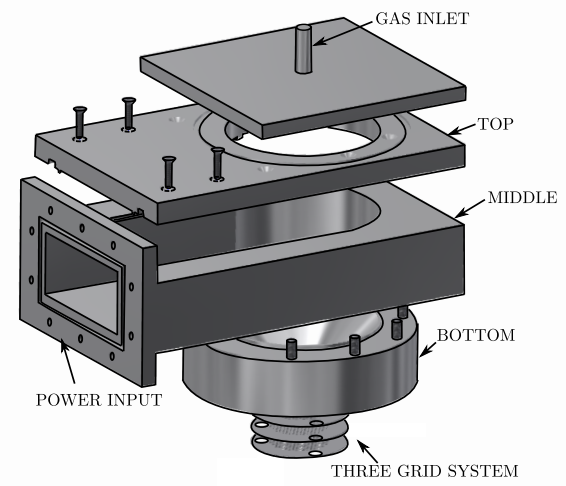

Figure 3.11: Exploded representation of final cavity.

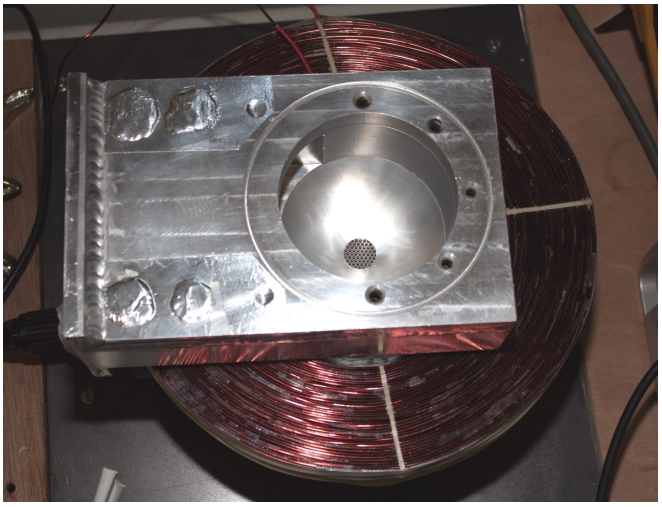

Figure 3.12: Final cavity design.

[2]Viton®O-rings are widely used in chemical, aerospace and industrial applications because of their excellent chemical and temperature resistant characteristics.

Verifying Operation of Cavity

The cavity was analysed using a Vector Network Analyser (VNA) to confirm that the final manufactured cavity operates in the TM_{010} resonant mode at 2.45 GHz. An experiment was done with the VNA to verify that the cavity produces a maximum electrical field distribution in the centre of the cavity. This was achieved by measuring the transmitted S_{21} power from the centre of the cavity to the side of the cavity, as shown in Figure 3.13. A separate gas lid with, a circular pattern of 5 mm arranged from the centre of the cavity to the sides, was designed to achieve the measurement.

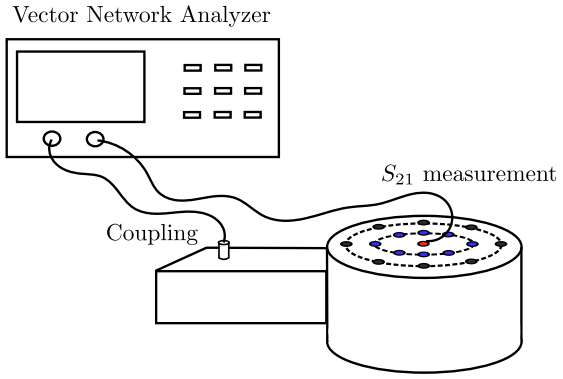

Figure 3.13: Cavity measurement setup.

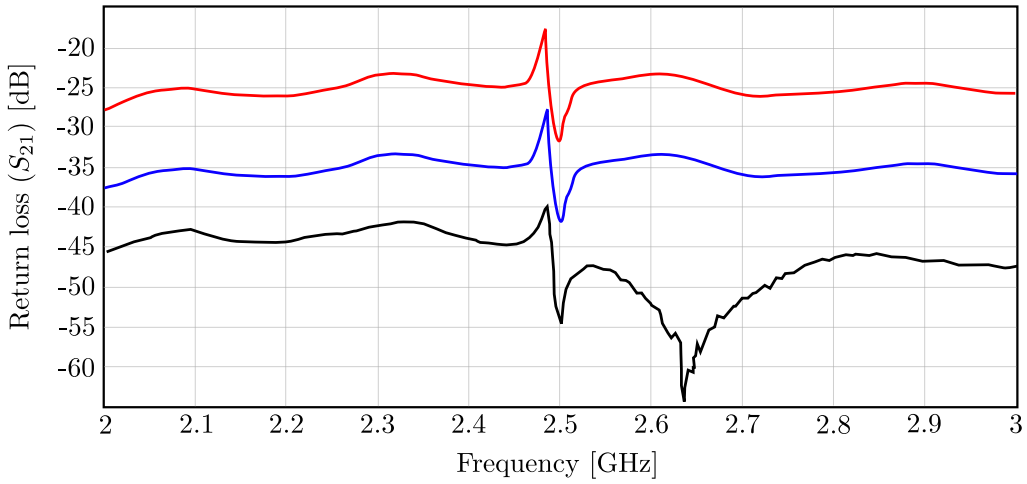

Figure 3.14: Verify electrical field distribution of manufactured cavity.

The experiment (Figure 3.14) verified a maximum electrical field distribution in the cavity centre (red graph in Figure 3.14). The magnitude was observed to decrease when moving to the sides of the cavity (blue and black graph in Figure 3.14). Therefore, it can be concluded that the cavity corresponds to the CST simulation in section 3.2.1.3 and the theory of a TM_{010} cylindrical cavity. Although the cavity's field distribution is

as desired, the VNA showed that the cavity resonates at a frequency slightly higher than 2.45 GHz. This could be the result of the impedance of the probe (input energy from VNA) and waveguide coupling that does not perfectly match the impedance of the cavity. Manufacturing inaccuracies can also contribute to the shift in resonant frequency.

3.3.2 Ion Optics

Ion optics are usually constructed out of molybdenum because the material extends the lifespan of the thruster by resisting plasma erosion. However, it was decided to manufacture the ion optics out of stainless steel due to the cost and lack of availability of molybdenum. As a result, the grids were designed in such a way that they can easily be replaced if extensive erosion occurs. All three grids were designed with apertures in a hexagonal pattern (see Figure 3.15). During manufacturing, the accuracy of the apertures was improved with the use of laser cutting.

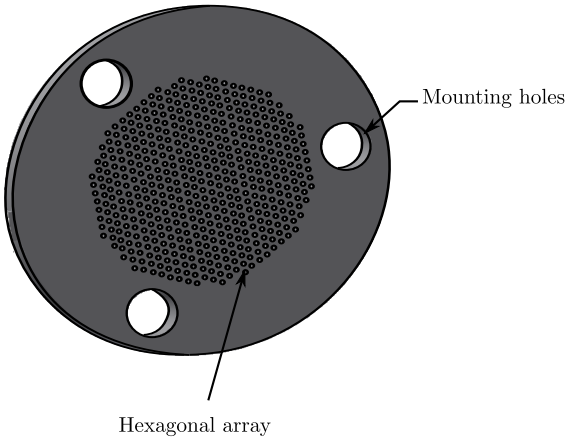

Figure 3.15: Preliminary design of ion optics.

Misalignment of the apertures is one of the most common problems in ion optics. Misalignment can be caused by mechanical or thermal stress as well as improper installation. As a result of this, ions impinge on the grids, causing the lifespan of the grids to be shortened. In addition, the extracted ion beam angle is affected, which reduces the thrust. Nothing could be altered to reduce the effects of thermal stress, however, the possibility of an improper installation was minimised. The grids were designed in such a way that the corresponding centre of each aperture of each grid was aligned during installation. Mica washers were used to achieve the grid spacing and three mounting holes were used for mounting the grids. The stability of Mica under extreme temperatures, resulted in the selection of this material to tolerate the temperatures of the grids during operation. The final grids were manufactured with an area of 28 cm^2, as shown by Figure 3.16.

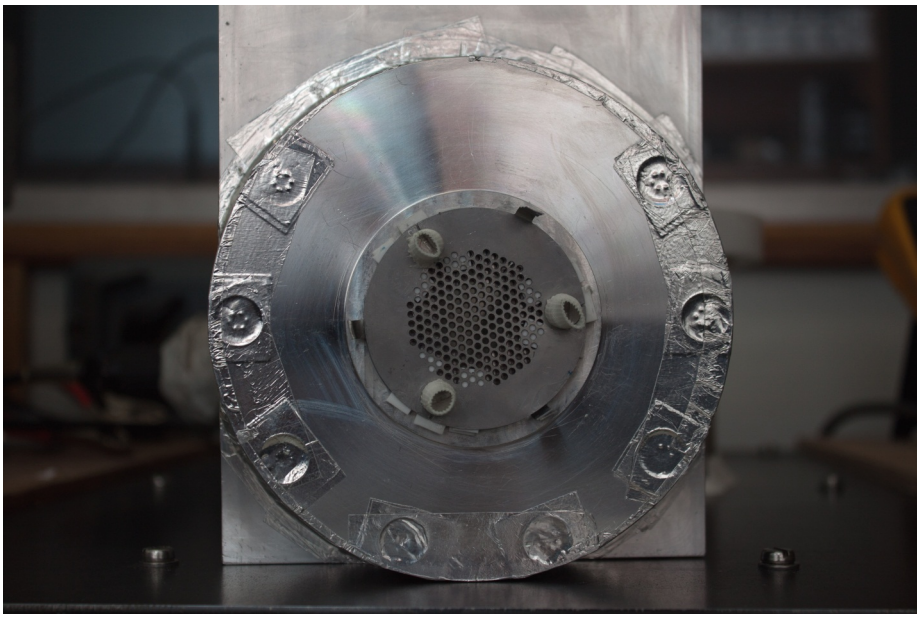

Figure 3.16: Final ion optics design.

3.4 Summary

In this chapter, the microwave-based ion thruster was designed and manufactured. A study was conducted with three conceptual designs, which entailed the use of a 2.45 GHz magnetron from a domestic microwave oven. A cylindrical TM_{010} resonant cavity coupled with a rectangular TE_{10} waveguide was found to be the most effective design for the purposes of this thesis. A simulation was performed using CST Microwave Studio software in order to analyse the electromagnetic fields inside the cavity. The cavity was found to produce a maximum electrical field distribution at the centre of the cavity which assists in the ionisation of the propellant. Finally, the ion optics were designed for the purpose of extracting and accelerating positive charge ions. The design entailed a three grid system where: a screen grid was biased at 1200 V; an acceleration grid was biased at -250 V; and a deceleration grid was biased at ground potential. The third grid was introduced in order to prevent ions from flowing back into the acceleration grid.

Chapter 4

Theoretical Predictions

This chapter presents the theory to predict the performance of the thruster designed in the previous chapter. Thruster performance is typically described by thrust and specific impulse. Therefore, the two main sections of this theoretical discussion will centre around thrust and specific impulse performance requirements. In order to calculate an accurate performance prediction, some corrections such as ion beam divergence and multiple charge species are introduced.

4.1 Thrust Prediction

The maximum theoretical current density for the thruster can be obtained from Equation 2.3.2 and Equation 2.3.3, assuming a Child Langmuir sheath is produced around each aperture. The values from sections 3.2.2 show that with $V_T = 1450\ V$ and $l_e = 0.1414\ cm$, the maximum ion current density can be calculated as,

$$\begin{aligned} J_{max} &= \frac{4\epsilon_0}{9}\sqrt{\frac{2e}{M}}\frac{V_T^{3/2}}{l_e^2} \\ &= 8.61242 \times 10^{-9}\frac{V_T^{3/2}}{l_e^2} \\ &= 23,78\ mA/cm^2. \end{aligned}$$

Thus the maximum ion beam current that can be obtained for the grids, with a grid aperture area of 3.14159 cm^2 (as designed in section 3.3.2), is $I_b = 74.70\ mA$. Assuming average beam voltage $V_b = 0.9(V_s + |V_a|) \approx 1305V$, the maximum thrust for this beam current yields,

$$T = \sqrt{\frac{2M}{q}} I_b \sqrt{V_b} = 2.47\ mN.$$

This calculated prediction is based on an unidirectional single ionised beam of ions starting at rest. However, in order to achieve this unidirectional beam, the operation parameters of the thruster needs to be perfect. In practice, thrust is decreased by plume angles, multiple charge ions and incomplete ionisation. Therefore, a more realistic prediction is obtained by applying two corrections. The first correction is for the beam divergence in a thruster, with a constant ion density, and is given as [7],

$$F_t = cos\Theta, \tag{4.1.1}$$

where Θ is the average half-angle divergence of the beam. Coletti [29] found that, for a three grid system with more or less the same parameters as this thesis, the divergence was about 10 degrees.

The second correction is for the presence of multiple charged ion species. If the ion beam contains singularly charged ions (I^+), as well as double charged ions (I^{++}), the total thrust T_m will be the sum of the thrust for each species [7]:

$$T_m = I^+\sqrt{\frac{2MV_b}{q}} + I^{++}\sqrt{\frac{2MV_b}{q}} = I^+\sqrt{\frac{2MV_b}{q}}\left(1 + \frac{1}{\sqrt{2}}\frac{I^{++}}{I^+}\right). \tag{4.1.2}$$

A similar correction can be applied for higher charged ions, although they are not typically present in ion thrusters. The thrust correction factor α for double charge ions is presented as,

$$\alpha = \frac{1 + 0.707\frac{I^{++}}{I^+}}{1 + \frac{I^{++}}{I^+}}. \tag{4.1.3}$$

The total thrust correction is the product of the two corrections discussed and is given as $\gamma = \alpha F_t$. The new prediction thrust is then given by

$$T = \gamma\sqrt{\frac{2M}{q}} I_b\sqrt{V_b}. \tag{4.1.4}$$

The predicted thrust for the thruster is calculated from Equation 4.1.4 as $T = 2.362\ mN$ for a divergence of 10 -degrees and a 10% doubles-to-singles charge ratio.

4.2 Specific Impulse (I_{sp})

The Specific Impulse (I_{sp}) is a measure of thrust efficiency. This measurement is defined as the ratio of the thrust to the propellant flow rate. The specific impulse for a constant thrust and propellant flow rate is given as [7]

$$I_{sp} = \frac{T}{\dot{m}_p g}, \tag{4.2.1}$$

where $\dot{m}_p$ is the propellant mass flow rate and g the acceleration of gravity at 9.807 m/s^2. The propellant mass flow rate $\dot{m}_p$ can be represented by

$$\dot{m}_p = QM, \tag{4.2.2}$$

where Q is the propellant particle flow rate (in particles/s) and M is the particle mass.

In electric thrusters, the specific impulse is defined in terms of the exhaust velocity as

$$I_{sp} = \frac{v_i}{g}\eta_m, \tag{4.2.3}$$

where v_i is the exhaust velocity of the ions. The efficiency of utilisation for the thruster for ionised versus unionised propellant is represented by η_m, and can be defined for a single charged ion as

$$\eta_m = \frac{\dot{m}_i}{\dot{m}_p} = \frac{I_b}{e}\frac{M}{\dot{m}_p}. \tag{4.2.4}$$

In order to calculate the predicted specific impulse, the exhaust velocity of Equation 4.2.3 can be substituted with Equation 2.1.3. Furthermore, the thrust corrections obtained in section 4.1, can be included to express the I_{sp} as

$$I_{sp} = \frac{\gamma\eta_m}{g}\sqrt{\frac{2qV_b}{M}} \text{ [7].} \tag{4.2.5}$$

The predicted specific impulse is calculated from Equation 4.2.5 as $I_{sp} = 6178$ *seconds* for a correction of $\gamma = 0.958$ and $\eta_m = 0.8$. It is shown in Equation 4.2.5, that to achieve a high specific impulse, it is necessary to operate at a high utilisation efficiency, η_m, and a high acceleration voltage , V_b.

4.3 Improving Performance

According to Equation 2.3.2 and Equation 2.3.4, the extracted current density and thrust can be augmented by increasing the electric field $E = \frac{V_T}{l_e}$ between the grids. Unfortunately, variation of this parameter is limited as an increase of the electric field over a threshold level will cause arcing between the grids ($E > E_{breakdown}$). Another limitation to the achievable current density and thrust is the perveance P_{max} (see Equation 3.2.2) which is related to the space charge region. The 'grid-system' can only extract a certain amount of current for a given voltage before the ions collide against the acceleration grid. In addition, the acceleration grid apertures are normally smaller than the screen grid apertures, which results in a higher probability of ions colliding against the acceleration grid. Thus the working perveance commonly used in ion thrusters is no higher than 50% of P_{max}.

One parameter that can increase the thrust of ion thrusters is the area of the ion optics. As the grid area is increased, the number of apertures can be increased. This results in high beam currents and an increase in thrust. However, there is a limitation to the size of the grids. The ion density needs to be high enough so that sheaths can form across the total area of the grids.

4.4 Summary

The predicted performance of the thruster, designed in Chapter 3, were studied. The maximum thrust achievable was found to be $T = 2.362\ mN$ when the affect of beam divergence and multiple charge ion species were taken into account. The maximum specific impulse predicted for the thruster was calculated as $I_{sp} = 6178\ seconds$. In addition, methods to improve the performance of the thruster were studied. An increase in the grid area was found to be a parameter that can increase the performance, as long as the ion density is high enough to produce a Child Langmuir sheath across the total grid area.

Chapter 5

Experimental Work

The theoretical predictions regarding the RF ion thruster's performance were discussed in the previous section. An experimental setup for the thruster was performed in order to verify these predictions and the operation of the RF ion thruster. The experimental design, setup and test procedures are explained in this chapter. A vacuum system consisting of a roughing and diffusion pump, that could achieve pressures of up to $10^{-6}\ Torr$, was designed to perform the experimental work. Microwave power was generated using a 600 W 2.45 GHz magnetron launched with a WR340 launcher. A circulator was used to prevent magnetron heating and failure, by preventing reflecting power coupling to the magnetron antenna. Also, a dual direction coupler was introduced into the system to determine the forward and reflected power. Figure 5.1 demonstrates the experimental arrangement. A three stub tuner is usually added to the system to aid impedance matching between the magnetron, waveguide and cavity. However, a three stub tuner was not available for the experimental work.

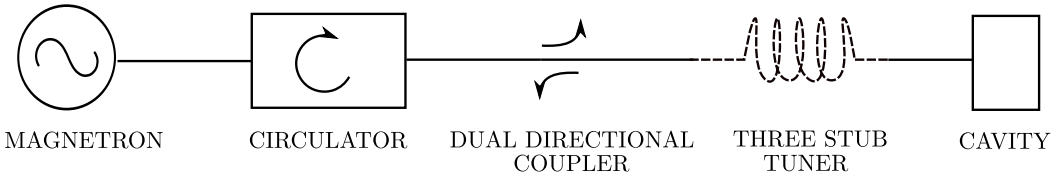

Figure 5.1: Schematic diagram of experimental arrangement.

5.1 Vacuum System

A vacuum chamber was required which could achieve pressures of at least 10^{-5} Torr [1] to test the RF ion thruster. This operating pressure was achieved using a two stage vacuum system designed with a *Two stage Edward 8* rotary pump and an oil vapour diffusion pump. The rotary pump was used in the first stage to achieve a pressure of approximately 10^{-3} Torr. Thereafter, the oil vapour diffusion pump was used to reduce the pressure to approximately 10^{-6} Torr. A simple diagram of the two stage system is shown in Figure 5.2. Solenoid valves aid switching between the two stages in the vacuum system. A detailed description of the vacuum system can be obtained in Appendix A.

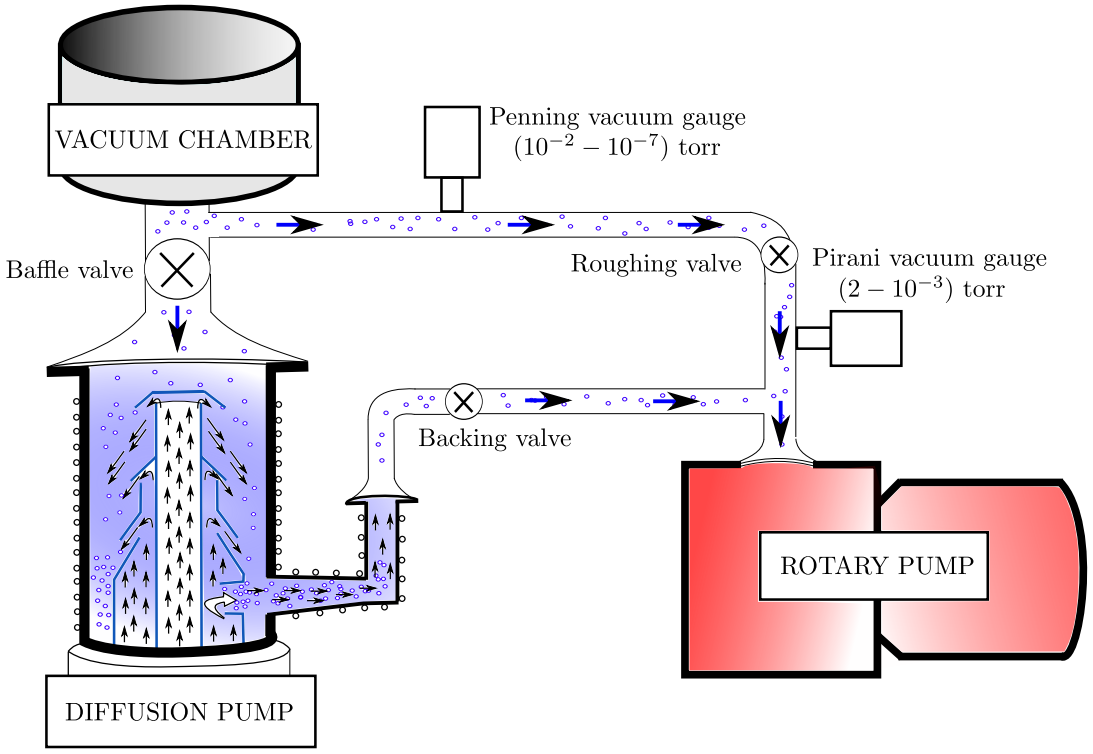

Figure 5.2: Two stage vacuum system.

The vacuum chamber was designed to accommodate the ion thruster and was manufactured out of aluminium. A window was introduced to one side of the chamber to allow observation of the extracted ion beam, as shown in Figure 5.3. The window also served as a 'port' to supply the grids inside the vacuum chamber with the high voltages needed for the operation of the ion optics. In addition, a *Penningvac* vacuum gauge was added to the vacuum chamber to determine the operating pressure. A Teflon divider was implemented

[1] Most literature operating pressure is between 10^{-3} and 10^{-5} Torr [34; 35; 28].

between the vacuum chamber and the cavity. This divider protected the vacuum system from the heat and high voltages of the cavity, during operation.

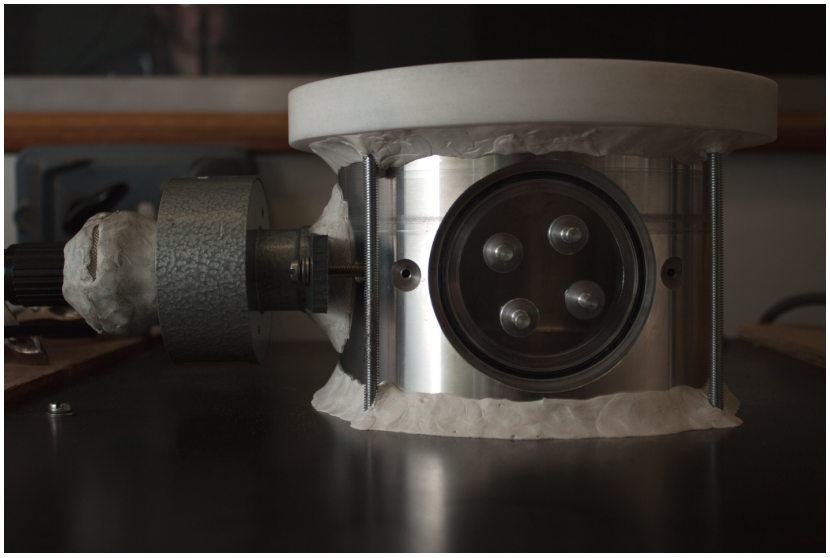

Figure 5.3: Vacuum chamber.

5.2 Biased Cavity Voltage

A literature review indicated that the entire TM_{010} resonant cavity needed to be raised to a bias positive voltage potential in order for the ion optics system to work sufficiently [7]. The high positive potential reduces the probability of ions colliding against the wall of the cavity as the two positively charged (cavity and ion) species will repel one another. Thereby the plasma is ensured to be in the centre of the cavity. The positive potential of the cavity is typically raised a few hundred volts higher than the screen grid of the ion optics. This voltage difference between the cavity and screen grid assists the positive ions to drift towards the ion optics for extraction and acceleration. The configuration of a positive biased cavity is normally easily achievable when electrodes are used for the purpose of gas ionisation. However, it becomes a challenge when electromagnetic waves are used to ionise the propellant. This is because the resonant cavity is directly coupled to the waveguide, which is connected to the electrical ground of the magnetron's power supply. As a result, the power supply's electrical ground needs to be raised to a bias voltage for the cavity to have a positive voltage. This is, however, not an easy task as the dual directional coupler, which is also connected to the magnetron's electrical ground, will be affected by the high bias voltage. In addition, the magnetron's power supply is fairly complex and as such, a different solution was required.

5.2.1 Preliminary Design

Instead of modifying the complex switch mode power supply of the magnetron, the cavity was insulated from the waveguide with a low dielectric material. This solved not only the problem for the high bias voltage, but also served as a vacuum seal for the cavity.

Mica Sheet Concept

Mica sheets are commonly used in microwave ovens to cover the waveguide from the substance being heated in the microwave. The initial concept entailed inserting a Mica sheet between two waveguide flanges with a Viton® O-ring to ensure vacuum. However, initial tests revealed that the Mica sheet was not dense enough to seal the cavity for low vacuum pressures.

Microwave Substrate Concept

The second concept entailed the use of a microwave substrate. Microwave substrates are relatively cost effective and have low dielectric losses. A simulation of the proposed concept was performed in CST Microwave Studio software with a simplified model, as illustrated by Figure 5.4, to analyse what affect the substrate will have on the system.

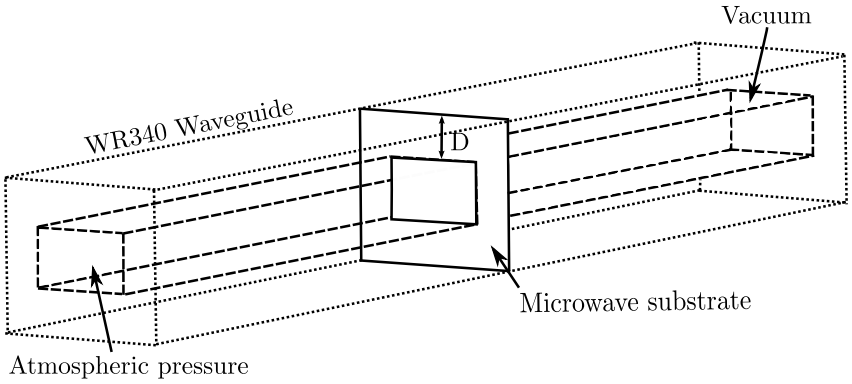

Figure 5.4: Simplified CST substrate concept.

The simulation was performed with 1.6 *mm* thick *Rogers 4350* microwave substrate with $\epsilon_r = 3.58$. A parameter sweep was included for dimension D (see Figure 5.4), from 29 *mm* to 37 *mm*, to calculate the optimal dimension that will ensure the best S_{11} and S_{21} parameters. Figure 5.5 and Figure 5.6 show the simulation of the return loss (S_{11}) and insertion loss (S_{21}), respectively. As indicated in Figure 5.5 and Figure 5.6, a substrate dimension of approximately $D = 32\ mm$ ensures minimal reflected power S_{11} and insertion loss S_{21}, at the operating frequency of 2.45 GHz.

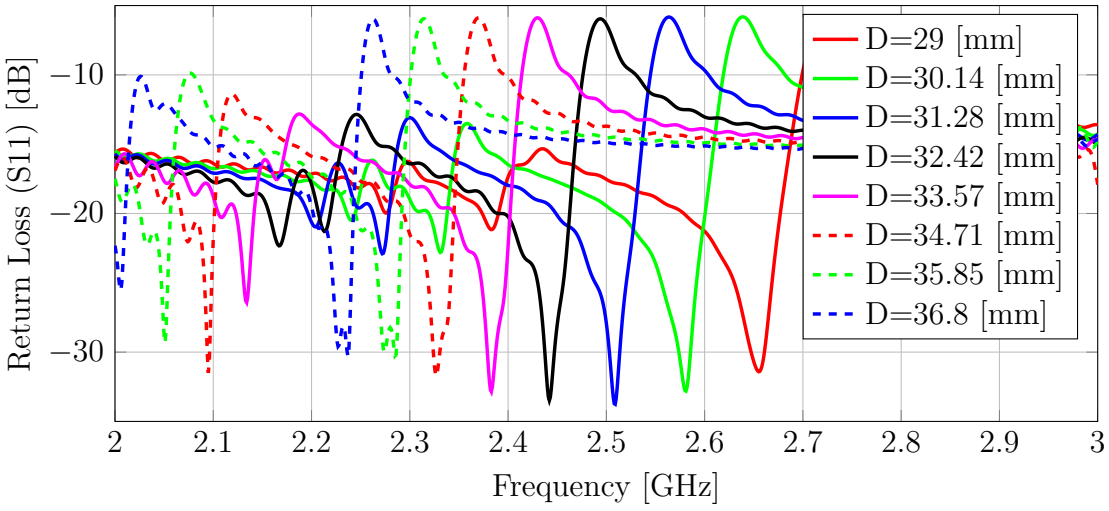

Figure 5.5: Return loss for different substrate diameters.

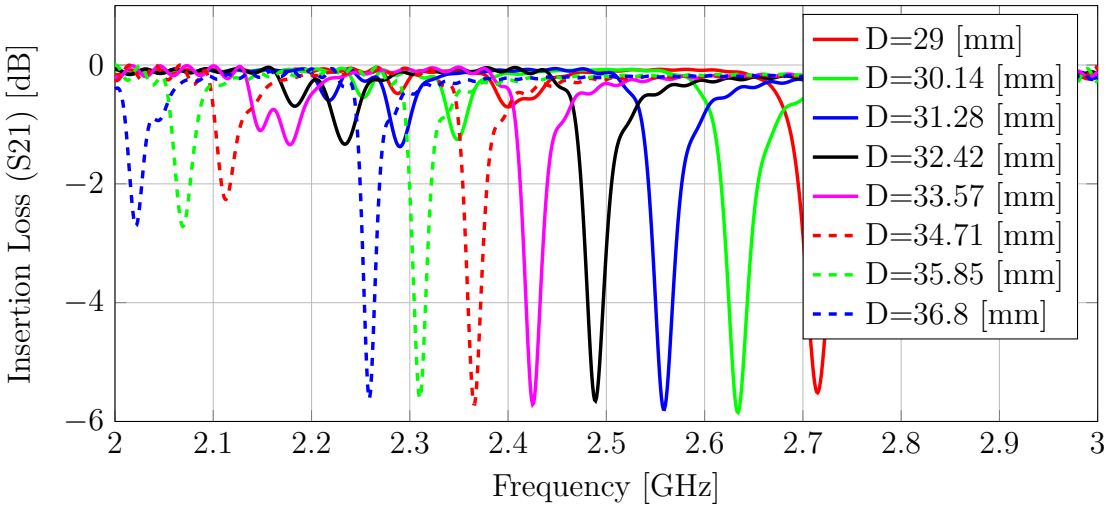

Figure 5.6: Insertion loss for different substrate diameters.

The width of the substrate was reduced to a minimum, that could withstand the force of the vacuum pressure, in order to improve the results. As a result, a substrate with a width of 1 mm and a diameter of $D = 32$ mm was chosen. Figure 5.7 indicates that the amount of power reflected is substantially smaller in comparison to results obtained from a substrate thickness of 1.6 mm. Also, the insertion loss, as shown in Figure 5.8, is almost zero at the 2.45 GHz operating frequency.

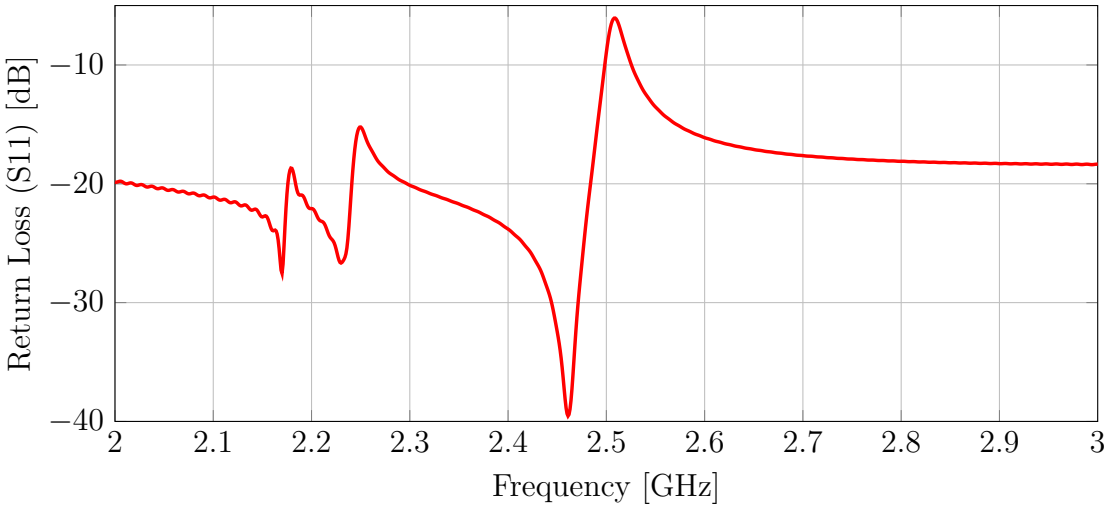

Figure 5.7: Return loss for microwave substrate at D=32mm.

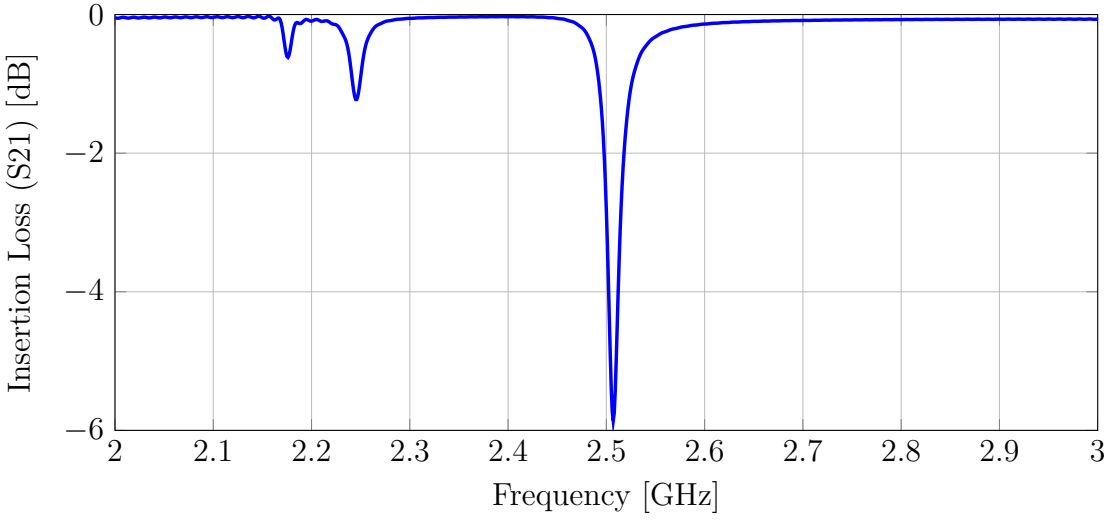

Figure 5.8: Insertion loss for microwave substrate at D=32 mm.

The amount of RF leakage through the microwave substrate was estimated by calculating the S-Parameter Balance in CST. The S-parameter balance is calculated as the square root of the summed power that leaves the structure through the ports. The S-parameter balance is defined, for a one port system, as

$$Balance_1 = \sqrt{\mid S_{11} \mid^2 + \mid S_{21} \mid^2}. \tag{5.2.1}$$

Figure 5.9 shows the S-parameter balance for the 1 mm substrate. As can be determined from Figure 5.9, minimal radiation has leaked out through the substrate with a power balance of approximately 0.98 at 2.45 GHz.

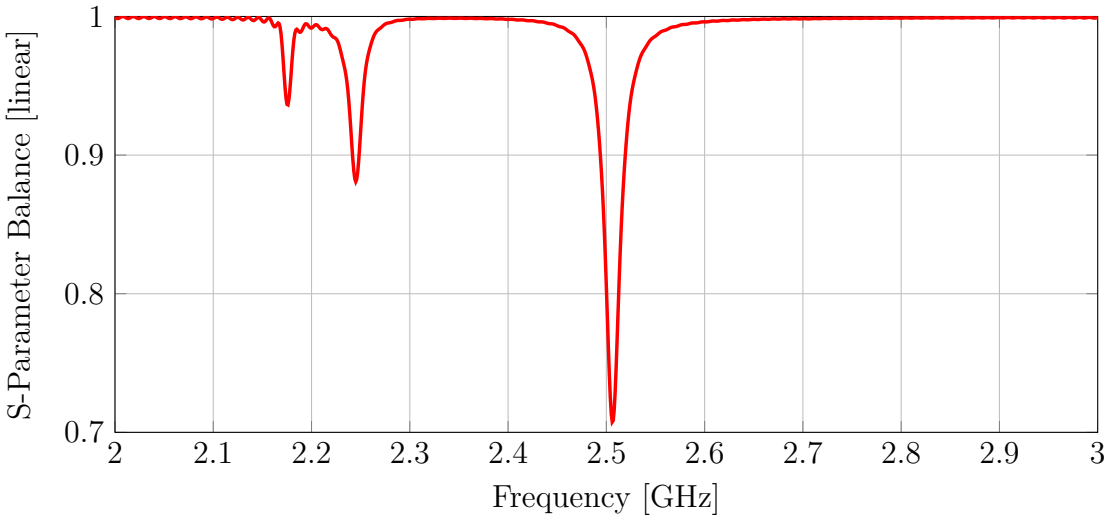

Figure 5.9: S-Parameter Balance.

5.2.2 Final Design

The final design of the substrate is shown in Figure 5.10. The 'film' was stripped according to the WR340 waveguide dimensions, allowing the microwaves to propagate through the substrate into the cavity. Also, the substrate was tightly clamped between the two waveguide flanges with Viton® O-rings to ensure a vacuum inside the cavity, as shown in Figure 5.12.

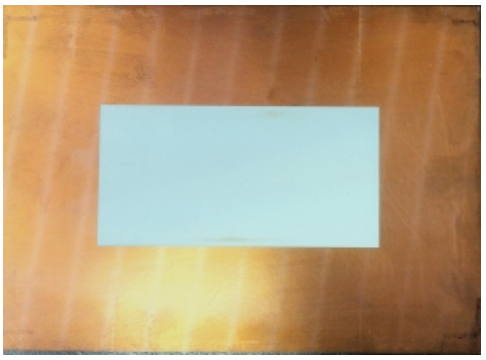

Figure 5.10: Final design of microwave substrate.

5.2.3 Verifying Microwave Substrate

Dielectric Losses of Substrate

Initial tests showed that the microwave substrate heats up fairly quickly when introduced to approximately 500 W of microwave power due to the dielectric losses of the substrate. As a result, the substrate fails if testing is done for more than a few minutes, as shown by Figure 5.11.

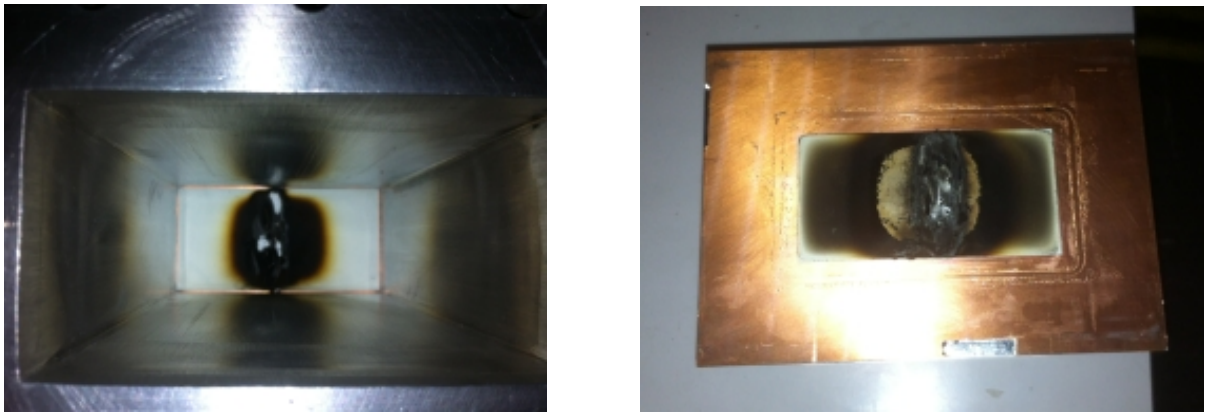

Figure 5.11: Illustration of microwave substrate failing during tests.

To overcome this limitation, a small hole was made in the waveguide, at the input power side, as shown by Figure 5.12 . This introduced compressed air into the system for cooling purposes. Testing concluded with the finding that cooling is sufficient for experiments to be performed for 20 minutes without substrate failure.

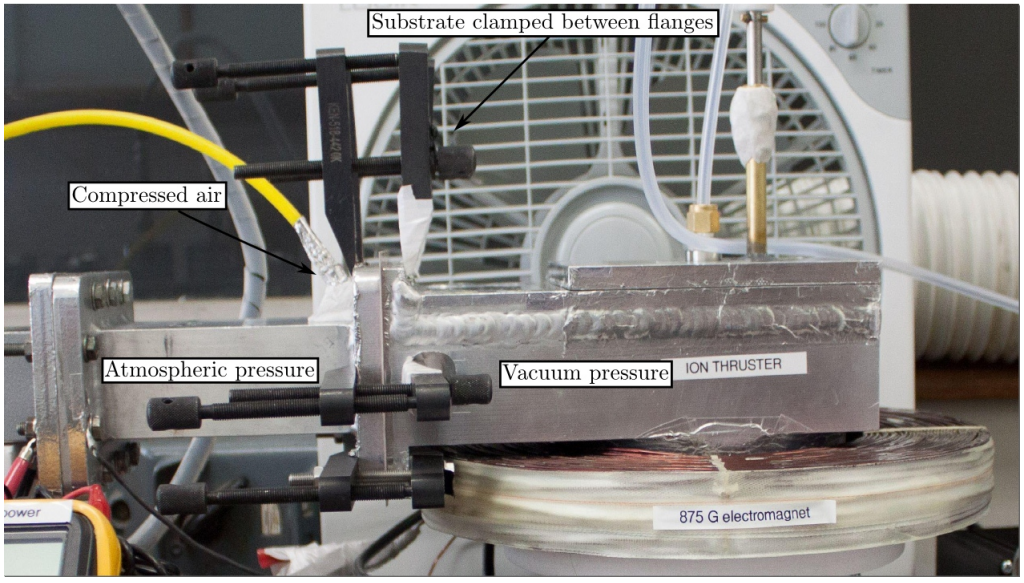

Figure 5.12: Substrate assembled between two waveguide flanges.

RF leakage

Microwave radiation was tested with a survey meter to determine the level of leakage through the substrate. The maximum radiation leakage documented was 20 mW/cm^2 when measured in close proximity to the microwave substrate. A range of between $1 - 8$ mW/cm^2 of radiation leakage was verified when tests were done at distances of 50 cm and further. According to the FDA, this leakage is far below the level stipulated to be harmful to humans.

5.3 Gas Injection and Plunger

It is essential to inject the neutral gas into the area of maximum electrical field distribution to ensure efficient ionisation. Therefore, the argon gas was injected in the centre of the cavity via a 1/4 in. Swagelok® fitting. The flow rate was controlled with a precise needle valve and adjusted to determine correlations between flow rate, input power and performance.

Due to the unavailability of a three-stub tuner to match the impedance of the magnetron and waveguide to the cavity, the resonant frequency of the cavity may change and some of the microwave energy may reflect back to the magnetron. This may result in insufficient power to ionise the propellant. A sharp tungsten bit plunger was added to the system to solve this problem as a precaution for the ionisation of the neutral gas. The plunger was added in close proximity to the gas inlet to assist in producing a maximum electrical field intensity at the gas inlet. Figure 5.13 below illustrates this setup.

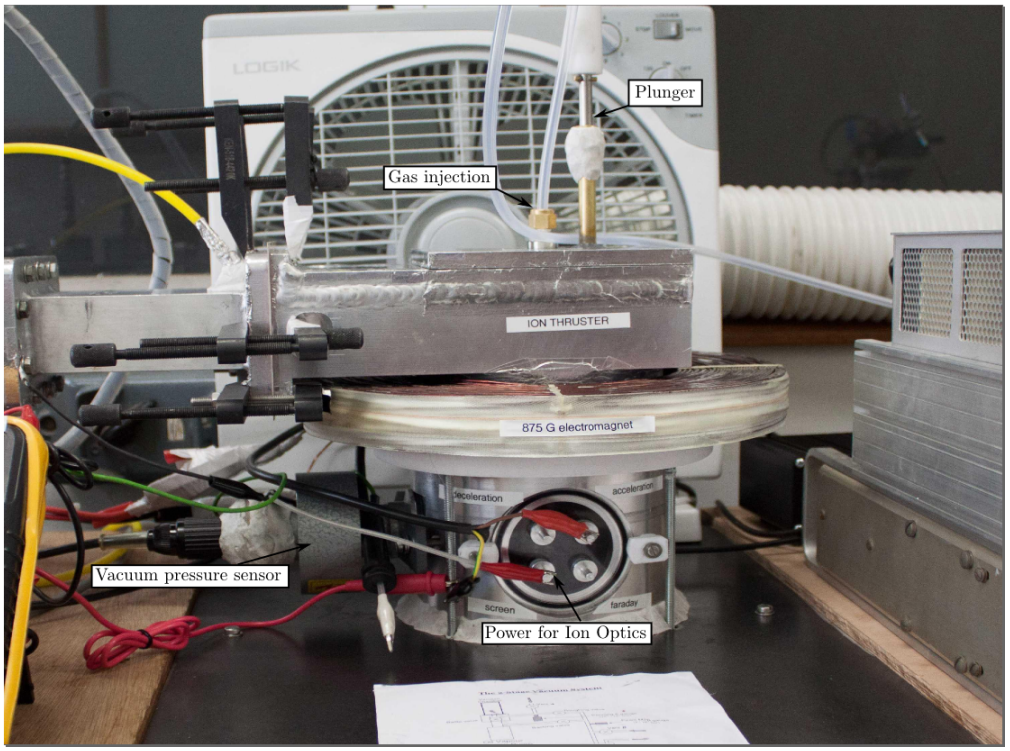

Figure 5.13: Illustration of gas injection method and plunger.

5.4 Electromagnet

The cavity is designed to use the ECR method to ionise the propellant, as discussed in section 2.2.3. The process of ECR will ensure that the thruster produce an efficient and high density plasma. An external magnetic field is required in order to use the electron cyclotron discharge technique. Here, a resonance condition is exploited that occurs when the gyration frequency of the electrons ($f_e = \omega_e/2\pi$) is equal to the microwave frequency ($f_0 = \omega_0/2\pi$). The magnetic field is typically produced by permanent magnets (Samarion-Cobalt) [28; 33], which are stacked around the discharge chamber, and the resonance region is often localised to a small zone inside the thruster. The small zone assists the permanent magnets to produce high magnetic field resonant regions. Due to the difficulty in producing high magnetic field resonant regions throughout a large discharge chamber volume with permanent magnets, it was decided to use an electromagnet. The electromagnet ensures a larger resonant region, and magnetic field divergence assists in spreading the plasma over the grid region for extraction.

5.4.1 Preliminary Design

The electromagnet was designed to be assembled around the combustion chamber. This ensures that the plasma is contained in the centre of the cavity and that the ions are directed towards the ion optics, as illustrated in Figure 5.14. Equation 2.2.24 was used to calculate the resonance condition for an operating frequency 2.45 GHz. It was found that the ECR region for argon gas is met when the magnetic field region is approximately $B = 874\ G = 0.00875\ T$.

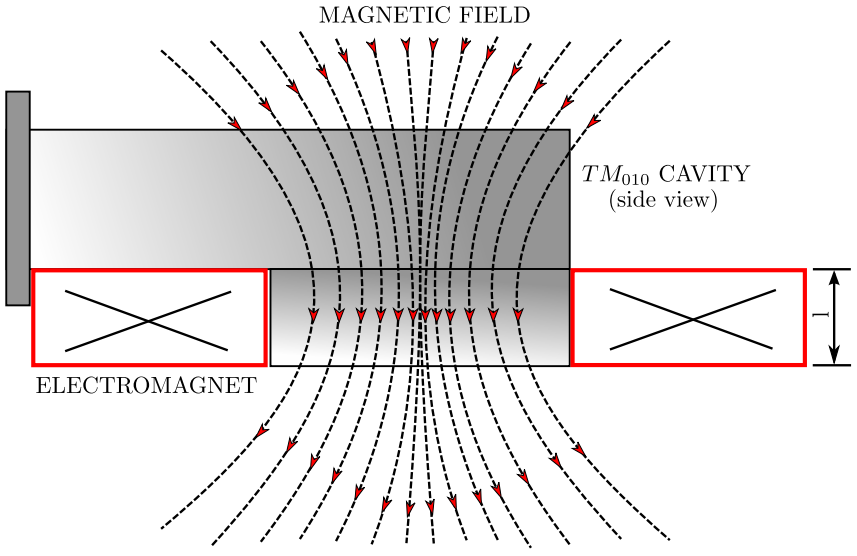

Figure 5.14: Preliminary electromagnet design.

A calculation was done to determine the optimal wire thickness, that will produce a magnetic field of 874 Gauss for an electromagnet, with dimensions that accommodate the cavity and the vacuum chamber. The magnetic field was calculated from Equation 5.4.1

$$B = \frac{\mu_0 N I}{l}, \tag{5.4.1}$$

where B is the magnetic field strength, N is the number of turns, I is the current and l represents the thickness of the electromagnet.

Figure 5.15 shows the maximum magnetic field strength in the centre of the electromagnet for various AWG Gauge wires. The maximum field strength shown in Figure 5.15 took into account the DC supply (200V @ 20A) that was available for the experiment, as well as the maximum current for each AWG Gauge wire.

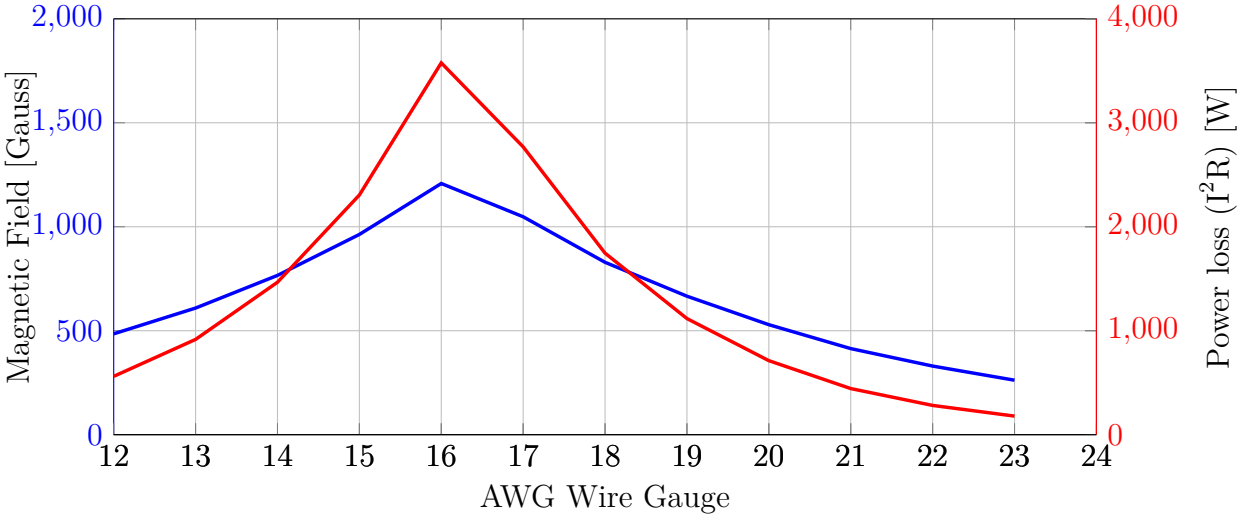

Figure 5.15: Magnetic field strength and power loss.

5.4.2 Final Design

After analysis of the results found in Figure 5.15, a 15 Gauge wire was chosen to be used for the electromagnet. Although a 16 Gauge wire will ensure greater magnet field strength with the DC power supply available, the power loss I^2R is far greater. The final design for the electromagnet is shown in Figure 5.16.

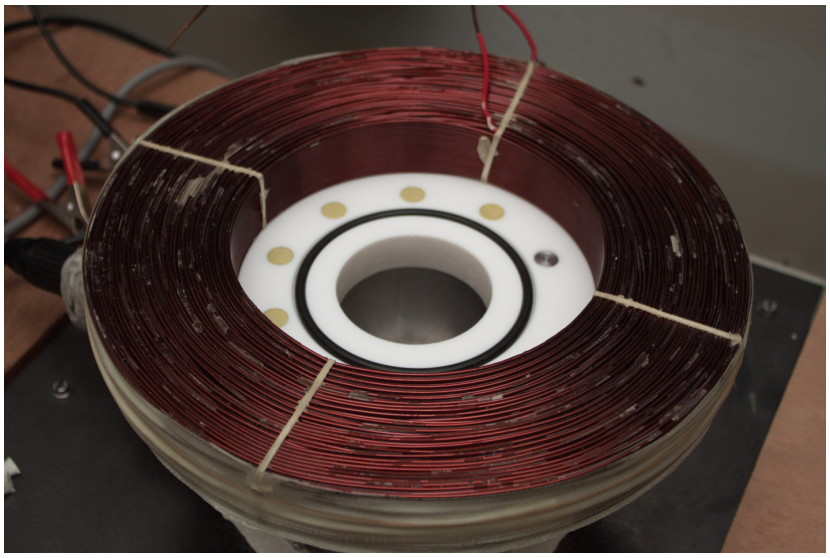

Figure 5.16: Final design of electromagnet.

5.4.3 Verifying Electromagnet Operation

A direct measurement was done with a Gauss Meter to confirm that the electromagnet is sufficient in generating the resonant region for the process of ECR. The direct measurement yielded a maximum magnetic field strength of approximately 920 Gauss at the centre of the electromagnet. Nonetheless, a sufficient amount of air cooling was required to ensure that the shielding of the electromagnet wire does not overheat.

5.5 Thrust Measurement

A variety of direct and indirect thrust measurement techniques exist for electric thrusters. The technique utilised depends on the thrust type (pulse or constant), the thruster range as well as the vacuum chamber size used for the experiment. Consequently various types of thrust measurements were studied to determine an appropriate technique for the RF ion thruster.

Direct Thrust Measurement

Cubbin *et al.* [36] used a direct measurement technique by designing an optical interferometric system that measured the deflection of a swinging arm supported by frictionless pivots. The deflection was determined by detecting the phase difference between two laser beams reflected off the arm. The system could measure thrust impulses between 100 μN and 10 N. Lun [37] used a simplified technique of this system by measuring the deflection of a thin cantilever beam fixed at one end with strain gauges. A depiction of the method is shown in Figure 5.17.

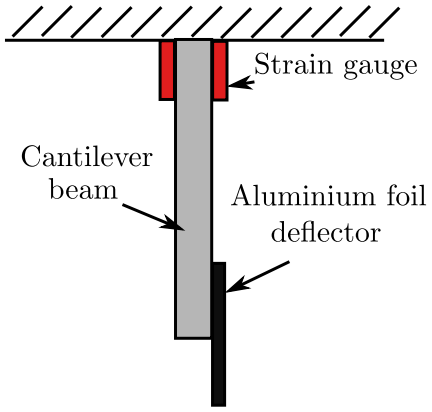

Figure 5.17: Schematic of Lun's thrust measurement technique [37].

Lun's thrust measurement technique had a few drawbacks. The deflection of the beam was too small to be detected by the strain gauges when small thrust was measured. In addition, the technique could only measure thrust once the vacuum pump had been switched off because vibration from the pump interfered with the strain gauges readings.

Indirect Thrust Measurement

The method of indirect thrust measurement was also studied. This method determines the thrust by utilising the information of the propellant mass flow rate and the propellant velocity (see Equation 2.1.1). Ganguli *et al.* [28] and Byron *et al.* [38] developed an ion collector system that measures the amount of ions ejected by the thruster. This collection is usually achieved by a large collector plate or Faraday cup to absorb the ions and results in a measurable current flow through a circuit. Bias voltages are typically used with the collector plate to attract ions and repel electrons. In addition, Langmuir probes are often used to determine the bulk plasma density, electron density and plasma potential of the extracted beam [39; 28].

5.5.1 Design

The direct measurement system is more accurate in determining the thrust compared to the indirect method. The direct transfer of energy, due to ions and electrons, is measured by the direct method. In contrast, the indirect method will only measure a small portion of the thrust and only take the contribution of ions into consideration. Yet, due to the space limitation inside the vacuum chamber, the indirect method was used to determine the thrust in this thesis. This was achieved by placing a 20 cm^2 stainless steel sheet approximately 20 mm away from the thruster's ion optics.

A 1.8 $k\Omega$ resistor was connected between the collector plate and ground, as shown by Figure 5.18. The voltage was measured across the resistor to obtain the current of the ions with Ohm's law. This represents the current that is induced by the collision of ions against the collector plate.

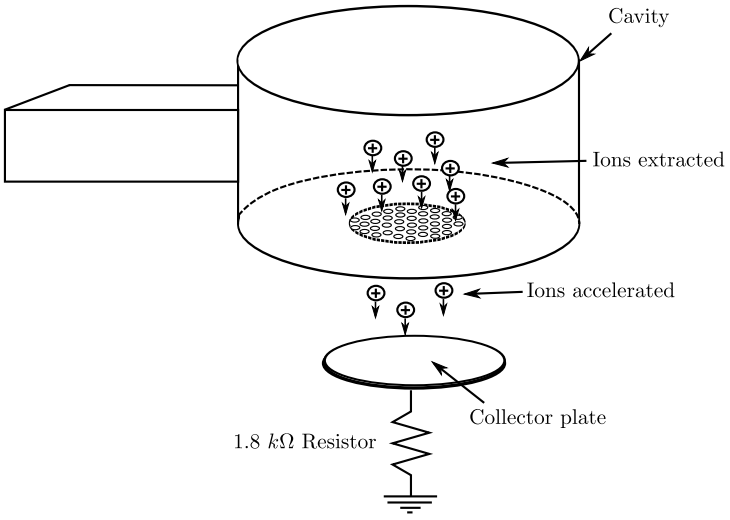

Figure 5.18: Indirect method for measuring thrust.

Secondary Electron Emission

The ions that collide against the collector plate have a certain amount of kinetic energy. When this kinetic energy is high enough, electrons can be displaced from the surface of the collector plate. This effect is known as secondary electron emission and can cause the ion current measured to be overestimated. Electrons will generally flow in the opposite direction to that of the ions, which produce a current flow in the same direction as if ions had been collected, and an overestimation of current flow results. To determine if secondary electron emission will affect the measurement results, the kinetic energy of the ions need to be estimated with

$$E_{k,ion} = \frac{1}{2} m_i v_i^2. \tag{5.5.1}$$

Assuming that the average speed of an ion [2] is approximately 30 km/s, the kinetic energy of an argon ion is approximately 188 eV, as calculated with Equation 5.5.1 . However, several sources ([38; 40; 37]) showed that the effect of electron emission is only significant for ions with kinetic energies greater than 1keV. Therefore, the effect of secondary electrons were neglected in the ion current measurements.

[2] Byron *et al.* [38] and Ganguli *et al.* [28] found that the average speed of ions is between 30-50 km/s.

5.6 Test Setup

The final setup for the RF Ion Thruster is shown in Figure 5.19. The setup consisted of a 600 W magnetron, with a WR340 launcher, connected to a circulator. The purpose of the circulator was to prevent the reflected power from propagating back into the magnetron, causing heating and failure of the magnetron. In addition, a dual directional coupler with two zero bias Schottky detectors was included to determine the transmitted and reflected power. Finally, the dual directional coupler was connected to the cylindrical TM_{010} resonant cavity. The microwave substrate designed in section 5.2.1 was inserted between the two waveguide flanges and clamped tightly. Lastly, the electromagnet was placed between the thruster and the vacuum chamber. All the sections were closed with aluminium tape to keep RF leakage to a minimum and prevent a capacitor charge being formed.

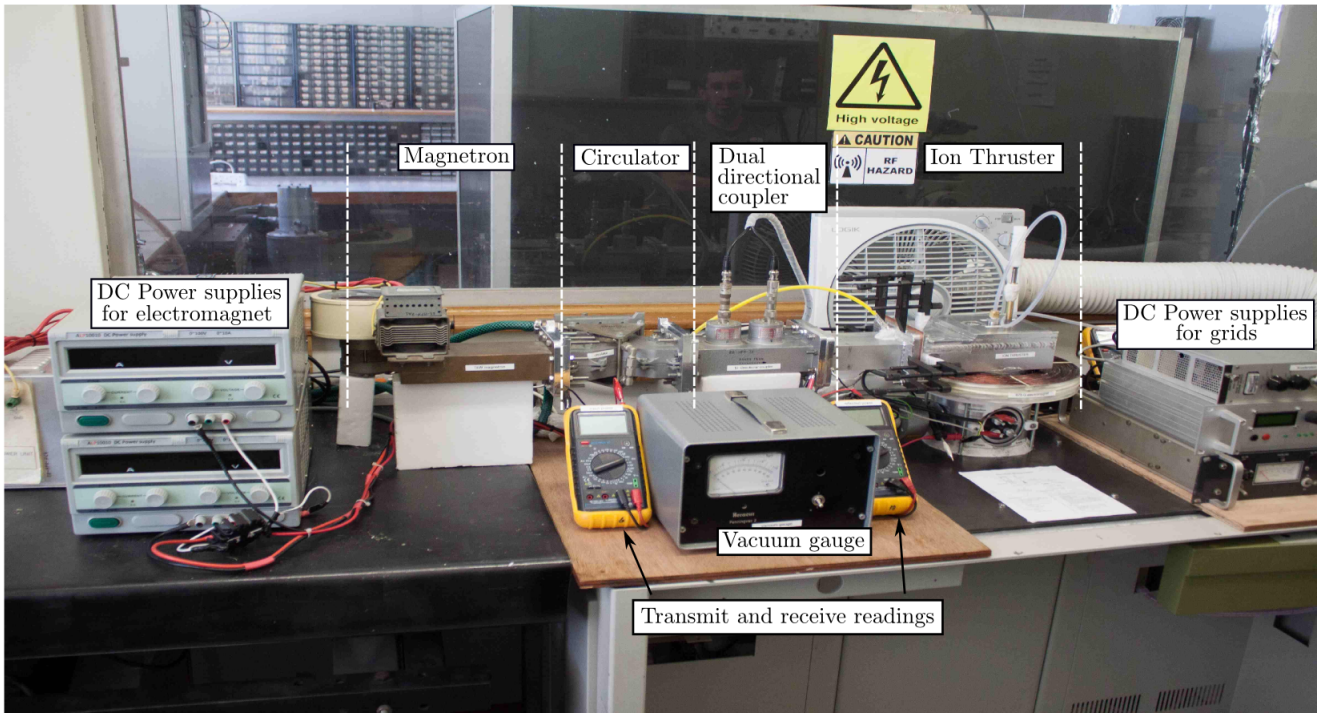

Figure 5.19: Final experimental setup for the purpose of testing the designed ion thruster.

The ion optics voltages were procured through the ports designed in the vacuum window. Unfortunately, only one high positive DC power supply was available. Thus the cavity and the screen grid were placed at the same voltage potential. A schematic of the system potentials is shown in Figure 5.20.

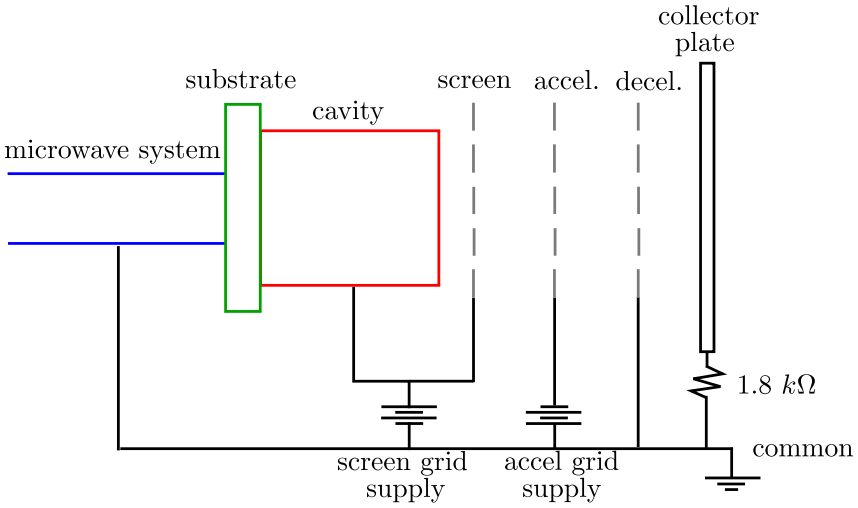

Figure 5.20: Schematic of system potentials.

5.7 Summary

The experimental elements needed to test the operation of the ion thruster, designed in chapter 3, were discussed in this chapter. Firstly, a two stage vacuum chamber was implemented, which could reach pressures as low as 10^{-6} $Torr$, in order to verify the operation of the thruster. Findings demonstrated that the cavity needed to be raised to a high positive bias voltage. Thereby the optimal operation of the ion optics could be ensured. An optimal microwave substrate was designed and implemented between the cavity and magnetron to protect the magnetron's power supply from this bias voltage. Also, in order to use the ECR process, a 910 Gauss electromagnet was designed and manufactured. Furthermore, the entire experimental setup was discussed. The setup consisted of a magnetron connected to a circulator to protect the magnetron from the reflected power. A dual-directional coupler was also introduced in order to determine the transmitted and reflected power of the entire system. Finally, various thrust measurement techniques were discussed and the technique of indirect thrust measurement was implemented. This was achieved by measuring the extracted ion beam, by introducing a 20 cm^2 stainless steel sheet into the extracted ion plume. The thrust could be determined by substituting the ion beam current into Equation 2.1.4.

Chapter 6

Tests and Results

The previous chapters discussed the design and manufacturing of an RF ion thruster. Up until this point, the performance of the ion thruster was predicted and the experimental work necessary for the testing of the ion thruster was explained. Extensive testing was necessary to determine the feasibility of the ion thruster after it was implemented. In this chapter, the testing procedures used to determine essential performance parameters including thrust, specific impulse, and efficiency are explained.

6.1 Ionisation Through Microwave Energy

The first series of experiments concentrate on the cavity feasibility to successfully ionise argon gas. The effects of various parameters were studied in order to determine the optimal conditions for operation. The ionisation of argon gas is dependent on a variety of parameters. The electrical field intensity produced inside the cavity, the frequency of the electron oscillation and the gas pressure, were the main parameters examined. The following subsections will focus on the effects these parameters have on the ionisation of neutral argon gas.

6.1.1 Necessity of Plunger

The goal of the first experiment is to determine the necessity of introducing the plunger for successful ionisation. In order to accomplish this, the vacuum chamber is pumped down to approximately 2×10^{-5} $Torr$ via a roughening pump followed by a diffuser pump. Appendix A provides a detailed explanation of the vacuum system procedure. When the cavity is at vacuum pressure the magnetron is switched on and the argon gas is injected into the cavity. The argon gas is controlled by an external needle valve until ionisation occurs. The ionisation of the argon gas is confirmed with the presence of a bright violet light inside the microwave cavity.

As part of the experimental setup described above, argon gas was injected into the cavity. The absolute pressure was decreased from 10^{-5} $Torr$ down to 10^{-2} $Torr$, by controlling the argon gas flow rate, to establish the pressure of 'ignition'/ionisation. Previous research showed that the gas breakdown occurs at a gas pressure between 10^{-4} $Torr$ and 10^{-3} $Torr$ [33; 28; 41]. Thus, it was expected that the breakdown will occur at the same pressure range. The first couple of tests did not include the extraction and acceleration process of ions. Therefore, the lid of the cavity was modified to obtain a visual of the inside of the cavity. This modification was achieved by implementing a circular pattern of holes drilled into the lid and sealed with a glass slide and O-ring. The diameter of the holes were chosen to be small enough to ensure zero radiation leakage. In the absence of a bright violet light, the results of the experiment indicated that the maximum electrical field distribution inside the cavity was not capable of ionising the argon gas. As a result, a sharp tungsten bit (plunger) was added to the system. Consequently, a bright violet light was observed at approximately 9×10^{-3} $Torr$ with the plunger added and the argon gas injected into the cavity, as shown in Figure 6.1.

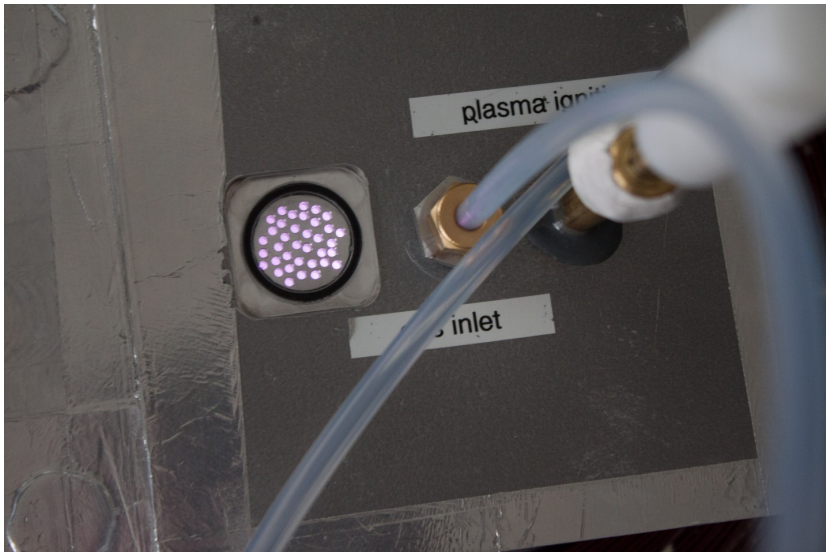

Figure 6.1: Successful plasma ignition with plunger.

The sharp tungsten bit was removed upon 'ignition' of plasma to determine the capability of plasma sustainment without the plunger present. Although the plasma is sustainable through the microwave energy without the plunger, it was found that the plasma density and energy was much lower. This was verified by a dim violet light inside the cavity.

A difficulty became apparent in distinguishing the plasma density at different pressure conditions due to the unavailability of a Langmuir probe. However, one detail that was noticeable during the tests was that the plasma was brighter in colour and had higher temperatures at higher operating pressure conditions. During low pressure conditions,

the plasma could be sustained for long time periods without any material failure. Once the pressure was increased, and the plasma sustained for 5 to 7 minutes, the plunger's temperature would increase to a point where the O-rings surrounding the plunger would fail, as shown by Figure 6.2.

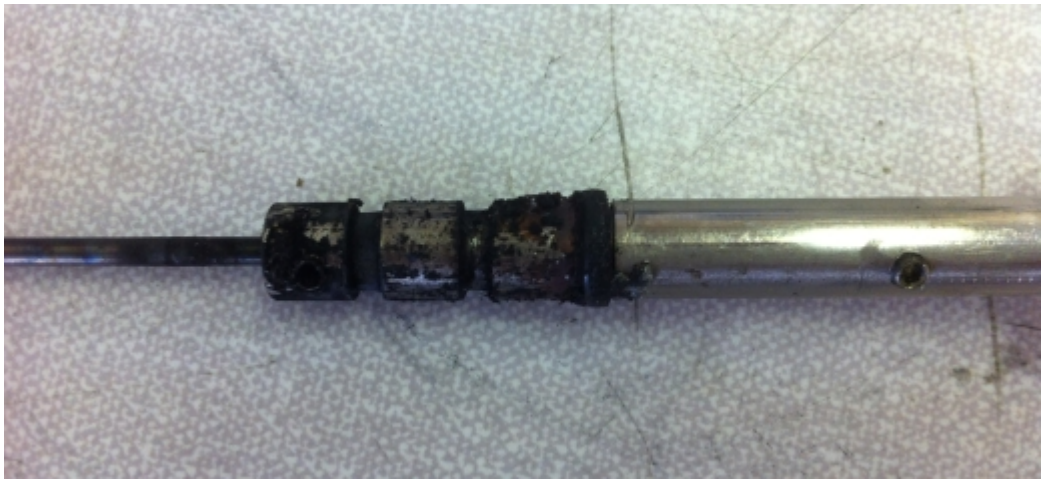

Figure 6.2: Plunger O-ring failure.

Measured Results

Experiments were conducted with and without the plunger and are summarised in Table 6.1. Results indicated that without any argon gas inside the cavity, almost all the microwave energy was reflected (86%) and was dumped, through the circulator, into the water-cooled dummy load. This result supports what was expected, because there was no 'load' present in the cavity to absorb the microwave energy. It is important to note that some percentage of microwave energy was lost due to the dielectric losses of the microwave substrate and the cavity. Yet, once the plunger and argon gas was added to the cavity, the plasma was 'ignited' and the reflected power was decreased to approximately 65%. This indicates that the plasma was absorbing some of the microwave energy. The density of the plasma was decreased upon removing the plunger. However it was still sustainable with approximately 73% of microwave power being reflected. Nonetheless, a further increase in argon gas flow rate resulted in the dissipation of the plasma and the reflection of all the microwave power.

Table 6.1: Experimental results, with and without plunger.

Transmitted Power [W]	Reflected Power [W]	Cavity Pressure [Torr]	Method	Result
400	345	2×10^{-5}	None	None (no gas)
400	305	2×10^{-5}	Plunger	None (no gas)
395	260	9×10^{-3}	Plunger	Bright plasma
390	255	5×10^{-3}	Plunger	Bright plasma
395	290	5×10^{-3}	None	'Dimmed' plasma
400	304	1×10^{-3}	None	Plasma dissipates

An analysis of the results obtained indicates that only a small portion of the microwave energy is being absorbed by the plasma, which indicates that only a low plasma density is sustainable. Furthermore, the results show that the plasma is only sustainable up to a certain point. An increase in the gas flow beyond this point results in the dissipation of the plasma. This phenomenon is due to the recombination rate of charge particles being greater than the ionisation rate. The process of ECR can be introduced in order to overcome this limitation. This ECR process, as stipulated in theory, will assist with the propagation of microwaves into the plasma, and result in the production of a denser plasma.

6.1.2 Effect of ECR

The second experiment was done to substantiate the process of electron cyclotron resonance (ECR). Argon gas was slowly fed into the cavity, by following the same experimental setup as before, but with the presence of a strong magnetic field, until ionisation occurred. Interestingly the bright violet light was already visible at a pressure of 2×10^{-4} $Torr$ and was achieved without the plunger. A further pressure increase resulted in the production of brighter plasma, as shown by Figure 6.3.

The experiment verified the theory stated in section 2.2.3. The experiment results confirmed that when the electrons of the argon gas are introduced to a magnetic field region of 875 G, then the electrons will start to oscillate at the same frequency as that of the supplied microwave energy. This resulted in the absorption of microwave energy, which lead to a high plasma density. Here it was seen that the process of ECR not only assisted in sustaining a higher plasma density, but also started the process of ionisation. Thus the plunger was found to be obsolete for 'ignition' purposes.

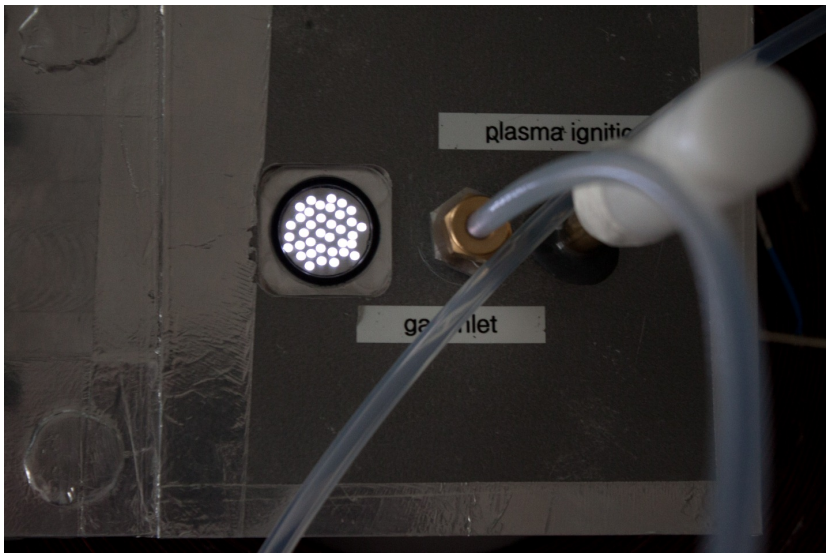

Figure 6.3: High plasma density with magnetic field present.

Measured Results

Experiments were completed using the ECR process and are summarised in Table 6.2. Results indicated that only 33% of the microwave power was being reflected when the process of ECR was implemented. This high power absorption rate resulted in a high plasma density being produced. A reduction in the magnetic field region resulted in a greater amount of microwave power reflected (45%), thus a less dense plasma being produced. Therefore, the percentage of microwave power absorption was seen to be directly proportional to the strength of the magnetic field region. Furthermore, the optimal operating pressure was found to be 4×10^{-4} $Torr$, with only 23% of the microwave power being reflected. The results obtained in Table 6.2, demonstrated that the ECR process significantly improved the performance of the ion thruster.

Table 6.2: Experimental results with ECR.

Transmitted Power [W]	Reflected Power [W]	Cavity Pressure [Torr]	Method	Result
400	345	2×10^{-5}	None	None (no gas)
410	150	2×10^{-4}	Electromagnet (875 G)	Plasma
395	93	4×10^{-4}	Electromagnet (875 G)	Dense plasma
395	180	4×10^{-4}	Electromagnet (430 G)	Plasma
400	190	8×10^{-4}	Electromagnet (875 G)	Plasma
400	340	2×10^{-3}	Electromagnet (875 G)	Plasma dissipates

6.2 Extraction and Acceleration

As the operation of the designed microwave cavity was substantiated by the initial test, the experimental focus shifted to the operation of the ion optics. The ion optics are considered to be the most crucial part of an ion thruster and needs to be thoroughly tested. A variety of parameters, including the voltage potentials of the grids and the plasma density at the grids, affects the successful operation of the ion optics. The following subsections examine these parameters in order to determine the optimal conditions for the ion optics.

6.2.1 Optimal Conditions

The first consideration was the operating pressure that should be used with the ion optics. The previous experiments found the optimal pressure for ionisation to be between 2×10^{-4} $Torr$ and 5×10^{-4} $Torr$. Therefore, the working pressure used started at 2×10^{-4} $Torr$. At this pressure, the screen grid and acceleration grid could operate, without any arching being observed, at 1500 V and -250 V, respectively. As the ion optics were introduced to the system, the ions produced inside the cavity were extracted through the apertures of the grids. At first the ion beam was not focused, as shown in Figure 6.4. However, the voltages were tweaked until a focused ion beam was produced, as shown in Figure 6.5. The optimal potentials were found to be 1100V and -200 V for the screen and acceleration grid, respectively.

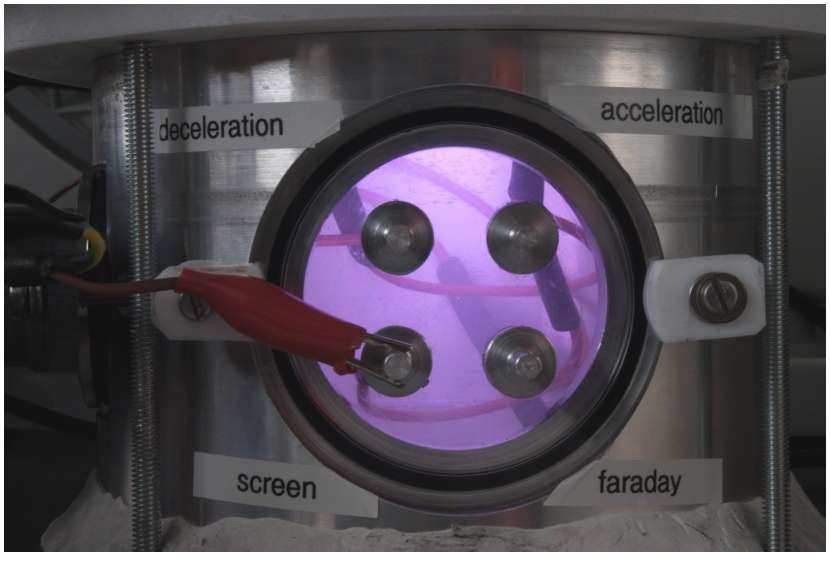

Figure 6.4: Partially extracted ion beam.

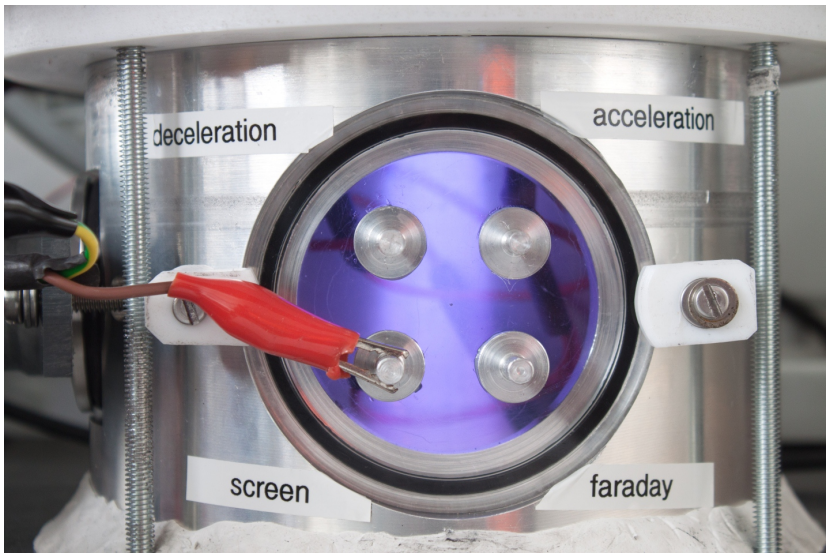

Figure 6.5: Extracted and accelerated ion beam.

An increase in gas flow rate resulted in an increase in pressure of up to 5×10^{-4} $Torr$. This yielded a brighter dense violet ion beam being extracted and accelerated through the ion optics, as shown in Figure 6.6. However, the extracted ion plume decreased with an increase in pressure beyond 7×10^{-4} $Torr$. This can result from the plasma sheath forming a flat sheath at each aperture, leading to ions impinging the acceleration grid instead of being accelerated through the grids, as explained in section 3.2.2.

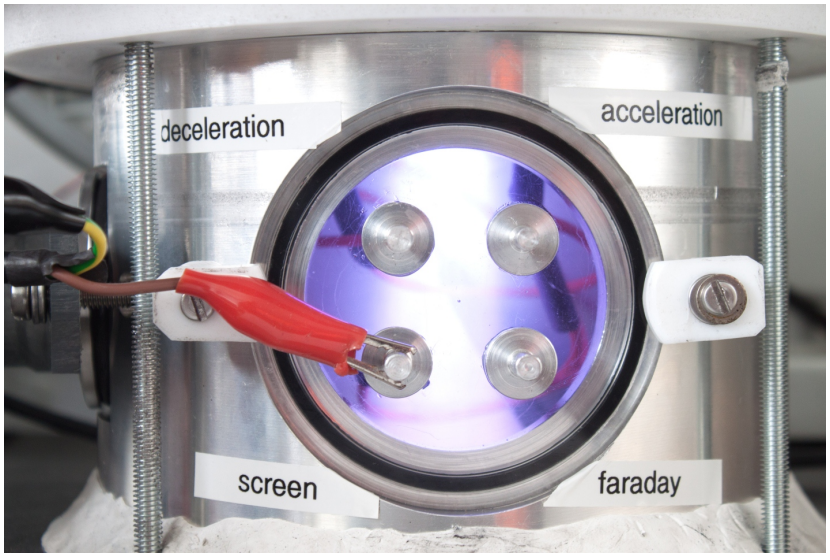

Figure 6.6: Optimal ion beam extraction and acceleration.

Power Supply Limitation

Although the ion optics were successful in extracting and accelerating the ions, the extracted ion beam was unfortunately not constant during the entire process. This phenomenon was initially thought to be a result of the microwave energy not being able to produce constant plasma during the operation of the ion optics. However, verifying a constant bright violet light inside the cavity during the operation of the ion optics, this hypothesis was eliminated. Further investigation revealed that the 'pulsed' ion beam is a result of the current operating conditions of the power supplies. The low current ratings of the power supplies caused the ion beam only to be visible, up to a point, where the power supply's current limit was reached. This resulted in a 'pulsed' ion beam being extracted and accelerated. The plasma density inside the cavity was also limited by the current ratings[1], because the cavity and screen grid were both biased with the same power supply.

6.2.2 Current Measurement

The ion current that could be extracted through the ion optics was the last result to be determined. Following the current measurement method discussed in section 5.5, a 20 cm^2 circular plate was inserted into the vacuum chamber with a 1.8 $k\Omega$ resistor connected to ground. An Oscilloscope was connected to the resistor and the voltage was measured across the resistor, to determine the ion beam current according to Ohm's Law.

Previous experiments found that the optimal condition for the ion thruster was at an pressure of 5×10^{-4} $Torr$ with a magnetic field region of approximately 875 Gauss. The optimal voltages for the ion optics were indicated as 1100 V and -200 V for the screen and acceleration grid, respectively. The experimental process was started and the ion beam current was measured with these optimal conditions taken into consideration. The maximum ion beam current obtained was approximately 57 mA, as shown in Figure 6.7. This ion beam current was, however, not constant during the entire operation, due to the current limitation of the power supply. A constant ion beam could be obtained when the argon gas flow rate was increased to an operating pressure of 7×10^{-4} $Torr$. This resulted in a less dense plasma being formed and thus the power supply not reaching the current limit. The ion beam current was, however, lower with an ion beam current of 25 mA.

[1]The current is produced due to the electrons, that are produced during ionisation, being attracted to the positive potential cavity. Thus, higher plasma density results in an increase in electrons and hence, a greater current.

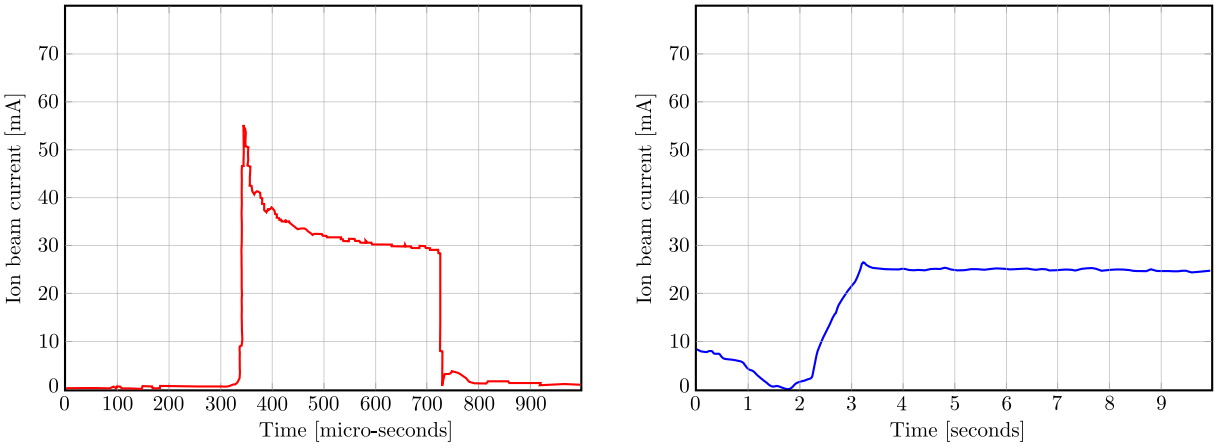

(a) Maximum ion beam current obtained.

(b) Constant ion beam current obtained.

Figure 6.7: Ion beam current measurements.

6.2.3 Performance Parameters

Although the designed microwave cavity produced a dense plasma, the extracted ion beam current was not as dense. The extracted ion beam was limited by the space charge perveance limit, as well as the power supplies current limits. At a screen grid voltage of 1100 V and an acceleration grid voltage of -200 V, the maximum ion beam current obtained was approximately 57 mA.

Thrust Calculation

The total amount of thrust for an ion beam current of 57 mA, can be calculated with Equation 4.1.4 as

$$T = \gamma\sqrt{\frac{2M}{q}}I_b\sqrt{V_b} = 1.78\ mN,$$

with $V_b = 0.9(1100 + |200|) \approx 1170V$. The amount of thrust obtained from the ion thruster was greatly limited by the grid area. The ionisation experiments discussed in section 6.1.2, showed that the microwave discharge cavity is capable of generating a very high plasma density by absorbing almost 70% of the supplied microwave power. As a result, the grid area can be substantially increased to produce a greater amount of thrust.

Specific Impulse calculation

The specific impulse can be expressed with Equation 4.2.1

$$I_{sp} = \frac{T}{\dot{m}_p g}, \tag{6.2.1}$$

where $\dot{m}_p = QM$, with Q representing the argon mass flow rate (particles/s) and M representing the argon ion mass. The argon gas flow rate could only be roughly estimated by calibrating the needle valve with a helium leak detector at iThemba LABS, due to the unavailability of a mass flow meter. The argon flow rate was found to be approximately 1.6 *sccm* (standard cubic centimetres per minute) at the corresponding thrust measurement of 1.78 mN. The conversion of 1 sccm to particle/second [7] is

$$\begin{aligned} 1\ sccm &= \frac{6.02214179 \times 10^{23}\ [atoms/mole]}{22.413996\ [liters/mole\ at\ STP] \times 10^3\ [cc/liter] \times 60\ [s/min]} \\ &= 4.477962 \times 10^{17}\ [atoms/s]. \end{aligned} \tag{6.2.2}$$

Substituting $\dot{m}_p = QM$ into Equation 6.2.1 and applying the above conversion, the specific impulse for argon gas can be expressed as

$$I_{sp} = 3.403 \times 10^6 \frac{T[N]}{Q[sccm]}. \tag{6.2.3}$$

Thus the total specific impulse achieved with the designed ion thruster is approximately $I_{sp} = 3786\ seconds$.

In order to put the calculated values into perspective, new theoretical values needs to be calculated for the new corresponding grid voltages. The maximum theoretical current density calculated from Equation 2.3.2 yields

$$J_{max} = \frac{4\epsilon_0}{9}\sqrt{\frac{2e}{M}}\frac{V_T^{3/2}}{l_e^2} = 20.19\ mA/cm^2,$$

with $V_T = 1300\ V$ and $l_e = 0.1414\ cm$. The maximum theoretical ion beam current for an current density of 20.19 mA/cm^2, yields $I_b = 63.41\ mA$. The maximum thrust and specific impulse can be estimated using Equation 4.1.4 and Equation 4.2.5, respectively. The calculated theoretical parameters are $T_{theo} = 1.9\ mN$ and $I_{sp-theo} = 5850\ seconds$. A comparison of the theoretical performance to actual performance results are summarised in Table 6.3.

Table 6.3: Comparison of theoretical performance to actual performance results.

Results	Maximum ion beam current $[mA]$	Thrust $[mN]$	Specific Impulse $[seconds]$
Theoretical	63.41	1.9	5850 (3630)
Actual	57	1.78	3786

The theoretical results can be compared with the actual results and it is noteworthy to mention that the actual performance of the thruster is very close to the predicted performance. The reason for the high theoretical specific impulse is due to the assumption of an 80% propellant utilisation efficiency, η_m, of argon. In order to obtain a more accurate theoretical prediction of the specific impulse, the propellant utilisation is calculated.

Thruster Efficiency

The efficiencies for ion thrusters are generally described by their mass utilisation efficiency, η_m, electrical efficiency, η_e, and overall efficiency, η_T. The mass utilisation efficiency describes the ionisation efficiency of the thruster and can be calculated from Equation 4.2.4, as

$$\begin{aligned}\eta_m &= \frac{\dot{m}_i}{\dot{m}_p} = \frac{I_b}{q}\frac{M}{\dot{m}_p} \\ &= 0.4965 \ [49.65\%].\end{aligned}$$

Therefore, the new theoretical specific impulse can be calculated with 40% propellant utilisation efficiency as $I_{sp} = 3630$ *seconds*. The actual specific impulse of the thruster is thus very close to the predicted specific impulse.

The electrical efficiency, η_e, is defined as the ion beam power, P_b, divided by the total input power, P_T [7]:

$$\begin{aligned}\eta_e &= \frac{P_b}{P_T} = \frac{I_b V_b}{I_b V_b + P_o} \\ &= 14.29\%,\end{aligned} \tag{6.2.4}$$

where $P_o = 400\ W$ represents the power input needed for the ionisation of the extracted ion beam. However, the above electrical efficiency is not an accurate indication of thruster's efficiency. The input power of $P_0 = 400$, does not reflect the amount of power needed to produce an ion beam current of $I_b = 57\ mA$. A better indication of P_o could be determined by decreasing the input power of the magnetron until the ion beam current is affected. Unfortunately, this was not possible due to the fixed power output of the magnetron.

Miyoshi *et al.* [30] designed a 2.45 GHz microwave discharge ECR ion thruster, using argon as a propellant. Miyoshi found that approximately 37 W of microwave power was needed to sustain an ion beam current of $I_b = 64\ mA$. Taking Miyoshi's findings into consideration, a more accurate approximation of the electrical efficiency could be

calculated, by assuming an input power of $P_0 = 60\ W$ [2]. The new electrical efficiency was found to be $\eta_e = 52.64\%$ with an input power of $P_0 = 60\ W$.

Finally, the total efficiency, η_T, of the thruster was defined as the jet power divided by the total electrical power in the thruster [7]:

$$\eta_T = \frac{P_{jet}}{P_{in}} = \frac{T^2}{2\dot{m}_p P_{in}}. \tag{6.2.5}$$

The total input power for the thruster is calculated, from Equation 6.2.5, as

$$\begin{aligned} P_{in} &= \frac{I_b V_b}{\eta_e} \\ &= 126.69\ W. \end{aligned} \tag{6.2.6}$$

Substituting $P_{in} = 126.69\ W$ into Equation 6.2.5, the total amount of power the thruster converts into useful kinetic energy is approximately 30%.

General Remarks

The specific impulse can be increased by operating at high utilisation efficiency, η_m, and high ion acceleration voltages, V_b, as mentioned is Chapter 4. The specific impulse can also be increased by reducing the ion mass, M, although it will result in a lower thrust for the same power level. This can be explained by observing the thrust-to-total input power ratio

$$\frac{T}{P_T} = \frac{T\eta_e}{I_b V_b}. \tag{6.2.7}$$

If T from Equation 4.1.4 is substituted into Equation 6.2.8, and Equation 4.2.5 is used for the specific impulse relation, then Equation 6.2.7 becomes

$$\frac{T}{P_T} = \frac{2\gamma^2 \eta_m \eta_e}{g I_{sp}} = \frac{2\eta_T}{g I_{sp}}. \tag{6.2.8}$$

As can be seen in Equation 6.2.8, an increase in specific impulse will reduce the available thrust for a given input power and total thrust efficiency. Thus, the I_{sp}-to-thrust trade-off can only be improved by increasing the total efficiency of the thruster.

[2] Miyoshi *et al.* used a large grid area for the thruster. To compensate for the small grid area of the ion thruster implemented in this thesis, the input power was increased.

6.3 Summary

This chapter verified the feasibility of the ion thruster designed and manufactured in Chapter 3. Various experiments were conducted to determine the optimal operating conditions for the ion thruster. Initial experiments concluded that the plunger was necessary to 'ignite' the plasma at an operating pressure between $9 \times 10^{-3} - 5 \times 10^{-3}\ Torr$. However, the ECR process was found to be affective for the 'ignition' of the plasma as well as producing a high plasma density. The ECR process produced a high plasma density with a plasma absorption rate of approximately 77% of the total input microwave power. The plunger was thus found to be obsolete for ignition purposes. The optimal operating voltages for the screen grid and acceleration grid was found to be 1100 V and $-200\ V$, respectively. The feasibility of the ion thruster was verified with the successful ionisation and acceleration of ions to produce a thrust, $T = 1.78\ mN$, and a specific impulse of $I_{sp} = 3786\ seconds$, with a overall efficiency of 30%, at an argon gas flow rate of 1.6 $sccm$. The practical results were found to match the theoretical results extremely well and any deviations that occurred in the results were explained. The final results obtained resemble results found in literature [29; 30; 42]. Lastly, it was found that the I_{sp}-to-thrust trade off can only be improved by increasing the total efficiency of the thruster.

Chapter 7

Summary of Limitations, Recommendations and Conclusions

This chapter concludes the present study by providing an overview of the research conducted on electric thrusters. An ion thruster was designed and implemented in order to improve the lifespan and performance of electric thrusters. This objective was achieved by studying the method of electromagnetic ionisation, which eliminates the limited lifespan of electrode based ion thrusters. A summary of the research will be described below as well as the accomplishments that were achieved. In addition, several limitations and recommendations will also be discussed for future work that will aid thruster development for space exploration.

7.1 Ion Thruster Design

The design and implementation of a microwave discharge ion thruster was reported in this thesis. A discussion was provided on the fundamental theory of electric thrusters in order to determine the feasibility of electromagnetic thrusters. The different methods of ionising the propellant was presented, whereafter the method of RF ionisation was implemented. The electromagnetic fields used for the ionisation of the propellant eliminated the lifespan issues associated with electrode-based electric thrusters.

A study was conducted with three conceptual designs which entailed the use of a 2.45 GHz magnetron obtained from a domestic microwave oven. By examining the theory, it was found that a circular TM_{010} cavity coupled with a rectangular TE_{10} waveguide was the most ideal method for ionising the propellant. The electromagnetic fields inside the cavity was analysed using CST Microwave Studio software. The cavity was found to produce a maximum electrical field distribution in the centre of the cavity which assists in the ionisation of the propellant. In addition, the cavity was designed for the purpose of resonating at 2.45 GHz in a TM_{010} mode, prior to ionisation of propellant.

The two different methods of extracting and accelerating the ions, namely electromagnetic acceleration and electrostatic acceleration were discussed. Electromagnetic acceleration was found to be the most ideal method of accelerating the ions. The method will ensure a greater lifespan with an absence of erosion on grids and a greater thrust output in comparison with electrostatic acceleration. However, the implementation was found to be far too complex for the amount of time available. As a result, the method of electrostatic acceleration was implemented with stainless steel grids. This was achieved by designing a multi-aperture three-grid system where: a screen grid was biased at 1200 V; an acceleration grid was biased at -250 V; and a deceleration grid was biased at ground potential. The apertures were designed to allow the establishment of a Child-Langmuir sheath around each screen hole for effective extraction and acceleration of positively charged ions. The third grid was introduced in order to prevent ions from flowing back into the acceleration grid, thereby reducing the thrust and lifespan of the thruster.

7.2 Experimental Approach

In order to test the microwave based ion thruster, a two stage vacuum chamber was implemented, which could achieve pressures of at least 10^{-5} $Torr$. This was achieved by designing a vacuum system with a *Two Stage Edward* 8 rotary pump to achieve a pressure of approximately 10^{-3} $Torr$. Thereafter, an oil vapour diffusion pump was introduced to reduce the pressure to approximately 10^{-6} $Torr$.

Literature studies indicated that the entire TM_{010} resonant cavity needed to be raised to a bias positive voltage potential in order for the sufficient extraction and acceleration of the positively charged ions. In order to protect the magnetron from the high bias voltages, a 1 mm thick *Rogers* 4350 microwave substrate was designed with CST Microwave studio software. The substrate proved to be successful in dividing the cavity and the magnetron with a minimum RF leakage measurement of $1-8$ mW/cm^2, 50 cm away and further. The microwave substrate did, however, heat up fairly quickly. This limitation was overcome by introducing a small hole into the waveguide, at the input power side, to cool the substrate down with compressed air.

The process of electron cyclotron resonance (ECR) was introduced to the system by including a 875 Gauss electromagnet to assist with the ionisation process. The external magnetic field ensured that the gyration frequency of the electrons (from the argon gas) is in sync with the supplied 2.45 GHz microwave frequency. This resulted in the propagation of microwave energy into the plasma leading to producing a dense plasma.

7.3 Accomplishments

Testing verified the necessity of the ECR process for the ionisation of the neutral argon gas. In the absence of the external magnetic field, the plunger was found to be necessary for ionisation. In addition, almost all the microwave energy was reflected with only approximately 33% being absorbed by the plasma in the absence of ECR. The ECR process produced a high plasma density by absorbing 77% of the microwave energy. A decrease in the external magnetic field strength was found to have a proportionate decrease in plasma density and microwave energy absorption, which was confirmed experimentally. The feasibility of the ion thruster was verified with the successful ionisation and acceleration of ions to produce a thrust, $T = 1.78\ mN$, and a specific impulse of $I_{sp} = 3786\ seconds$ with a overall efficiency of 30%. The results were found to be comparable with other microwave discharge ion thrusters designed. The extraction and acceleration of a constant ion beam was found to be difficult. This was due to the current limitation of the power supplies being used. In addition, it was found that to increase the performance of the thruster, the total efficiency of the thruster needs to be increased.

7.4 Limitations and Recommendations

The main limitation of electric propulsion, which includes electromagnetic thrusters, is the need of high power units to produce thrust. The following recommendations discussed below, focus on improving the efficiency of the microwave discharge ion thruster.

Firstly, the resonant cavity in this thesis was designed for an empty cavity with focus placed on the 'ignition' of the neutral argon gas. As a result, with the plasma 'ignited', the cavity's resonant frequency changed. This resulted in a reflection of microwave power which decreased the efficiency of the thruster. An automated stub tuner can be implemented with a feedback system, using the data from the bi-directional coupler, in order to minimise the reflected power. The cavity's resonant frequency can, thus, be adapted accordingly to the plasma load to ensure maximum power efficiency.

Secondly, during testing of the thruster it was noted that there is an optimal operating condition for the thruster, which varies as the plasma density varies. Furthermore, it was found that the plasma density of the thruster is a function of the argon gas flow rate and absorption rate of microwave power. By implementing a variable form of microwave power and a precise controlled mass flow meter, the optimal operating conditions for the thruster can be controlled. This will ensure that the thruster achieves optimal operation conditions throughout the different plasma densities required for a desired thrust output.

Lastly, two recommendations are worth mentioning regarding the acceleration of the ions. The thrust output achieved by the designed thruster was severely limited by the grid area

of the ion optics. Thus, the first recommendation would be to increase the grid area of the ion optics. This would allow the utilisation of the high plasma density produced by the designed microwave cavity, thereby generating a greater amount of thrust. The second recommendation is the future study and implementation of grid-less acceleration method. Thereby the life expectancy of the thruster would be increased, and most importantly, the space charge limit present in grid based thrusters will be overcome.

7.5 Conclusion

The RF ion thruster designed in this thesis increased the expected lifespan of electric thrusters by successfully ionising a neutral argon gas with a 2.45 GHz magnetron coupled to a TM_{010} resonant cavity. The RF ion thruster utilise the process of ECR to increase the power efficiency of electric thrusters and showed good results. The research presented highlights the limitations that are inherent in ion thrusters that can be overcome with the use of feedback control systems. In addition, future research should be conducted into the use of grid-less thrusters to achieve optimal operating conditions, with maximum performance. This would allow space exploration to be facilitated as more efficient electric thrusters could be implemented. As a result, the two crucial performance parameters namely, thrust and specific impulse, can be increased.

Bibliography

[1] Turner, M.J.: *Rocket and Spacecraft Pro-Physics: Principles, Practice and New Developments.* Springer, 2008.

[2] Li, J.F.: *Design of a Microwave-Initiated Pulsed Plasma Thruster.* Master's thesis, Department of Mechanical and Aerospace Engineering, Princeton University, 2006.

[3] Chiravalle, V.: *A Numerical and Experimental Study of a Two-Stage Microwave Electrothermal Thruster for Spacecraft Propulsion.* Ph.D. thesis, Princeton University, 2003.

[4] Rayman, M.D. and Varghese, P.: The deep space 1 extended mission. *Journal of Acta Astronautica*, vol. 48, pp. 693–705, 2001.

[5] Choueiri, E.: A critical history of electric propulsion: The first 50 years. *Journal of Propulsion and Power*, vol. 20, pp. 193–203, 2004.

[6] Räisänen, O.: Electrostatic ion thuster. July 2012.

[7] Goebel, D.M. and Katz, I.: *Fundamentals of Electric Propulsion.* John Wiley & Sons, 2008.

[8] Chen, F.F.: Introduction to plasma physics and controlled fusion. *New York: Plenum Press*, vol. 1, 1984.

[9] Gedalin, M.: *Introduction to Plasma Physics.* 2002.

[10] Chabert, P. and Braithwaite, N.: *Physics of Radio-Frequency Plasmas.* Cambridge University, 2011.

[11] Astra: The variable specific impluse magnetoplasma rocket (vasmir).
Available at: `http://www.adastrarocket.com/aarc/VASIMR`

[12] Kuninaka, H. and Satori, S.: Development and demostration of a cathode-less electron cyclotron resonance ion thruster. *Journal of Propulsion and Power*, vol. 14, pp. 1022–1026, 1998.

[13] Lubey, D.P.: *Development of a Miniature Microwave-Frequency Ion Thruster*. Master's thesis, The Pennsylvania State Univerisity, 2011.

[14] Mehdizadeh, M.: *Microwave/RF Applicators and Probes : For Material Heating, Sensing and Plasma Generation*. Elsevier, 2010.

[15] Roth, J.: *Industrial Plasma Engineering*. Institute of Physics Publishing, 1995.

[16] Balanis, C.A.: *Advanced Engineering Electromagnetics*. John Wiley & Sons.

[17] Xiag Li, Y.J.: *Design of Cylindrical Cavity Resonator for Measurements of Electrical Properties of Dielectric Materials*. Master's thesis, University of Gavle, 2010.

[18] Ramo, S.: *Fields and Waves in Communication Electronics*. Wiley, 1994.

[19] Kajfez, D.: *Q Factor Measurements, Analog and Digital*.

[20] Jahn, R.G.: *Physics of Electric Propulsion*. Dover.

[21] et al., J.B.: Status of xenon ion propulsion technology. *Journal of Propulsion and Power*, vol. 6, pp. 145–150.

[22] Schimdt, G.R.: The nasa evolutionary xenon thruster (next): The net step for u.s. deep space propulsion. Tech. Rep., NASA Glenn Research Center.

[23] M. Patterson, J.F.e.a.: Next: Nasa's evolutionary xenon thruster.

[24] Child, C.: Discharge from hot cathode. *Physical Review*, vol. volume 32, p. 492, 1911.

[25] Langmuir, I.: The affect of space charge and residual gases on thermionic currents in high vacumm. *Physical Review*, vol. volume 2, p. 450, 1913.

[26] Rostoker, N.: Toroidal collective accelerator for heavy ions. In: *Electron Beam Research Technology, 1977 2nd International Topical Conference on*, vol. 2, pp. 635–645. 1977.

[27] Gower, S.: Development of a high power microwave plasma beam applicator. *American Institute of Physics*, vol. 72, p. 4273, 2001.

[28] Ganguli, A., Tarey, R., Arora, N., Narayanan, R. and Akhtar, K.: Development of compact electron cyclotron resonance plasma source. In: *Pulsed Power Conference (PPC), 2013 19th IEEE*, pp. 1–5. 2013. ISSN 2158-4915.

[29] Coletti, M. and Gabriel, S.B.: The applicability of dual stage ion optics to ion engines for high power missions. *IEEE Transactions on Plasma Science*, vol. 40, p. 1053, 2012.

[30] et al., M.M.: Microwave discharge ion thruster using argon as a propellant. In: *30th International Electric Propulsion Confernece*. 2007.

[31] Holmes, A. and Thompson, E.: Beam steering in electrode extraction systems. *Rev. Sci, Instrum.*, vol. 52, pp. 172–179, 1981.

[32] Lieberman, M. and Lichtenberg, A.: *Principles of Plasma Discharge and Materials Processing*. John Wiley and Sons, 2005.

[33] van Staden, W.F.: *The Fabrication of PBCO Buffered Step-edge Josephson Junction*. Master's thesis, Department of Electrical Engineering, Stellenbosch University, 2006.

[34] et al., D.P.L.: Design of the miniature microwave-frequency ion thruster. In: *32nd International Electric Propulsion Conference*. The Pennsylvania State Univerisity, 2011.

[35] Takao, Y., Iwata, I. and Chou, N.: Development of small scale microwave discharge ion thruster with variable magnetic field. In: *Renewable Energy Research and Applications (ICRERA), 2012 International Conference on*, pp. 1–2. 2012.

[36] Cubbin, E.: Pulse thrust measuerment using laser interferometry. *Review of Scientific Instruments*, vol. 68, pp. 2339–2346, 1997.

[37] Lun, J.: *Development of a Vacuum Arc Thruster for Nanosatelite Propulsion*. Master's thesis, Stellenbosch University, 2008.

[38] Byron, E. and Anders, A.: Ion energy distribution functions of vacuum arc plasmas. *Journal of Applied Physics*, vol. 39, pp. 1899–1906, 2003.

[39] A. Ganguli, M.K.A. and Tarey, R.: Absorption of high-frequency guided waves in a plasma loaded waveguide. *Journal of Physics*, vol. 14, pp. 102107–1–102107–10, 2007.

[40] et al., Y.C.: Measuerment of secondary electron emission. *IEEE Transactions on Plasma Science*, vol. 31, pp. 1095–1099, 2003.

[41] F Werner, D.K. and Engemann, J.: Slot antenna 2.45 ghz microwave plasma source. *Plasma Sources Sci. Technol.*, vol. 3, p. 473, 1994.

[42] Indranuj Dey, Y.T.e.a.: Microwave-plasma interaction in a miniature plasma ion thruster. In: *Presented at the 33rd International Electric Propulsion Conference*. 2013.

Appendices

Appendix A

Two Stage Vacuum System

The procedure of the two stage vacuum system designed for the testing of the ion thruster is presented in Sections A.1 to A.4.

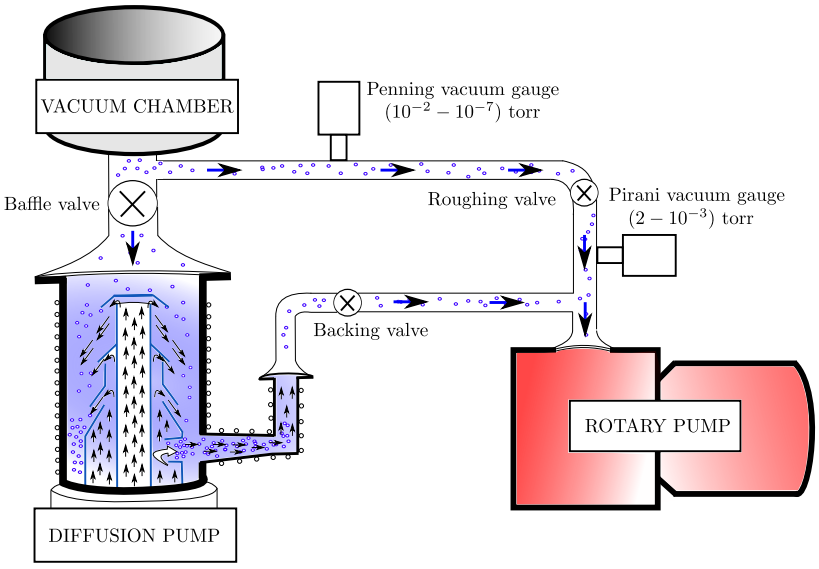

A.1 Pump Down Vacuum Chamber

- Close **baffle valve**
- Open **backing** and **roughing valves**
- Switch on **rotary pump**
- Turn on water supply for **vapour pump**
- Turn on element of **diffusion pump**
- Wait approximately 50 minutes (10^{-3} $Torr$) and then close **roughing valve**

- Open **baffle valve** (**backing valve** still open)

A.2 Open Vacuum Chamber

- Close **baffle valve**
- Vent **vacuum chamber** (**baffle** and **roughing valve** closed)

A.3 Pump Down Vacuum Chamber

- Close **backing valve** (**baffle valve** already closed)
- Open **roughing valve**
- Wait approximately 10 minutes and then close **roughing valve** and open **backing valve**
- Open **baffle valve**

A.4 Shut Down Vacuum System

- Close **baffle valve**
- Switch off element of **diffusion pump**
- Wait approximately 40 minutes for **oil vapour pump** to cool down and then close **backing valve**
- Switch off **rotary pump** and water

Appendix B

Design Drawings

This appendix contains the design drawings of the microwave thruster.

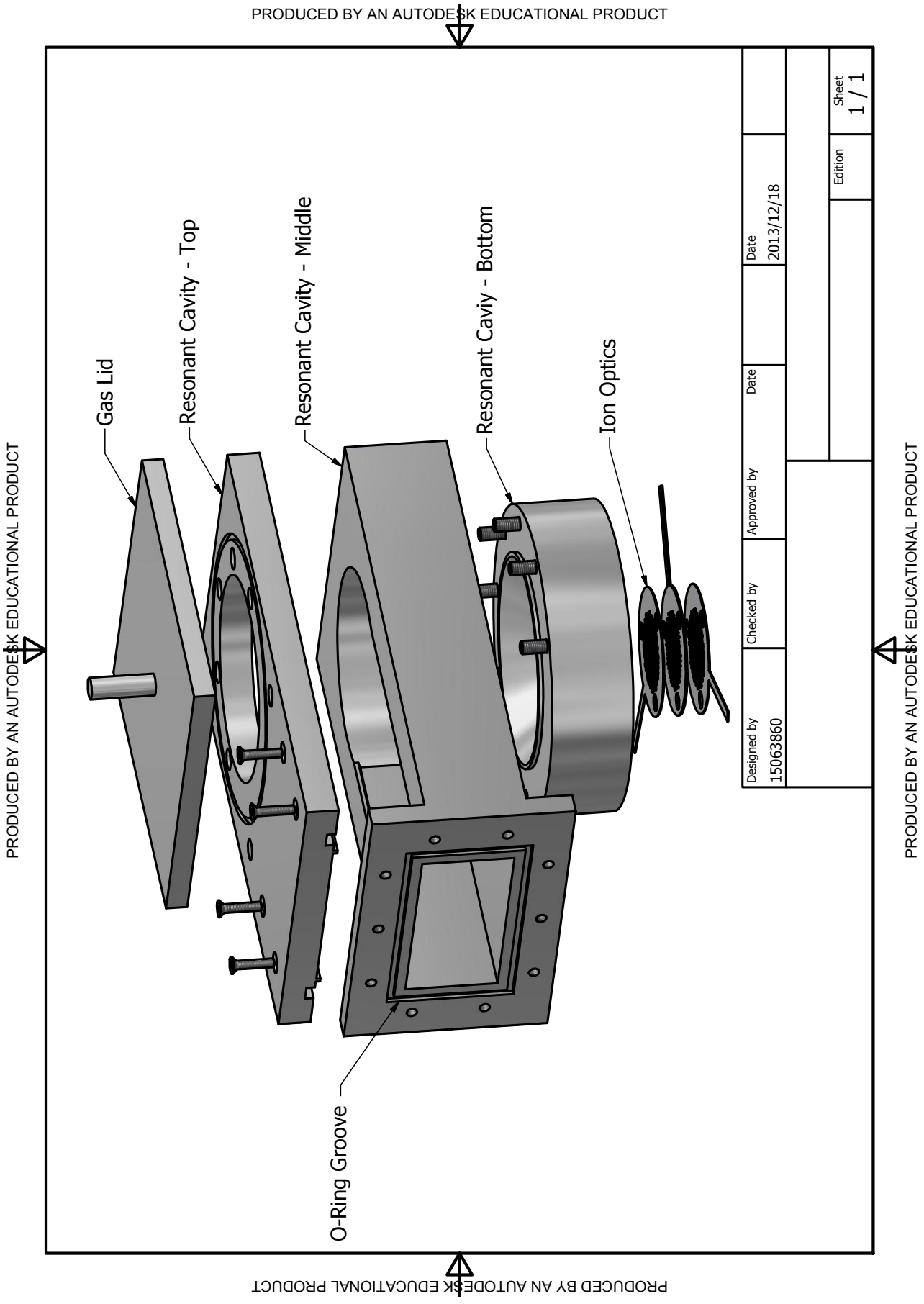

Figure B.1: Design drawing of complete thruster.

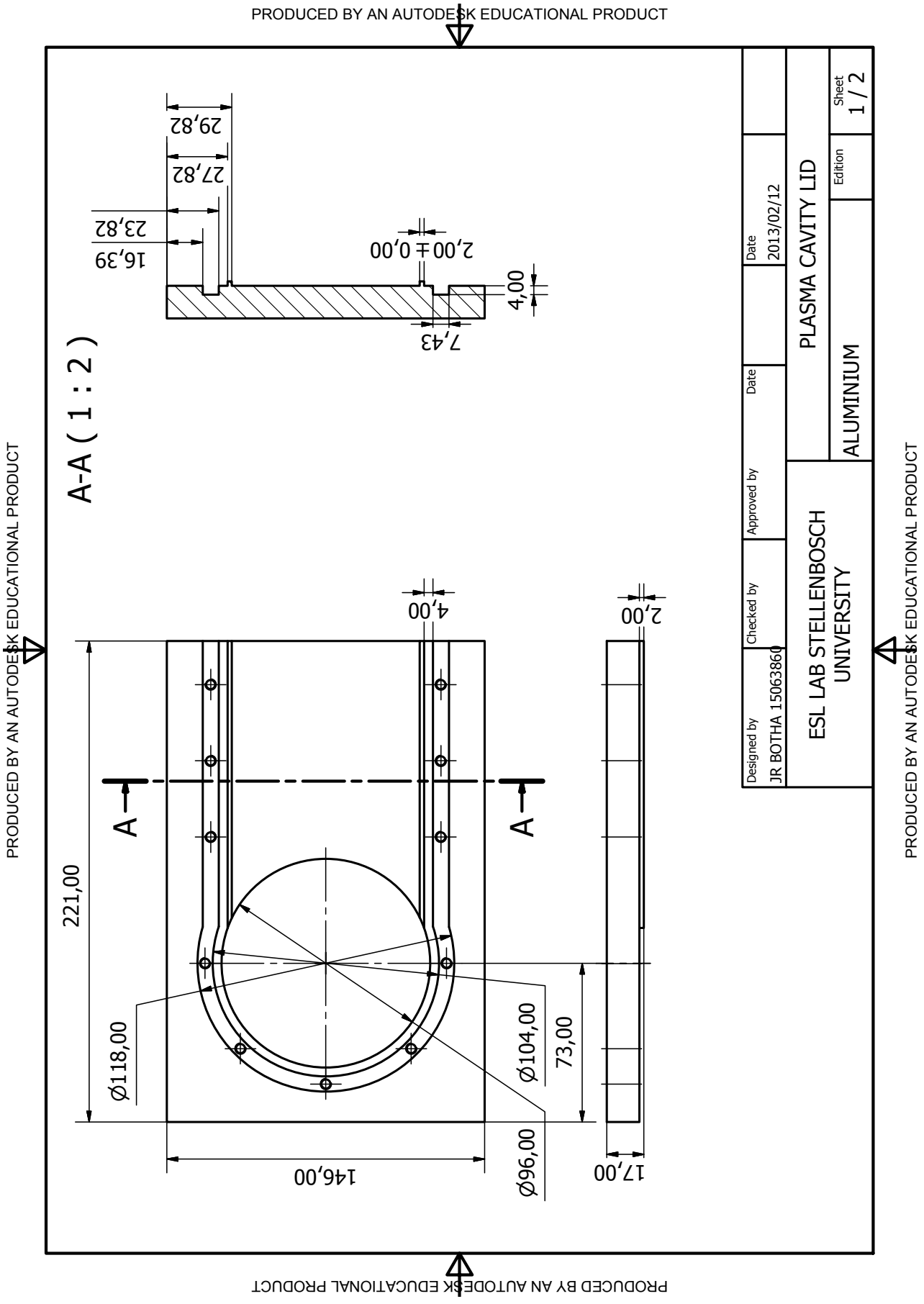

Figure B.2: Design drawing of resonant cavity - top section (1 of 2).

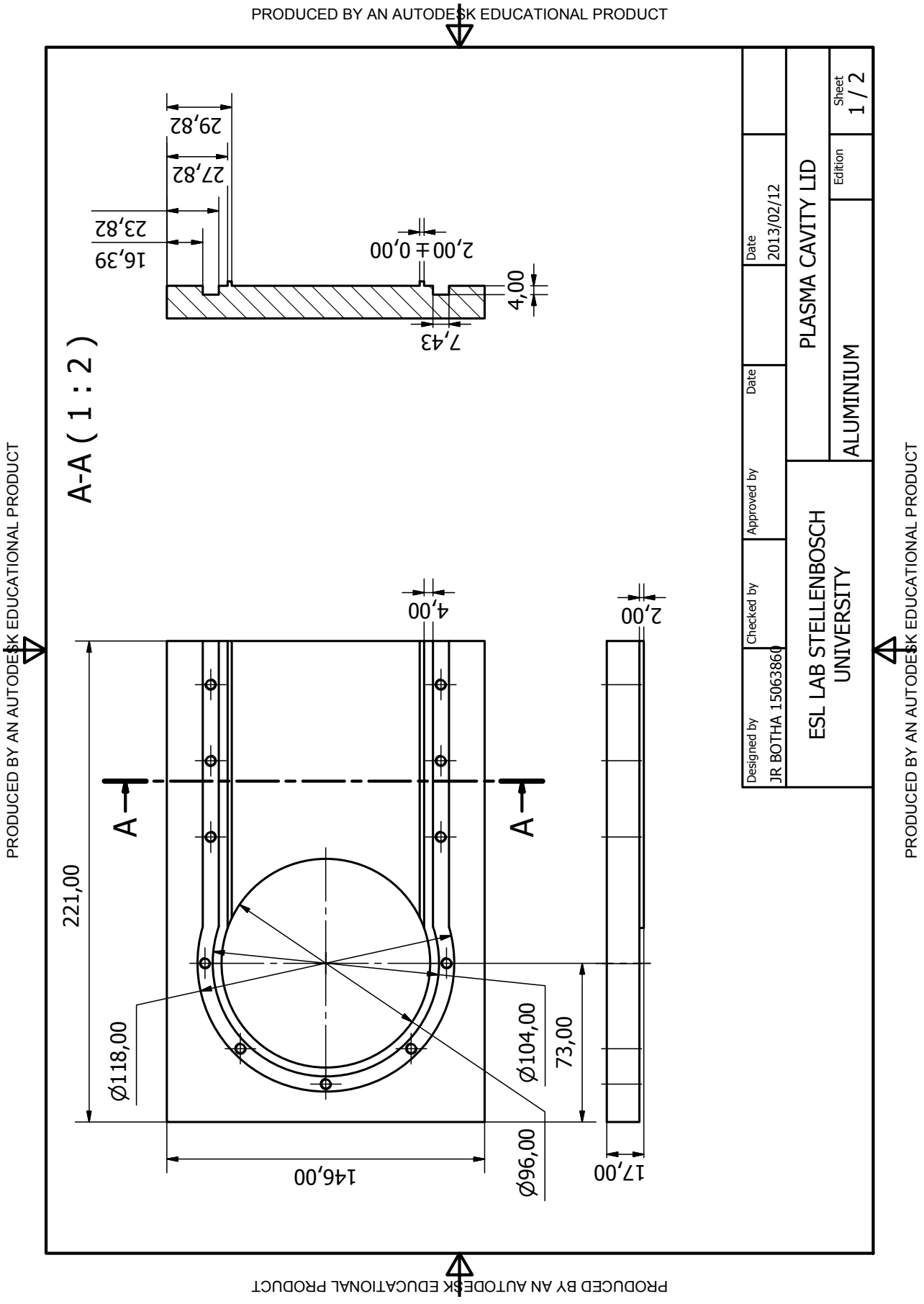

Figure B.3: Design drawing of resonant cavity - top section (2 of 2).

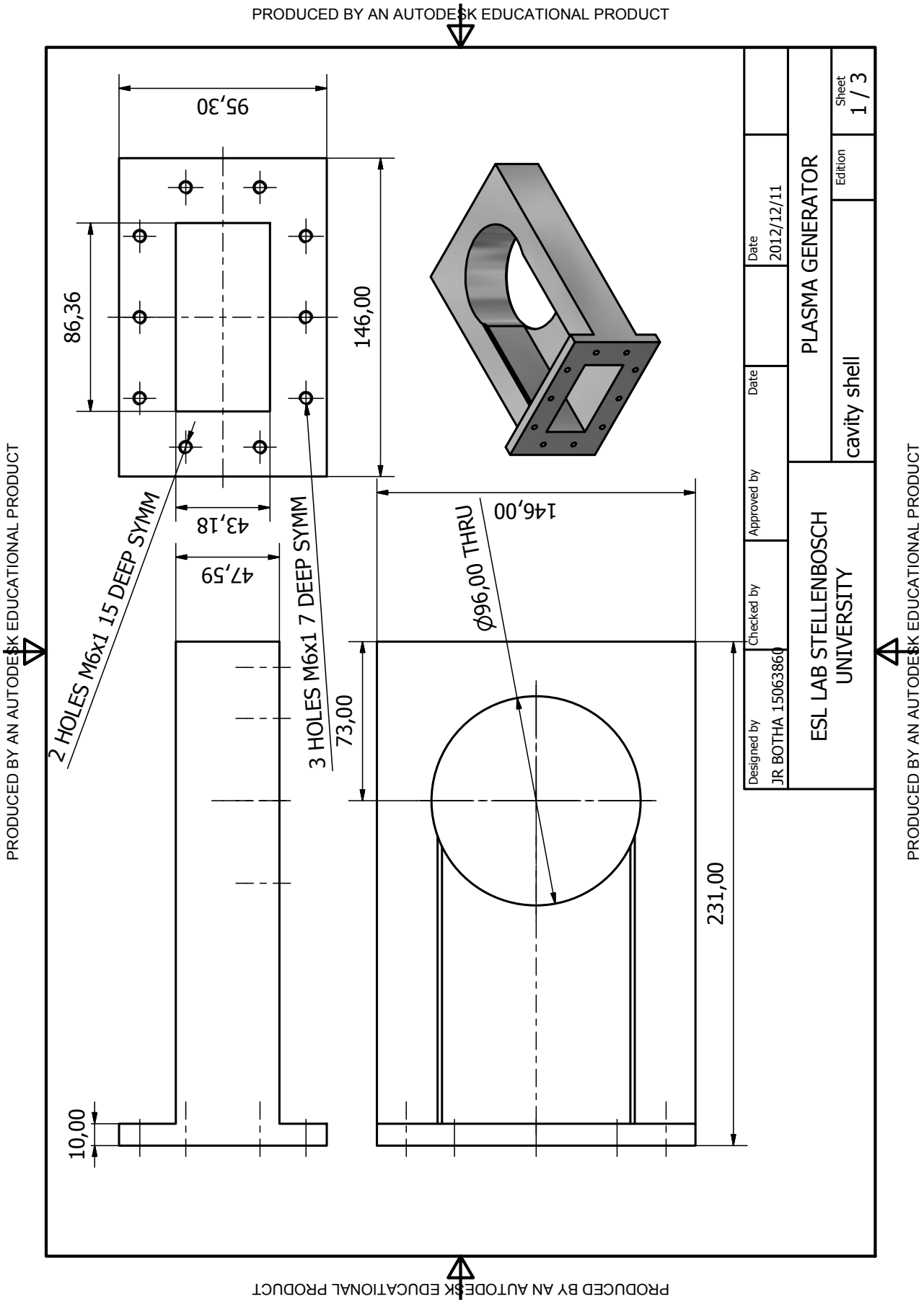

Figure B.4: Design drawing of resonant cavity - middle section (1 of 3).

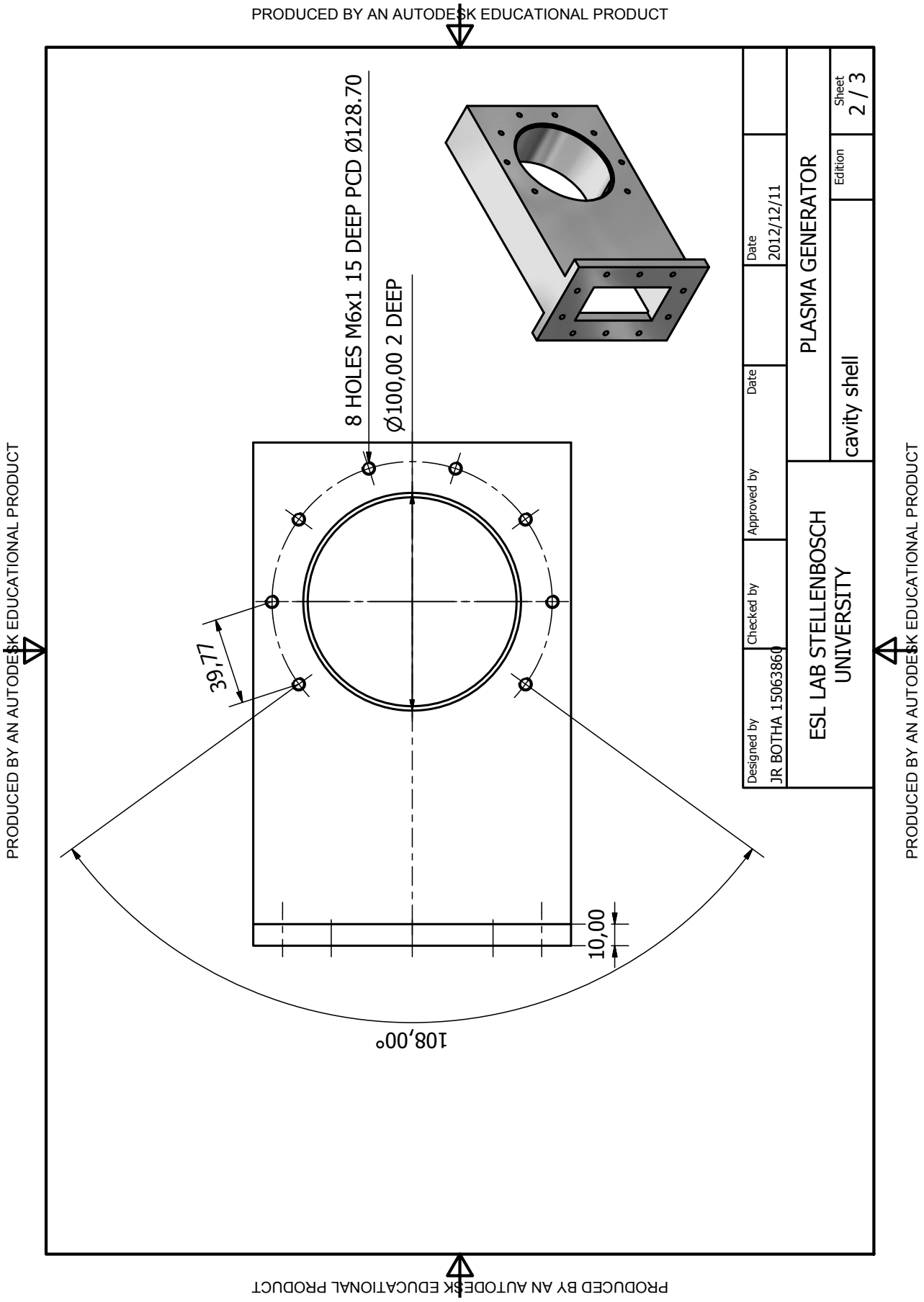

Figure B.5: Design drawing of resonant cavity - middle section (2 of 3).

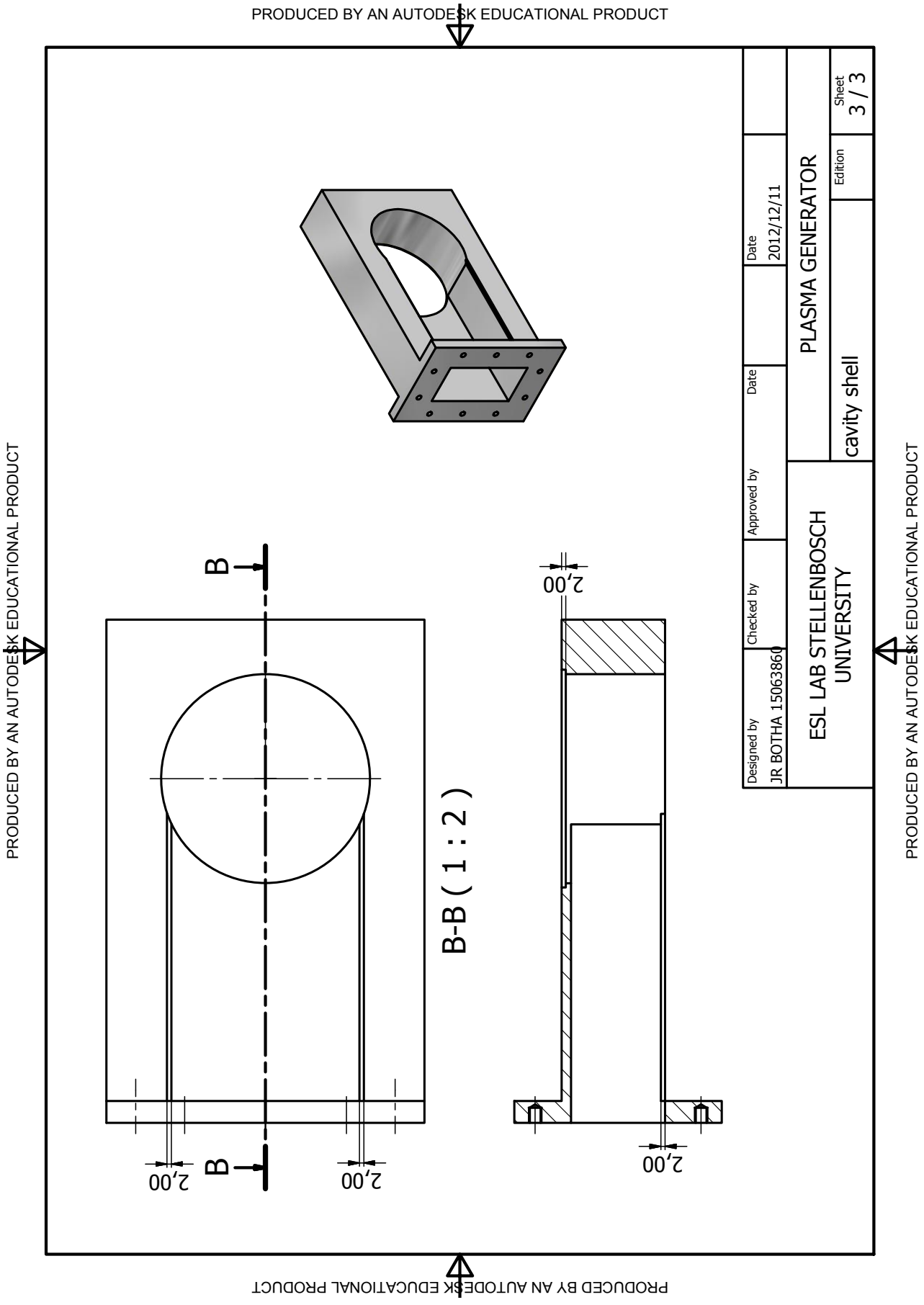

Figure B.6: Design drawing of resonant cavity - middle section (3 of 3).

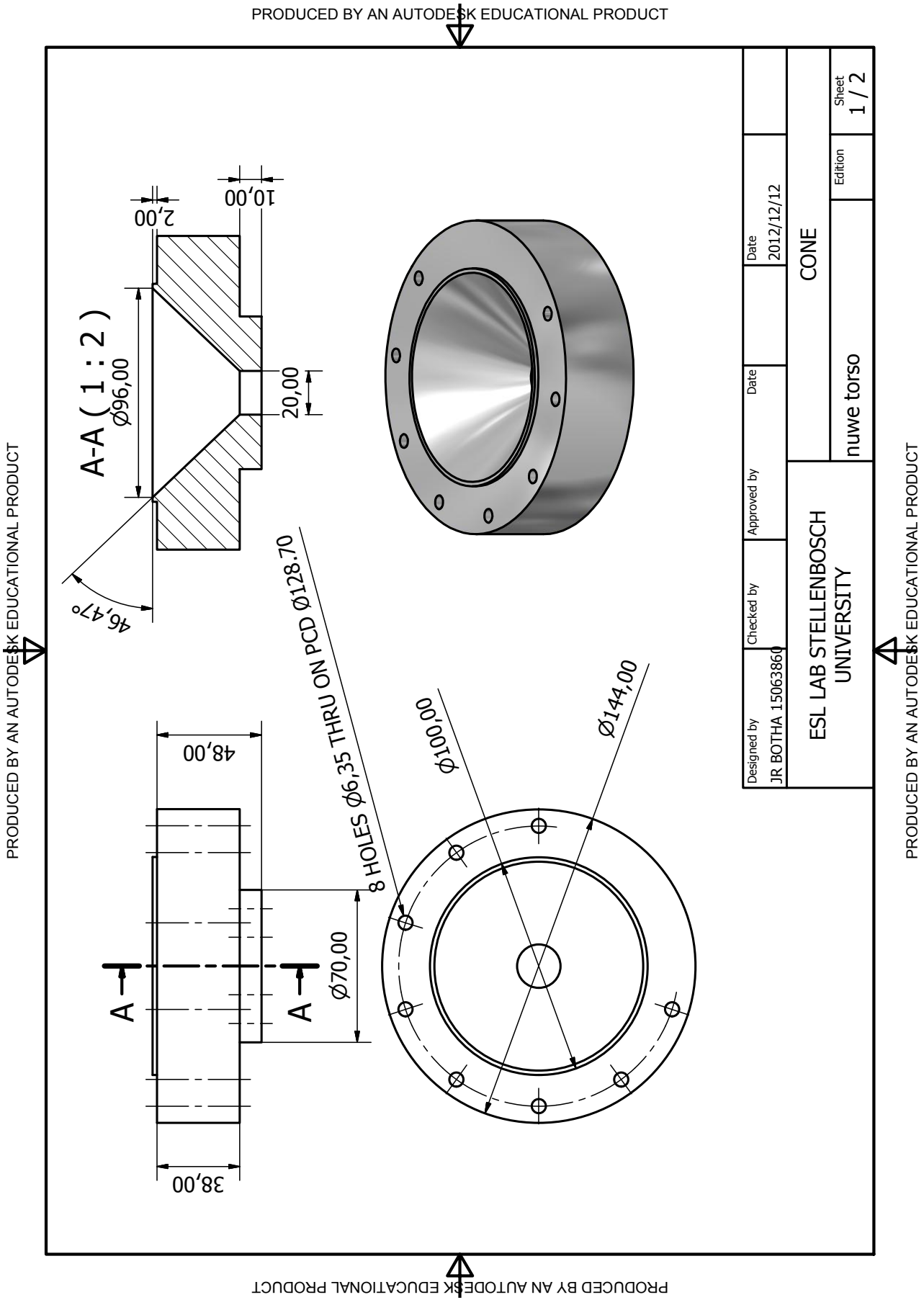

Figure B.7: Design drawing of resonant cavity - bottom section (1 of 2).

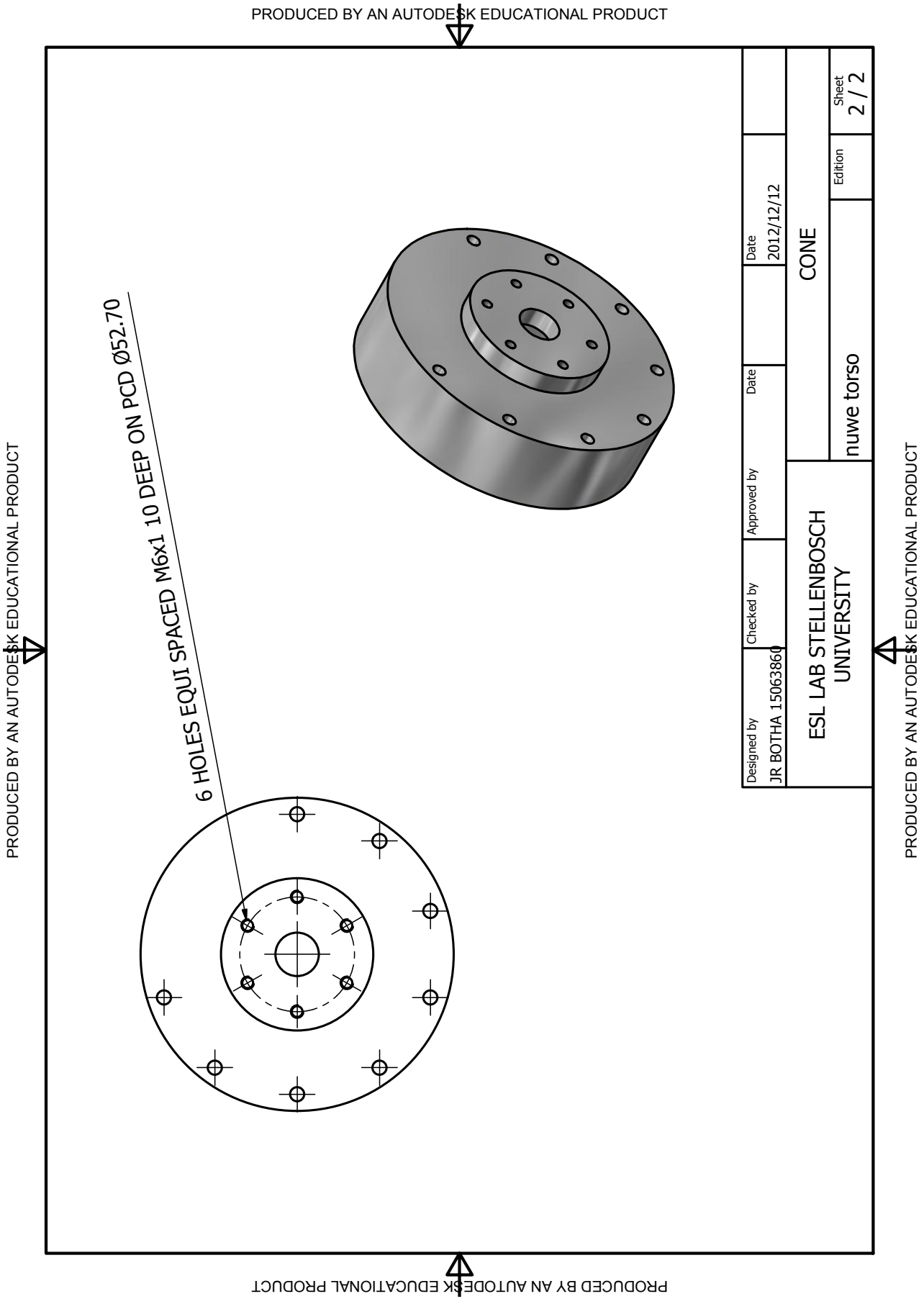

Figure B.8: Design drawing of resonant cavity - bottom section (2 of 2).

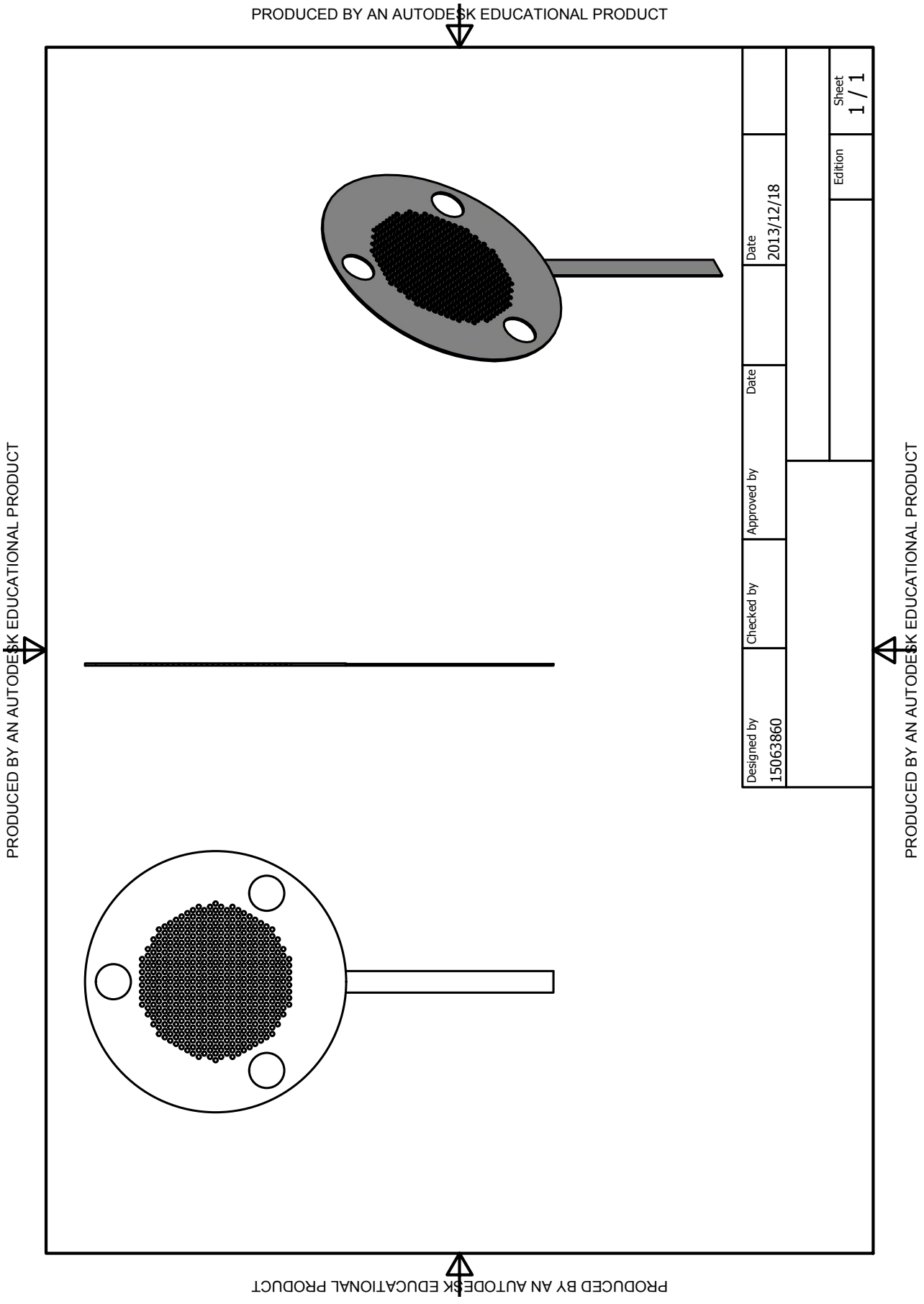

Figure B.9: Design drawing of a Grid.

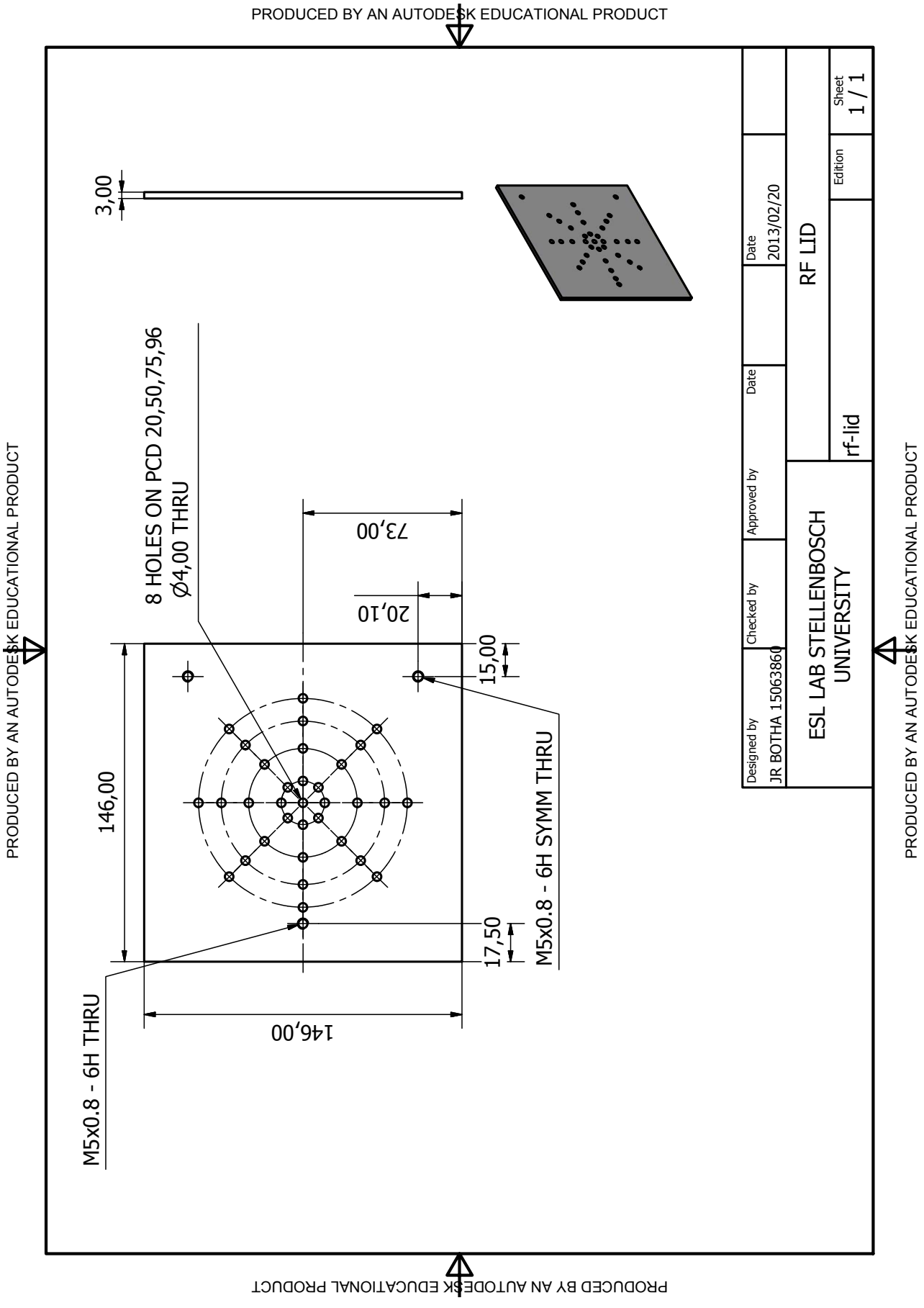

Figure B.10: Design drawing of lid to verify cavity operation.